INFORMATION TO USERS

This material was produced from a microfilm copy of the original document. While the most advanced technological means to photograph and reproduce this document have been used, the quality is heavily dependent upon the quality of the original submitted.

The following explanation of techniques is provided to help you understand markings or patterns which may appear on this reproduction.

1. The sign or "target" for pages apparently lacking from the document photographed is "Missing Page(s)". If it was possible to obtain the missing page(s) or section, they are spliced into the film along with adjacent pages. This may have necessitated cutting thru an image and duplicating adjacent pages to insure you complete continuity.

2. When an image on the film is obliterated with a large round black mark, it is an indication that the photographer suspected that the copy may have moved during exposure and thus cause a blurred image. You will find a good image of the page in the adjacent frame.

3. When a map, drawing or chart, etc., was part of the material being photographed the photographer followed a definite method in "sectioning" the material. It is customary to begin photoing at the upper left hand corner of a large sheet and to continue photoing from left to right in equal sections with a small overlap. If necessary, sectioning is continued again — beginning below the first row and continuing on until complete.

4. The majority of users indicate that the textual content is of greatest value, however, a somewhat higher quality reproduction could be made from "photographs" if essential to the understanding of the dissertation. Silver prints of "photographs" may be ordered at additional charge by writing the Order Department, giving the catalog number, title, author and specific pages you wish reproduced.

5. PLEASE NOTE: Some pages may have indistinct print. Filmed as received.

University Microfilms International
300 North Zeeb Road
Ann Arbor, Michigan 48106 USA
St. John's Road, Tyler's Green
High Wycombe, Bucks, England HP10 8HR

THE THEORY AND EXPERIMENT OF AN OPTICAL DEVICE EXHIBITING BISTABILITY AND DIFFERENTIAL GAIN

by

T. N. C. Venkatesan

A dissertation submitted to the Graduate Faculty in Physics in partial fulfillment of the requirements for the degree of Doctor of Philosophy, The City University of New York.

1977

This manuscript has been read and accepted for the Graduate Faculty in Physics in satisfaction of the dissertation requirement for the degree of Doctor of Philosophy.

1 MAY 77

Date

George Skorinko

George Skorinko
Chairman of examining Committee

Date

Myriam P. Sarachik

Executive Officer

Samuel L. McCall

S. L. McCall

Hyatt M. Gibbs

H. M. Gibbs

A. Halpern

N. Tzoar

Supervisory Committee

The City University of New York

1977

TO

MY PARENTS

THE THEORY AND EXPERIMENT OF AN OPTICAL DEVICE EXHIBITING BISTABILITY AND DIFFERENTIAL GAIN

By

T. N. C. Venkatesan

ABSTRACT

This thesis reports the theory and experiment of an optical element which exhibits bistable transmission, differential gain, discriminator, limiter and clipper actions. In all the above modes of operation of this element, a weak optical signal into a third port can control the output of a stronger optical power into the device. Hence this device may play as significant a role, in future optical signal processing as the transistor does in electrical communication today.

The element utilizes the nonlinear refractive index and/or the nonlinear absorption of a medium inside a Fabry-Perot interferometer. The idea for the nonlinear absorptive device was originally proposed by Seidel, rediscovered by Szöke and later by McCall. Several attempts were made to observe bistability and in the first successful experiment by H. M. Gibbs, S. L. McCall and T. N. C. Venkatesan using a sodium vapor filled Fabry-Perot and a tunable dye laser source, the dominance of nonlinear refractive index over nonlinear absorption was discovered.

Since then a simple model which explains the important features of the device has been developed. In pursuit of a solid state device, an experiment was performed with ruby, using a cw ruby laser source specifically for this thesis work. Unanticipated room temperature operation of the device revealed an overlooked contribution to the nonlinear refractive index.

Excellent agreement between the theory and the experiment has been seen. The results of the sodium and ruby experiments greatly increase the choice of materials for making such devices. The device does not need any population inversion of the intracavity medium and in principle it may be possible to make micron size, nanosecond speed, solid state devices utilizing submicrowatts of optical power.

ACKNOWLEDGMENTS

Research with Drs. Sam McCall and Hyatt Gibbs has been an educative and exciting experience. I am indebted to Sam for suggesting the thesis topic and guiding me to completion. To Hyatt, I owe my basic experimental training. I am also thankful to him for letting me use his laboratory for all my experimental work. Above all, I am grateful for their sincere concern for my welfare.

In the course of the experiment I received help from many people, and I would like to thank in particular, Dr. Mike Sturge, who triggered my thoughts toward the non-resonant bands in ruby, Al Passner for helping me with the several electronic servo systems that I had to build, Gary Patterson for letting me use his cryogenic dewar and Charlie Rubinstein for lending me the glass rods for the Faraday Rotator. I am grateful to Dept. 1115, headed by Dr. Phil Platzman for a Research Assistantship.

I thank Professors George Skorinko, Alvin Halpern and Narkis Tzoar for serving on my thesis committee. I especially want to thank Professor Skorinko, not only for acting as the chairman of my thesis committee, but also for his valuable criticism of my dissertation. I take this opportunity to express my gratitude to Professors Joseph Krieger and Victor Franco at Brooklyn College from whom I learned a great deal.

Finally, I am very grateful to Lakshmi, my wife, and my family for sharing all my ups and down in the course of my doctoral work and for inspiring me to a successful finish.

CONTENTS

CHAPTER 1

INTRODUCTION

There has been a rapid growth in the fields of optical integrated circuits, optical display and optical communication in the past decade. If one pauses to think about the advancement of a field like electronics, one realizes the vital role played by the triode and the transistor: three port devices with which one is able to control a large voltage or current by a weak signal. An analogous three port device in the optical regime where the transmission of a light beam through the device is controlled by a weaker light beam, should be an important asset to optical signal processing. This thesis is about such a three-port optical device. Possible noise reduction in very closely spaced information channels (optical fibers) and the possibility of sending different colored, noninteracting light beams down the same fiber (equivalent to several currents in the same wire) may turn out to have significant advantages which favor optical systems in the future.

This optical device has several interesting modes of operation, obtained by varying some of the parameters of the device. In Fig. 1 the different modes of operation are illustrated. The graph of the output light intensity versus the input light intensity is called the characteristic curve of the device, and the curve is qualitatively different for the different modes of operation. The first mode is the bistable mode; in this curve we see that the

output has two stable values for the same input intensity for a certain region of the input. A device operating in this mode is an optical logic device where, with a dc light intensity between "switch-on" and "switch-off" points, a weak light pulse can switch the device to the 1 or 0 state as shown in the figure. A bistable device could also be used as a short term memory. However, a constant power source is needed for such an application but, operating in a large duty cycle, this would not be a great drawback.

In the second mode of operation "the discriminator and pulse amplifier", one sees a potential candidate for an element in a repeater station in an optical communication network using pulse code modulation. In this method of communication, the information is coded in the form of light pulses and is transmitted in an optical fiber. The pulses not only attenuate with distance but also become noisy. A discriminating pulse amplifier at a repeater station may be used to reject the noise and regenerate the optical pulses.

In the third mode of operation "the transistor or the differential or ac gain mode", the curve exhibits a region of slope greater than one. A small signal modulating a dc level of light is amplified. This mode of operation might be useful for analog communication.

The next mode of operation is the clipper. As is shown in the figure, this could be used to eliminate noise or reshape optical pulses. In laser induced fusion and

in certain coherent optics experiments, pure pulses of light without any small pre- or post-pulses are required. The clipper mode can provide such pulses.

Finally one has the limiter mode of operation, in which one sees a region where the output is independent of input variations. Such a device may be used to stabilize a light source or produce pulses with a smooth top as shown. If optical signal processing develops in a manner analogous to electrical signal processing, all these different modes of the device have potential application.

A bistable device utilizing a nonlinear absorber inside an optical cavity was first proposed by Seidel,[1] and later independently by Szöke et al.[2] and then by McCall.[3] Several attempts, to observe bistability, have been made.[4] In the first successful demonstration of bistability, Gibbs, McCall and Venkatesan[5] used a sodium vapor filled Fabry-Perot interferometer (FP). A major outcome of this experiment was the recognition of the dramatic role played by nonlinear refractive index,[6] which not only decreased the threshold for bistability but also increased the frequency range of operation of the device. The importance of nonlinear refractive index has subsequently been recognized by Felber and Marburger.[7] In pursuit of a solid state device, similar effects were demonstrated in ruby by Venkatesan and McCall.[8] An interesting related work has been done by Smith et al.,[9] while other proposals have also been made.[10,11,12]

One can qualitatively picture the action of the refractive index device in the following way. Consider an empty FP with ten percent transmitting mirrors. When the cavity is mistuned with respect to an incoming light beam (the optical path length within the cavity is somewhat different from an integral number M of half wavelengths, i.e., the round trip phase $\overline{\Phi} = 2\pi M + \theta$) the intracavity intensity is about ten percent of the input intensity, as there is negligible constructive interference between the forward and backward waves inside the cavity. But, when the cavity is tuned to be on resonance (i.e. $\overline{\Phi} = 2\pi M$), the intracavity intensity is about ten times the input intensity. This large resonant intracavity energy has been utilized in many experiments, notably intracavity second harmonic generation. This dual value for the intracavity intensity (depending on whether the cavity is tuned on resonance or not with respect to the light) is the essential property of the FP which is responsible for the bistable operation of the device. What happens when a medium whose refractive index is dependent on the intracavity light intensity is put into the cavity? Let us look at Fig. 2 and try to construct a possible characteristic curve. Let the cavity be mistuned at low light intensity, so that the total round trip phase $\overline{\Phi} = 2\pi M - \theta + \Phi(P_c)$, $\theta \neq 0$, where $\Phi(P_c)$ the intensity dependent phase is chosen to be positive. As the input intensity is increased, the cavity intensity increases, and hence $\Phi(P_c)$

increases such that the round trip phase, $\bar{\Phi}$, approaches the resonance value $2\pi M$. At a critical value of the input intensity there is a run-away effect, as, the increasing $\bar{\Phi}$ increases P_c (the cavity power) and vice versa. The phase, $\bar{\varphi}$, then rapidly increases to a value slightly larger than $2\pi M$. As a result the output of the cavity switches from a low to a high value. Further increases in the input would give a somewhat uniform transmitted output as the fractional transmission of the cavity decreases with increasing intensity. However, upon decreasing the input intensity, the large intracavity intensity maintains the value of $\bar{\varphi}$ close to $2\pi M$ and consequently the device turns off at a lower value of the input than is required to switch it to the high output state. This hysteresis is the origin of the bistability.

A similar argument could be used to describe the action of a device using only a saturable absorber. The intracavity absorption reduces the Q of a cavity (which is tuned to transmit the light, i.e., $\theta = 0$), at low intensities. At higher intensities the absorption saturates and the device switches to a transmitting state. In the absorptive case, also, there will be a hysteresis in the characteristic curve, as this is an inherent property of a FP.

By varying the initial mistuning of the FP and the nonlinear medium inside the cavity, other modes of operation can be obtained. In the different modes of operation, a cw light beam can be controlled by a weak beam (not

necessarily at the same frequency) from a third port. In other cases the weak control signal could be non-optical.

The following chapters in this thesis, present the relevant theory and describe the experimental details and results. The second chapter presents a simple mathematical model which adequately describes the operation of the device. In particular, the model neglects the effect of the spatial modulation of the intracavity non-linearity, due to standing waves. The dynamics of the system are studied using this model. To understand the physics of the nonlinear absorption and refractive index, a two level atomic system is considered in the third chapter. Further, the problem of a bistable element consisting of a FP containing a homogeneous two level medium, is solved, including standing wave effects. The reader may skip the third chapter, as it illuminates only some finer points. The fourth chapter describes the sodium vapor experiment in which the author was a collaborator. Only a brief review is presented here. The last chapter, the thesis research work of the author, deals with the ruby experiment. That chapter describes the initial expectations of the author, the actual setting up of the experiment, the pleasant surprise that occurred (room-temperature operation), the explanation of the final results, and a theoretical simulation of the experiment. The thesis ends with a conclusion, in which the limits of the device have been specified and some forecasts have been made.

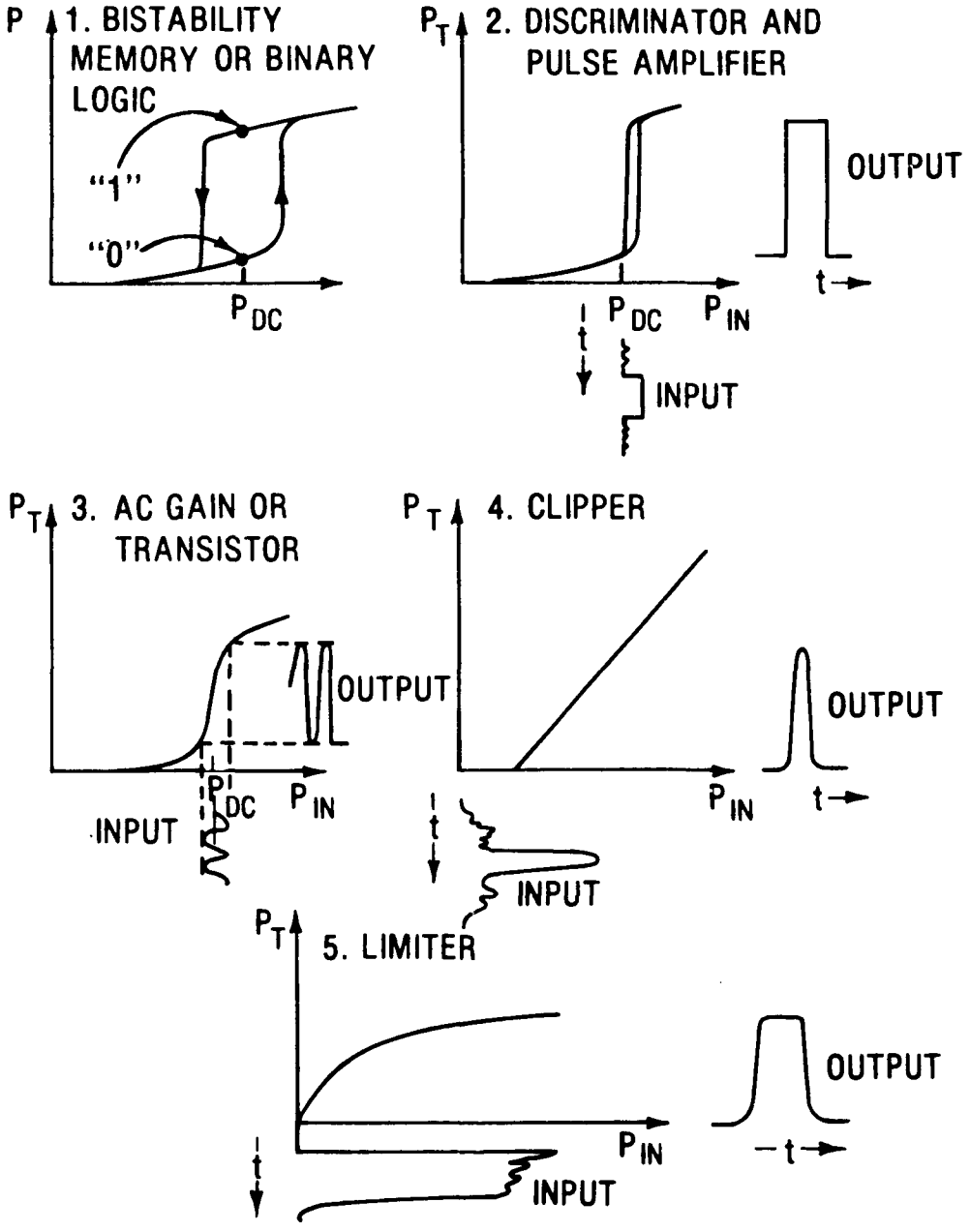

The different modes of operation of the device

Figure 1

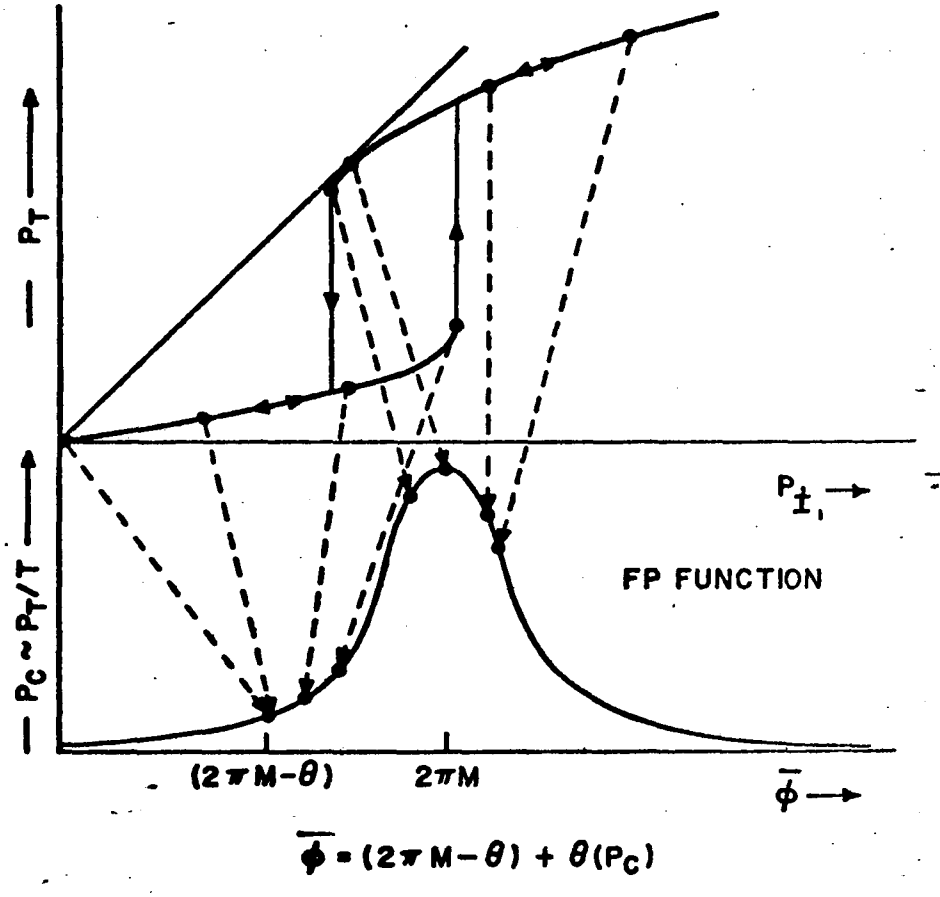

HYSTERESIS IN A NONLINEAR REFRACTIVE INDEX DEVICE

Figure.2

CHAPTER 2

2.1 A SIMPLE MATHEMATICAL MODEL

An exact mathematical description of the device is difficult, but most of its qualitative features can be understood by use of a very simple mathematical model. This model clearly shows the role of the detuning parameter, the nonlinear refractive index and the mirror reflectivity.

The transmission of a FP is described in terms of the input field E_I and transmitted field E_T, through the standard formula,

$$E_T = Te^{i\bar{\Phi}/2}(1-Re^{i\bar{\Phi}})^{-1}E_I \ , \qquad 2.1$$

where $\bar{\Phi}$ is the round trip phase shift, and T and R are the transmissivity and reflectivity of the FP mirrors, respectively. $\bar{\varphi} = 2\pi n\,(2L/\lambda)$, where $L \gg \lambda$ is the mirror separation, n the refractive index, and λ the light's vacuum wavelength. If $\bar{\Phi}$ is a multiple of 2π, the FP transmission is 100%. In the case when the FP has a nonlinear medium between the plates, $\bar{\varphi}$ is a function of the fields inside the FP. These fields are directly related to E_T, through boundary conditions at the exit mirror, and $\bar{\varphi}$ is regarded as a function of E_T.

In the limit of small T, the FP transmission is insignificant, unless $\bar{\varphi}$ is nearly a multiple of 2π. Let $\bar{\varphi}$ differ from a multiple of 2π by $\Delta\varphi(E_T)$, which is small in absolute value. Then using Eq. 2.1, approximately with $R/T \gg 1$ and $\Delta\varphi$ small we get

$$E_I = E_T - i(\frac{R}{T})\Delta\varphi(E_T)E_T \ . \qquad 2.2$$

The intensity dependent nonlinearity is contained in $\Delta\varphi(E_T)$ which is in general complex. The real part $\Delta\varphi^R = \varphi(E_T) - \theta$, is due to the nonlinear index and the imaginary part $\Delta\varphi^I$ is due to the absorption. Squaring 2.2, yields (with appropriate constants)

$$P_I = P_T[(1+\Gamma\Delta\varphi^I)^2 + \Gamma^2(\varphi(P_T) - \theta)^2], \qquad 2.3$$

with $\Gamma = R/T$. As seen in the introduction, a mistuning θ is needed for the nonlinear index device to work. Since relevant quantities are the power input and output henceforth, we will deal with power rather than intensity. Further the phase is now considered a function of P_T rather than E_T.

In Eq. 2.3 the striking feature is that the incident power is calculated in terms of the transmitted power. This is mathematically easier to deal with since P_I is a single valued function of P_T whereas the reverse is not necessarily true.

In Fig. 3, Eq. 2.3 is displayed for the case of zero absorption, i.e. ($\Delta\varphi^I = 0$). One sees that P_I is made of two parts, a unit slope line due to P_T and the rest of the curve due to $\Gamma^2(\varphi-\theta)^2P_T$. It is easy to see that as long as $\varphi(P_T)$ is not a constant one could always construct a curve by varying Γ^2 and θ such that P_T becomes a multivalued function of P_I. This is true

because $(\varphi-\theta)^2 P_T$ has at least two zeros, one at $P_T = 0$ and another where $\varphi(P_T) = \theta$. In between the two values of P_T the function is hump shaped. By making Γ^2 large enough the characteristic curve could be made to go bistable.

It can be shown that points where $\frac{\partial P_I}{\partial P_T} < 0$ are unstable and hence the device would switch up or down where $\frac{\partial P_I}{\partial P_T}$ is close to zero. In the appendix A this is proved for a purely absorptive case using a two level Bloch model for the nonlinearity.

2.2 DYNAMICS

How does the output evolve in time when the input is changed? How do the rise and fall times of the bistable device depend upon the properties of the cavity and the intracavity media? This section will try to answer these questions. A few approximations will be made to simplify the problem. It will be assumed that the device has a medium with no absorption but a nonlinear refractive index and that the phase shift grows exponentially with time, when the intracavity field is changed. Consider the phase shift to be of the form

$$\varphi(t) = \int_{-\infty}^{t} e^{-(t-t')/t_0} \left[f(P_T(t')) \right] dt' , \quad 2.4$$

where f is an unspecified function of the intracavity power and is simply related to the transmitted power. We shall neglect

the cavity build up time. This is a good approximation for a small practical device.

From Eq. 2.4 we get, with time measured in units of t_0 a characteristic time determined by the medium

$$\dot{\varphi}(t) + \varphi(t) = f(P_T). \qquad 2.5$$

Since $\Delta\varphi^I=0$ in the absence of absorption, Eq. 2.3 can be set to

$$P_I = P_T\,[1 + \Gamma^2(\varphi-\theta)^2]. \qquad 2.6$$

Then $f(P_T) = f\left(\frac{P_I}{1+\Gamma^2(\varphi-\theta)^2}\right)$ now expressed as a function of φ, is symmetrical about $\varphi = \theta$ (Fig. 4). Define

$$F(t,\varphi) = f\left(\frac{P_I(t)}{1+\Gamma^2(\varphi-\theta)^2}\right) - \varphi\,, \qquad 2.7$$

so that

$$\dot{\varphi} = F(t,\varphi).$$

The steady-state value of the phase shift is the solution of $\dot{\varphi} = 0$, i.e.,

$$f\left(\frac{P_I(t)}{1+\Gamma^2(\varphi-\theta)^2}\right) - \varphi = 0. \qquad 2.8$$

This equation has several solutions, and we can study the stability of these solutions for a simple form. In Fig. 4 $f(P_T) = \dot{\varphi} + \varphi$ is plotted as a function of φ for a given P_I. The intersections of the $\dot{\varphi} = 0$ and $f(P_T)$ curves give the steady state value of φ. If P_I is such

that there are three different steady state values of φ, then P_T has more than one value for that P_I. Which of these are stable values? Let φ_0 be a steady state value. If φ changes from φ_0 by a small amount $\Delta\varphi$ what happens to the temporal evolution of $\Delta\varphi$? Expanding φ about φ_0 yields

$$\dot{\Delta\varphi} = F_{\varphi_0} \Delta\varphi \ , \qquad 2.9$$

where $F_{\varphi_0} = \left.\frac{\partial F}{\partial \varphi}\right|_{\varphi_0}$. The solution to this equation assuming small variation of F_{φ_0} is,

$$\Delta\varphi(t) = \Delta\varphi(0) e^{F_{\varphi_0} t} \ . \qquad 2.10$$

The solution is unstable for $F_{\varphi_0} \geq 0$, but converges for $F_{\varphi_0} < 0$ (Fig. 4). An approximate solution in the vicinity of a steady state value of the phase is,

$$\varphi(t) = \varphi_0 + \Delta\varphi(0) e^{F_{\varphi_0} t} \ , \qquad 2.11$$

where differentiating Eq. 2.7 one obtains,

$$F_{\varphi_0} = - \left\{ 1 + \frac{2P_I(\varphi_0-\theta)\Gamma^2}{[1+\Gamma^2(\varphi_0-\theta)^2]^2} \ f'\left(\frac{P_I}{1+\Gamma^2(\varphi_0-\theta)^2} \right) \right\} . \qquad 2.12$$

Eq. 2.11 defines a time constant $\tau = -1/F_{\varphi_0}$. Clearly for meaningful values of τ, F_{φ_0} must be less than

zero. For cases where $\dot{\varphi}_0 \neq 0$, we can define a time constant as,

$$\frac{1}{\tau} = - \frac{\dot{\varphi}}{\varphi - \varphi_0} . \qquad 2.13$$

Hence,

$$\tau = \frac{\varphi_0 - \varphi}{f\left(\frac{P_{I_0}}{1 + T^2(\varphi - \theta)^2} \right) - \varphi} , \qquad 2.14$$

in units of t_0. Since φ increases monotonically with time, the topology of $P_T(t)$ versus t is the same as $f(P_I, \varphi)$ as a function of φ (i.e., maxima, oscillations, etc.). Using this fact the output for a square input has been obtained in Fig. 5a. The phase φ goes from φ_A to a final value φ_B. If φ goes through the value θ, overshoots occur when the output intensity switches on or off. The sharp rise at φ_A (Fig. 5a) from curve A to B is limited by the cavity transit time which is assumed to be short.

We can approximately determine the time dependence of P_T by considering two regions: $\varphi > \theta$ and $\varphi < \theta$ (Fig. 5b). For $\varphi < \theta$ assume a linear increase of φ with time, so that from Eq. 2.5

$$\left.\begin{aligned} \dot{\varphi} &\simeq f(P_{I_B}) - \theta \\ \varphi &\simeq (f(P_{I_B}) - \theta)t + \varphi_A \end{aligned}\right\} \quad \varphi < \theta . \qquad 2.15$$

For $\varphi > \theta$ assume an exponential evolution of φ with time,

so that

$$\left.\begin{aligned} \dot{\varphi} &\simeq \gamma(\varphi_B-\theta)e^{-\gamma t'} \\ \varphi &\simeq \theta + (\varphi_B-\theta)(1-e^{-\gamma t'}) \end{aligned}\right\} \quad \varphi > \theta; \quad t > \frac{\theta-\varphi_A}{f(P_{I_B})} \quad , \tag{2.16}$$

where

$$\gamma = 1 - \left.\frac{\partial f}{\partial \varphi}\right|_{\varphi B} \quad \text{and} \quad t' = t - \frac{(\theta-\varphi_A)}{f(P_{I_B})} \quad . \tag{2.17}$$

As an example if we choose $f(P_T)$ to be linear in P_T, then $P_T = \dot{\varphi} + \varphi$. Hence,

$$P_T \propto \varphi_A + ((P_{I_B}) - \theta)(t+1) - \theta, \quad \varphi < \theta \quad ,$$

and

$$\propto \theta + (\varphi_B-\theta)\gamma e^{-\gamma t'} \qquad \varphi > \theta \quad . \tag{2.18}$$

The overshoot $P_T(\theta) - P_{TB}$ is proportional to

$$f(P_{I_B}) - f\left(\frac{P_{I_B}}{1 + (\varphi_B-\theta)^2}\right). \tag{2.19}$$

Fig. 5b depicts P(t) versus t under this approximation.

In the Appendix B, the response of the device to a linear increase in the input power has been calculated. It is seen that the increase in phase as a function of time is related to the time derivative of the logarithm of an Airy function.

2.3 THE TRANSFER AND GAIN FUNCTIONS

When using the device in the amplifier mode, it would be interesting to study the gain of the device for a small ac modulation on a dc light level. We will derive general formulae and study the broad implications. In Appendix C we will consider the simple case of a two level atomic system.

The operation of the device may be described by the transfer function $\mathcal{J}(E_T, \varphi, \theta, \Gamma)$ which connects the input and output fields, such that

$$E_I = \mathcal{J}(E_T, \varphi, \theta, \Gamma) E_T \ . \qquad 2.20$$

The function will depend upon the absorptive and refractive index properties of the medium. For a given Γ, θ and functional form of φ there is a fixed relationship between the input and output fields. By proper choice of these parameters we could use a particular characteristic curve of the device. For a given characteristic curve, it would be interesting to study the output modulation for a given input modulation on a constant light field E_{IO} so that,

$$E_{I_0} = \mathcal{J}(E_{T_0}, \varphi_0, \theta, \Gamma) E_{T_0} \ . \qquad 2.21$$

Then

$$\Delta E_I = \{\mathcal{J}(E_{T_0}, \varphi_0, \theta, \Gamma) + E_{T_0} \mathcal{J}'(E_{T_0}, \varphi_0, \theta, \Gamma)\} \Delta E_T \ , \qquad 2.22$$

where the prime denotes differentiations with respect to E_T at E_{T_0}. We could invert the Eq. 2.22 and write it as,

$$\Delta E_T = \mathcal{G}(E_{T_0}, \varphi_0, \theta, \Gamma)\Delta E_I, \qquad 2.23$$

where

$$\mathcal{G}(E_{T_0}, \varphi_0, \theta, \Gamma) = [\mathcal{J}(E_{T_0}, \varphi_0, \theta, \Gamma) + E_{T_0}\mathcal{J}(E_{T_0}, \varphi_0, \theta, \Gamma)]^{-1} \qquad 2.24$$

$\mathcal{G}$ is a complex gain function, whose significance becomes transparent if we define a 2×2 vector space in which field modulations are represented by two vectors and the gain function $\mathcal{G}$ becomes a 2×2 matrix. The upper and lower elements of the vector represent the real and imaginary amplitudes respectively, and we get

$$\begin{pmatrix} \Delta\varepsilon_T^{Re} \\ \Delta\varepsilon_T^{Im} \end{pmatrix} = \begin{pmatrix} \mathcal{G}^{RR} & \mathcal{G}^{RI} \\ \mathcal{G}^{IR} & \mathcal{G}^{II} \end{pmatrix} \begin{pmatrix} \Delta\varepsilon_I^{Re} \\ \Delta\varepsilon_I^{Im} \end{pmatrix} \qquad 2.25$$

The inner product of the vector with itself gives the energy in the modulation (but for a constant factor). In general the elements of $\mathcal{G}$ are nonvanishing, and consequently for a pure amplitude modulated input one could have an amplitude as well as frequency modulated output and vice versa.

In Appendix C the elements of the matrix in Eq. 2.25 are calculated for a two level Bloch system. In the next chapter the details of the nonlinear phase shift, its origin, dependence on the strength of the atomic transition etc. are studied.

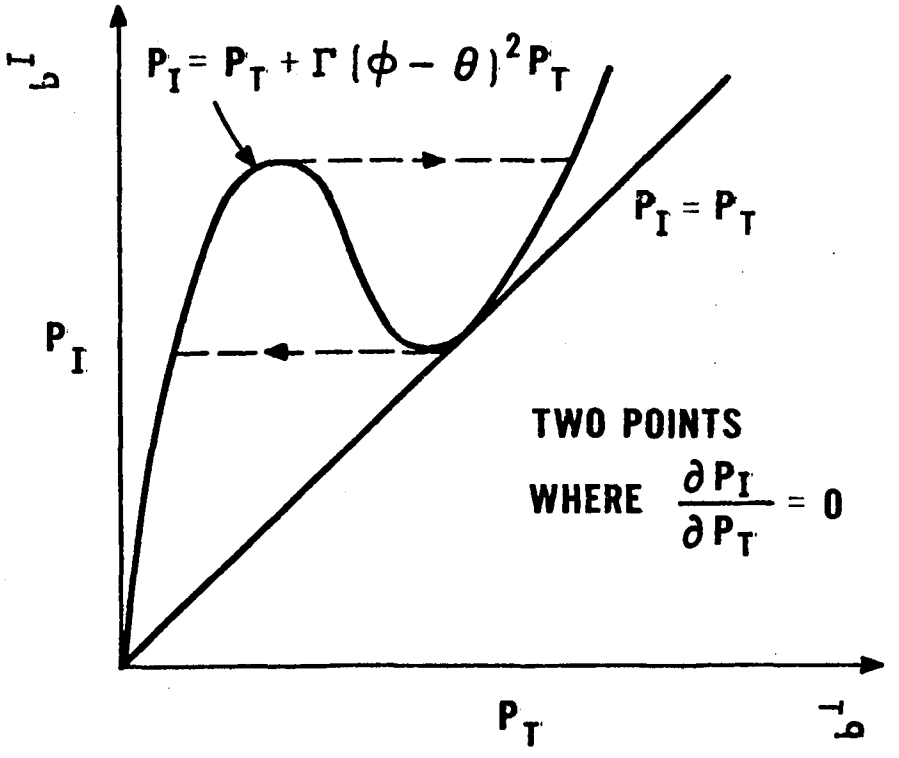

"WHICH FORMS OF ϕ (P_T) GIVE BISTABILITY?"

"ϕ (P_T) COULD HAVE ANY FUNCTIONAL FORM OTHER THAN A CONSTANT."

Figure 3

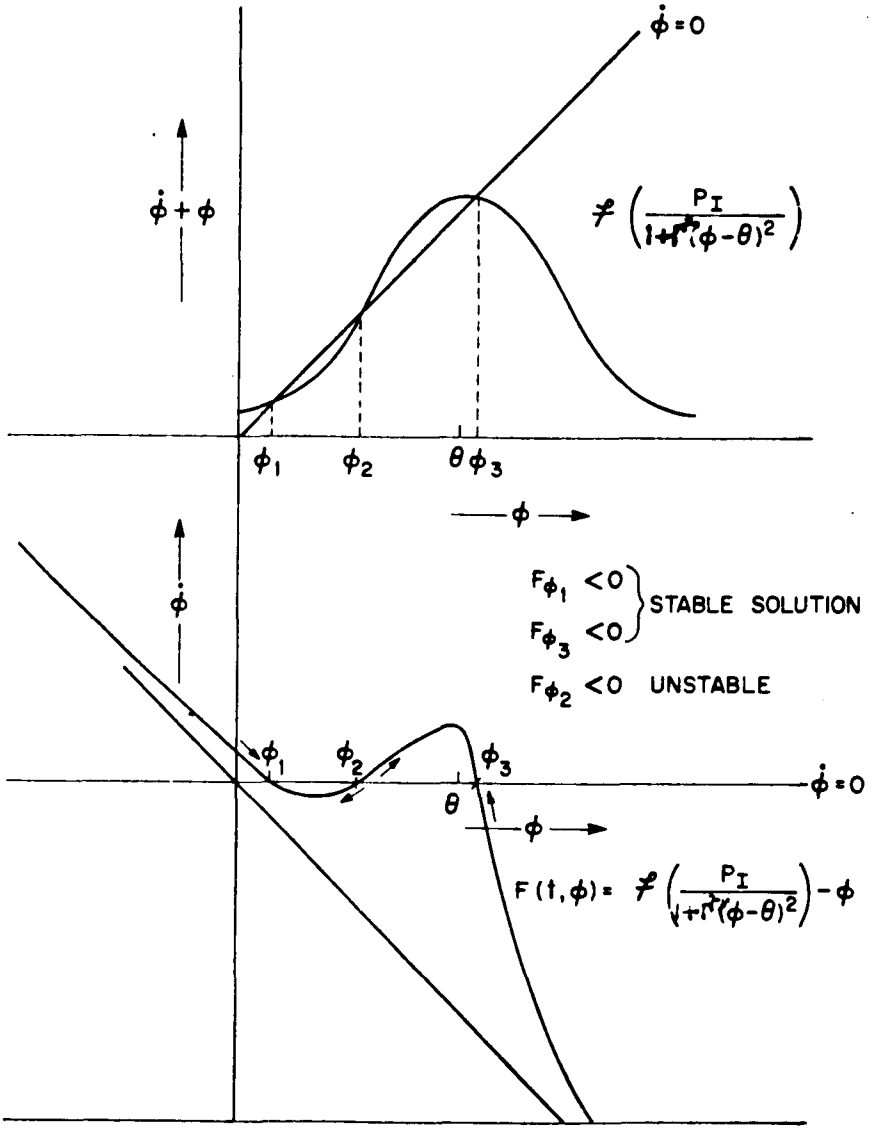
$\dot{\phi}=0$
$\dot{\phi}+\phi$
$\mathcal{L}\left(\frac{P_I}{1+\tau^2(\phi-\theta)^2}\right)$
ϕ_1
ϕ_2
θ ϕ_3
ϕ
$\dot{\phi}$
$F_{\phi_1} < 0$
$F_{\phi_3} < 0$
STABLE SOLUTION
$F_{\phi_2} < 0$ UNSTABLE
ϕ_1
ϕ_2
ϕ_3
θ
$\dot{\phi}=0$
ϕ
$F(t,\phi) = \mathcal{L}\left(\frac{P_I}{1+\tau^2(\phi-\theta)^2}\right)-\phi$

Figure 4

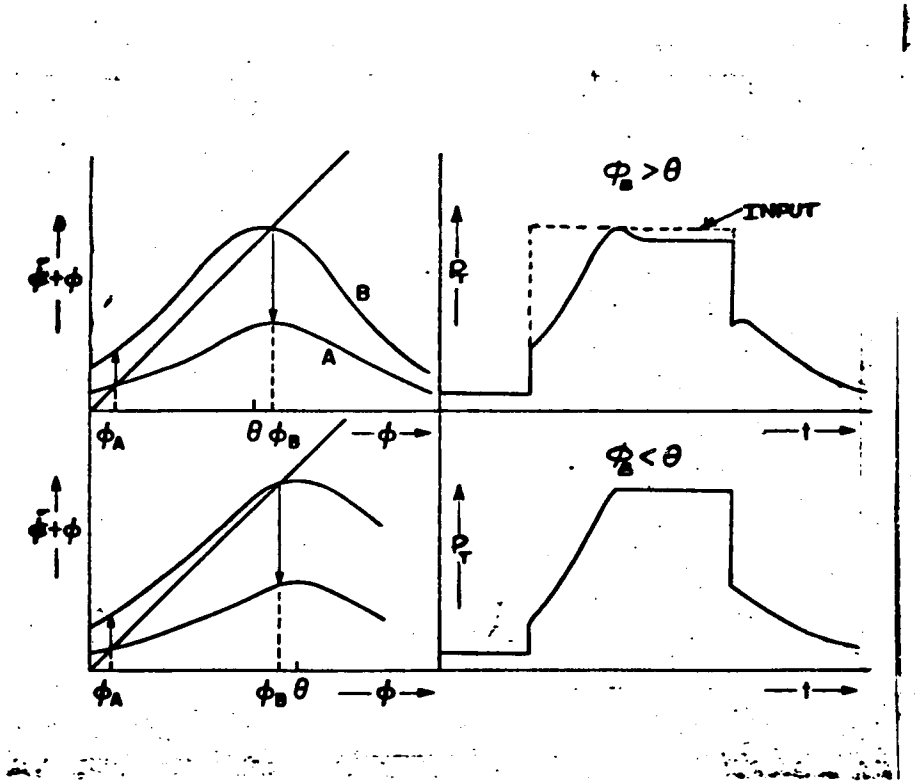

An appropriate output for a square input pulse

Figure 5a

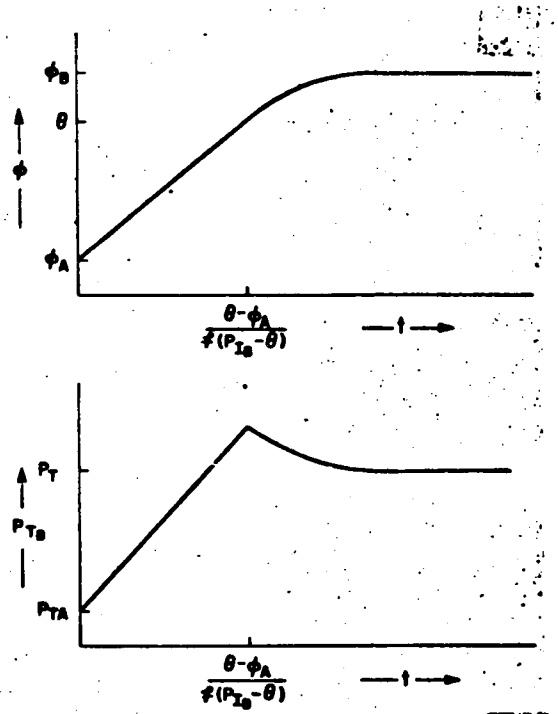

A simple mathematical fit for the overshoot

Figure 5b

CHAPTER 3

3.1 OPTICAL NONLINEARITIES IN A TWO LEVEL SYSTEM

Having enunciated the basic property of the FP interferometer, the next step is to understand the nonlinear medium. The wavelength of the light to be used, the response time, the optical power level needed and the limitation on the size of the device are to a large extent determined by the properties of the intracavity nonlinear medium. Hence it is important to study the physics of optical nonlinear refractive index and absorption. With such a goal in mind, a review of cw light propagation in a pure two level system is presented in this section. The two level atomic picture is mathematically simple to understand and is very helpful in getting insight into the various properties of the optical nonlinearities required for the device operation.

In this picture the effect of the light field on the atoms is described by Bloch's equations and the effect of the atoms on the field by the Maxwell equations. The two sets of equations are coupled and the solution for cw light propagation is obtained by solving the equations for steady state conditions. The atomic system is characterized by the resonance frequency ω_0 and the Rabi frequency per unit field $\kappa = \frac{2p}{\hbar}$ with p the dipole moment for the transition. Further, there are different relaxation times associated with the system. T_1 is the decay time of

the excited state population say, due to physical motion of atoms out of the laser beam or due to spontaneous emission. T_2' is the homogeneous dipole dephasing time such that $\frac{1}{T_2'} = \frac{1}{2T_1} + \frac{1}{T_2''}$, where T_2'' pertains to any lifetime broadening mechanism which does not significantly alter the population distribution between the two levels of the system connected with the resonance. Instead, T_2'' accounts for the broadening of either or both levels by relaxation processes that do not cause transitions between the two levels. Such broadening is produced, for example, by electric Stark or magnetic Zeeman frequency modulation of the level eigenvalues because of incoherent local field fluctuation, or phonon interaction. In addition there is the inhomogeneous dipole dephasing time T_2^* which may be due to a range of Doppler velocity shifts as in a gas, like, sodium or a statistical variation in static local cyrstalline-field potentials as in ruby at 77°K and below. Only the homogeneous line case ($T_2^* = \infty$) is considered. Interested readers may refer to Ref. 3 for details on the effect of inhomogeneous broadening.

THE BLOCH EQUATIONS FOR A HOMOGENEOUS SYSTEM

All atoms are considered alike and have the same resonant frequency. Neglecting transverse effects the electric field is chosen to be a plane wave such that,

$$E(z,t) = \varepsilon(z,t)e^{-i(kz-\omega t)} + c.c. \,, \qquad 3.1$$

where ω is the laser frequency, $k = \frac{n_0\omega}{c}$ where n_0 is a background refractive index. The electric field envelope ε is complex in the case of frequency modulation. The complex conjugate term is denoted by c.c.

In the two level approximation, the atoms interact with the electric field according to the Hamiltonian,[13]

$$\mathcal{H} = \frac{1}{2}\hbar\omega_0\sigma_z - \frac{\hbar}{2}\kappa E\sigma_x. \qquad 3.2$$

The ac Stark effect and the influence of other levels are neglected. The energy separation of the two levels is $\hbar\omega_0$ and σ_x, σ_y and σ_z are the usual Pauli spin matrices. The real and imaginary parts of the light induced polarization of the medium are represented by u and v and their values are given by $u = Np\langle\sigma_x\rangle$ and $v = Np\langle\sigma_y\rangle$, where N is the total number of atoms/cc. The fractional difference of the excited and ground state population is represented by w and $= \langle\sigma_z\rangle$ (e.g., if all atoms are in the ground state, then $w = -1$). u and v give rise to a real and imaginary refractive index $n = n_R + in_I$ such that, $n_R = \frac{2\pi}{n_0}\frac{u}{\varepsilon}$ and $n_I = \frac{2\pi}{n_0}\frac{v}{\varepsilon}$. Since u and v are nonlinear n is also nonlinear.

In the Heisenberg representation, Eq. 3.2 could be simplified[14] to $\mathcal{H} = -\hbar\underline{\sigma}\cdot\underline{H}$ where $\underset{\sim}{\sigma} = \sigma_x\hat{u} + \sigma_y\hat{v} + \sigma_z\hat{w}$ where $\hat{u}$, $\hat{v}$, $\hat{w}$ are three mutually orthogonal unit vectors

with $\hat{w} = \hat{u}x\hat{v}$. With this form for the Hamiltonian, $H = -\frac{\omega_0 \hat{w}}{2} + \frac{\kappa E \hat{u}}{2}$ and the Heisenberg equation for the time derivative of $\underline{\sigma}$ is

$$i\hbar\dot{\sigma} = [\sigma, \mathcal{H}] = i\hbar\, \underline{\sigma} \times \underline{H} \quad . \tag{3.3}$$

Eq. 3.3 yields three coupled equations from which the time variation of u, v and w could be obtained.

The problem is still not easily resolved. Two reasonable approximations are made. Firstly, the optical field is assumed to be a slowly varying envelope (SVEA) in space and time, i.e.,

$$\frac{1}{k}\left|\frac{\partial^2 \varepsilon}{\partial z^2}\right| << \left|\frac{\partial \varepsilon}{\partial z}\right| << k|\varepsilon|$$

$$\frac{1}{\omega}\left|\frac{\partial^2 \varepsilon}{\partial t^2}\right| << \left|\frac{\partial \varepsilon}{\partial t}\right| << \omega|\varepsilon| \quad . \tag{3.4}$$

Then the Maxwell equation in one spatial dimension,

$$\frac{\partial^2 E(z,t)}{\partial z^2} - \frac{n_0^2}{c^2}\frac{\partial^2 E(z,t)}{\partial t^2} = \frac{4\pi}{c^2}\frac{\partial^2 \mathcal{P}(z,t)}{\partial t^2} \quad , \tag{3.5}$$

reduces to

$$\frac{\partial \varepsilon}{\partial z} + \frac{n_0}{c}\frac{\partial \varepsilon}{\partial t} = i\frac{2\pi\omega}{n_0 c} P, \tag{3.6}$$

where $\mathcal{P}(z,t) = P(z,t)e^{-i(kz-\omega t)} + c.c.$ and $P = u + iv$ is the optically induced total polarization envelope.

The second approximation involves a transformation to a coordinate frame rotating with the angular frequency ω so that the electric field appears stationary in that frame: i.e., a rotating wave approximation (RWA). This involves neglecting terms oscillating with the frequency 2ω. This approximation involves rejecting a small shift in the resonant frequency (Bloch-Siegert shift)[15] and is a valid one for the two level atom. Without going into the details, one could use the equations from Ref. 3 and write down (with T_1, T_2' damping constants phenomenologically added[16]),

$$\dot{u} = \Delta\omega v + w\kappa\varepsilon_I - u/T_2' , \qquad 3.7a$$

$$\dot{v} = -\Delta\omega u - w\kappa\varepsilon_R - v/T_2' , \text{ and} \qquad 3.7b$$

$$Np\dot{w} = v\kappa\varepsilon_R - u\kappa\varepsilon_I - Np(w+1)/T_1 , \qquad 3.7c$$

where $\Delta\omega = \omega_0 - \omega$.

3.2 THE STEADY STATE SOLUTIONS

For cw light propagation $\dot{u} = \dot{v} = \dot{w} = \dot{\varepsilon} = 0$. From Eq. 3.6 we get (with $n = \frac{2\pi P}{n_0\varepsilon}$),

$$\frac{\partial}{\partial z}(\ell n\ \varepsilon) = \frac{i\omega n}{c} . \qquad 3.8$$

Clearly the solution for the field envelope at any coordinate z is

$$\varepsilon(z) = \varepsilon(0)e^{i(\omega/c)\int_0^z n(z')dz} , \qquad 3.9$$

which could be written at low intensities as

$$\varepsilon(z) = \varepsilon(0)e^{-\frac{\alpha(\Delta\omega)z}{2} + i\varphi}, \qquad 3.10$$

where $\alpha(\Delta\omega) = \frac{2\omega n_I}{c}$ is the absorption coefficient/unit length at the detuning $\Delta\omega$ and $\varphi = \omega n_{R/c}$ is the phase shift/unit length. Since $n_R = \frac{2\pi u}{n_0\varepsilon}$ and $n_I = \frac{2\pi v}{n_0\varepsilon}$ we can calculate their steady state values from Eq. 3.7 and we get

$$n_R = + \frac{c\alpha(0)}{2\omega} \frac{Y}{(1+Y^2+F^2)}, \qquad 3.11a$$

$$n_I = \frac{c\alpha(0)}{2\omega} \frac{1}{(1+Y^2+F^2)} \qquad \text{and} \qquad 3.11b$$

$$w = \frac{-(1+Y^2)}{(1+Y^2+F^2)} \qquad 3.11c$$

where $Y = \Delta\omega T_2'$, $F^2 = \kappa^2\varepsilon^2 T_1 T_2'$ and $\alpha(0) = \frac{2\pi\hbar N \kappa^2 \omega T_2'}{n_0 c}$.

At low intensities we get,

$$\alpha(Y) = \alpha(0) \frac{1}{(1+Y^2)}. \qquad 3.12$$

Needless to say, the bistable device that we are talking about uses these nonlinear indices. Both n_R and n_I change with intensities and go to zero at large intensities (saturation). For the nonlinear refractive device n_R must change sufficiently to cancel the initial mistuning . But for the nonlinear absorptive device, n_I must go to zero. On this basis, the refractive index device might have a lower threshold of operation. Further, far off resonance n_R is proportional

to Y^{-1} whereas n_I is proportional to Y^{-2}. Hence the refractive index nonlinearity spans a wider optical frequency range, and would enable the device to operate with the optical frequency quite a bit off-resonance.

Far off resonance, the nonlinear refractive index can be expanded in powers of E^2 and we get

$$n_R = n_R^0 + n_2 E^2, \qquad 3.13a$$

where $n_R^0 = + \dfrac{\pi \hbar N \kappa^2 T_2'}{n_0 c (1+Y^2)}$ and

$$n_2 = - \frac{4\pi N \hbar T_1 T_2'^2 \kappa^4}{n_0 c (1+Y^2)^2} \quad . \qquad 3.13b$$

Hence we get a second order nonlinear index coefficient, equivalent to the Kerr constant.

From Eq. 3.11 it is seen that a light beam passing through the medium is phase shifted by an amount $\Phi = \dfrac{n_R \omega}{c}$ per unit length. This phase could also be written using Eqs. 3.8c and 3.11 as,

$$\varphi = \frac{\alpha Y}{2} \left(\frac{1 + Y^2}{1 + Y^2 + F^2} \right) = - \frac{\alpha Y}{2} \, w. \qquad 3.14$$

If as in Chapter 2, φ is defined to be zero at low light intensity, (since this could be assimilated in the initial detuning θ), we can define φ as $\varphi(I) - \varphi(0)$. Then the nonlinear phase shift is

$$\varphi = - \alpha Y \frac{(1+w)}{2}. \qquad 3.15$$

It is clear that $\frac{(1+w)}{2}$ is the fraction of excited state atoms and $-\alpha Y$ is the phase shift per excited atom.

3.3 EFFECT OF A NONRESONANT HOMOGENEOUS BAND

A consequence of the ruby experiment (Chapter 5) is that one could have nonlinear phase shift contribution from nonresonant, but strong homogeneous absorption bands. So besides the two sharp levels separated by ω_0, let us assume a band centered far off at $\bar{\omega}_0$ with a Lorentzian profile $\bar{\alpha}(\omega)$ of width $\overline{\Delta\nu}$ (FWHM). The homogeneous dipole dephasing time $\bar{T}_2' = 2/\overline{\Delta\nu}$. Associated with this absorption would be a refractive index and hence a phase profile so that, a light wave at frequency ω will be phase shifted by $\varphi(\omega)$.

To calculate this phase shift, let us divide the absorption band into segments of width $d\nu$, centered at $\overline{\omega_0} + \nu$ where $\nu = 0$ corresponds to the band center. Then the absorption due to this band at a frequency ω is (could be proved by perturbation theory)

$$\delta\alpha(\omega) = \frac{\bar{T}_2'}{\pi} \frac{\bar{\alpha}(\bar{\omega}_0+\nu)d\nu}{\{1 + (\bar{\omega}_0+\nu-\omega)^2\bar{T}_2'^2\}}, \qquad 3.16$$

$\frac{\bar{T}_2'}{\pi}$ is a normalization factor and the denominator takes into account the effect of being off-resonant. This will contribute a phase

$$\delta\varphi(\omega) = + \frac{\bar{T}_2'}{\pi} \frac{\bar{\alpha}(\bar{\omega}_0+\nu)(\bar{\omega}_0+\nu-\omega)\bar{T}_2' \, d\nu}{\{1 + (\bar{\omega}_0+\nu-\omega)^2\bar{T}_2'^2\}} \quad . \tag{3.17}$$

Hence the total contribution due to the band is

$$\varphi(\omega) = + \frac{\bar{T}_2'^2}{\pi} \int_{-\infty}^{\infty} \frac{\bar{\alpha}(\bar{\omega}_0+\nu)(\bar{\omega}_0+\nu-\omega)d\nu}{\{1 + (\bar{\omega}_0+\nu-\omega)^2\bar{T}_2'^2\}} \tag{3.18}$$

If the band is sufficiently far off resonance so that $|\omega-\bar{\omega}_0| > \overline{\Delta\nu}$ and $(\bar{\omega}_0-\omega)T_2' > 1$, we could approximate Eq. 3.18 by

$$\varphi(\omega) = + \frac{\frac{1}{\pi}\int_{-\infty}^{\infty} \bar{\alpha}(\bar{\omega}_0+\nu)d\nu}{(\bar{\omega}_0-\omega)} \quad . \tag{3.19}$$

An implicit assumption has been that the number of atoms excited to these bands is negligible. This phase/unit length of the sample could be nonlinear, depending upon the number of atoms excited. The phase shift with the atom in the ground state is

$$\varphi^g = \frac{1}{\pi} \frac{\int \bar{\alpha} d\nu}{(\bar{\omega}_0-\omega)} \quad . \tag{3.20}$$

However the phase shift with an atom in the excited state

$$\varphi^e = \frac{1}{\pi} \frac{\int \bar{\alpha}_0 d\nu}{(\bar{\omega}_0-\omega-\omega_0)} \quad , \tag{3.21}$$

where the absorption profile looks different to an excited

state atom and further the laser frequency is upshifted by the two level resonant frequency.

Hence the nonresonant contribution to the nonlinear phase shift, adjusted to be zero at low light intensity is,

$$\varphi(I) = (\varphi^e - \varphi^g)\,\frac{(1+w)}{2}\,. \qquad 3.22$$

As will be seen in Chapter 5, in ruby there was a significant nonresonant contribution to the nonlinear phase shift and this resulted in the room temperature operation of the device, which was not anticipated. If the band is not homogeneous then the analysis becomes difficult, $\bar{T}_2' \neq \frac{2}{\Delta\nu}$ and the inhomogeneous distribution function must be included in the integral.

3.4 GAIN OF A SMALL MODULATION

Typically, the device is in operation with a dc level of light, and a small modulated (amplitude or frequency) optical signal, not necessarily at the same frequency, is applied through a third port. To study the effect of this signal on the transmitted light, one must understand how the intracavity nonlinearity is modulated for a change in the cavity field. Let us consider a nonlinear medium described by the Eq. 3.7 and try to calculate the incremental change in the indices for a small change in the steady field ε_0. The increase in the field is $\Delta\varepsilon$, which is in

general complex, in order to take into account both amplitude and frequency modulation. Linearizing about the steady state values, ε_0, u_0, v_0 and w_0 we get from 3.7,

$$\frac{d}{dt}\Delta u = -\Delta\omega\Delta v - \frac{\Delta u}{T_2'} + w_0\kappa\Delta\varepsilon_I \qquad 3.23a$$

$$\frac{d}{dt}\Delta v = \Delta\omega\Delta u - \frac{\Delta v}{T_2'} - \Delta w\,\kappa\varepsilon_0 - w_0\kappa\varepsilon_R \qquad 3.23b$$

$$\frac{d}{dt}\Delta w = -\frac{\Delta w}{T_1'} + \kappa\varepsilon_0\Delta v + v_0\kappa\Delta\varepsilon_R - u_0\kappa\Delta\varepsilon_I \qquad 3.23c$$

If we consider a simple, amplitude modulation

$$\Delta\varepsilon_R = \mathrm{Re}\,\mathcal{E}e^{i\nu t} \quad \text{and} \quad \Delta\varepsilon_I = 0. \qquad 3.24$$

Then Eqs. 3.23 yield

$$\Delta n_R = -\mathrm{Re}G_R(\Delta\omega,\nu)\kappa T_2'\frac{\mathcal{E}e^{i\nu t}}{\varepsilon_0}, \qquad 3.25$$

where

$$G_R(\Delta\omega,\nu) = -\frac{ixY\{F^2 + (1+iax)(2+ix)\}}{(1+Y^2+F^2)[(1+ix)^2(1+iax)+(1+iax)Y^2+(1+ix)F^2]} \qquad 3.26$$

and $Y = T_2'\Delta\omega$ and $x = T_2'\nu$.

Similarly,

$$\Delta n_I = -\mathrm{Re}\,G_I(\Delta\omega,\nu)\kappa T_2'\frac{\mathcal{E}e^{i\nu t}}{\varepsilon_0}, \qquad 3.27$$

where

$$G_I(\Delta\omega,\nu) = \frac{2(1+ix)F^2 + ix(1+ix-Y^2)(1+iax)}{(1+Y^2+F^2)[(1+ix)^2(1+iax)+(1+iax)Y^2+(1+ix)F^2]} \quad . \quad 3.28$$

If the absorption line is inhomogeneously broadened and described by a distribution function $g(\Delta\omega)$ then the gain functions in Eqs. 3.26 and 3.28 could be redefined as,

$$G(\nu,F,a,g(\Delta\omega)) = \frac{\int g(\Delta\omega)G(\Delta\omega,\nu)d(\Delta\omega)}{\int g(\Delta\omega)G(\Delta\omega,0)d(\Delta\omega)\Big|_{F=0}} \qquad 3.29$$

where, now $\Delta\omega$ has been reinterpreted as the frequency detuning of a homogeneously broadened isochromat from the laser frequency assumed to be ω_0. In Ref. 3 the case of a Gaussian distribution function is treated and the gain function for the absorption has been calculated. It is seen that the gains seem to peak at the Rabi frequency and decrease with increase in inhomogeneous broadening.

3.5 THE BISTABLE DEVICE PROBLEM FOR A TWO LEVEL INTRACAVITY NONLINEAR SYSTEM

The interferometer consists of two mirrors of reflectivity R and transmission T separated by a distance L. A homogeneously broadened absorber, comprised of stationary atoms, that absorbs light of weak intensity at

frequency ω_0 is placed between the plates. Light of frequency ω is incident from the right. The electric field envelopes are ε_I, incident from the right; ε_R, reflected to the right; ε_F, inside the cavity, moving to the left; ε_B, inside the cavity, moving to the right; ε_T, transmitted from the cavity moving to the left. The intracavity field may be written as

$$E(z,t) = \varepsilon_F e^{i\varphi_F} e^{-i(\omega t+kz)} + \varepsilon_B e^{i\varphi_B} e^{-i(\omega t-kz)} + c.c., \qquad 3.30$$

where ε_F and ε_B are taken to be real and independent of time. Using the SVEA in the spatial coordinates in the wave equation one gets (Ref. Eq. 3.6).

$$\frac{\partial}{\partial z}(\varepsilon_F e^{i\varphi_F}) - \frac{\partial}{\partial z}(\varepsilon_B e^{i\varphi_B}) e^{2ikz} = \frac{i2\pi\omega}{n_0 c} P\, e^{ikz}. \qquad 3.31$$

The determination of the polarization P requires the quantity

$$E^2_{\text{time}} = 2\varepsilon_F^2 + 2\varepsilon_B^2 + 2\varepsilon_F \varepsilon_B e^{-2ikz+i\Delta\varphi} + 2\varepsilon_F \varepsilon_B e^{2ikz-i\Delta\varphi}, \qquad 3.32$$

where $\Delta\varphi = \varphi_F - \varphi_B$.

Because of the formation of standing waves inside the cavity there could be a rapid variation of u and v in a light wavelength, so that SVEA must be used with care. The intracavity polarization P may be written as

$$P = \left(\frac{N\hbar\kappa^2 T_2'}{2} \right) \frac{(\varepsilon_F e^{i\varphi_F} e^{-ikz} + \varepsilon_B e^{i\varphi_B} e^{ikz})\ (Y+i)}{1 + Y^2 + T_1 T_2' \kappa^2 \langle E^2 \rangle_{time}}\ , \qquad 3.33$$

which may be written as a Fourier sum,

$$P = \left(\frac{N\hbar\kappa^2 T_2'}{2} \right) (Y+i)\ (\varepsilon_F e^{i(\varphi_F - kz)} + \varepsilon_B e^{i(\varphi_B + kz)})(\sigma(0) +$$

$$+ \sigma(2k) e^{-2ikz + i\Delta\varphi} + \sigma(-2k) e^{2ikz - i\Delta\varphi} + \ldots.). \qquad 3.34$$

Thus

$$\sigma(0) = A^{-1}(1-b^2)^{-\frac{1}{2}} \qquad 3.35$$

and

$$\sigma(2k) = \sigma(-2k)^* = A^{-1}b^{-1}[1 - (1-b^2)^{-\frac{1}{2}}], \qquad 3.36$$

where

$$A = 1 + Y^2 + T_1 T_2' \kappa^2 \{\varepsilon_F^2 + \varepsilon_B^2\} \quad \text{and}$$

$$b = 2T_1 T_2' \kappa^2 E_F E_B A^{-1}.$$

Substituting 3.32 and 3.34 in the Maxwell Eq. 3.31 we get,

$$\frac{\partial \varepsilon_F}{\partial z} = \frac{\alpha}{2} \sigma(0)\ \varepsilon_F + \frac{\alpha}{2}\ \sigma(2k)\ \varepsilon_B(\cos \Delta\varphi - Y \sin \Delta\varphi) \qquad 3.37a$$

$$\frac{\partial \varepsilon_B}{\partial z} = -\frac{\alpha}{2} \sigma(0)\ \varepsilon_B - \frac{\alpha}{2} \sigma(2k)\ \varepsilon_F(\cos \Delta\varphi + Y \sin \Delta\varphi) \qquad 3.37b$$

$$\frac{\partial \Delta\varphi}{\partial z} = -\alpha Y \sigma(0) - \frac{\alpha}{2}\sigma(2k)\left\{ Y \cos\Delta\varphi \left(\frac{\varepsilon_B}{\varepsilon_F} + \frac{\varepsilon_F}{\varepsilon_B} \right) + \sin\Delta\varphi \left(\frac{\varepsilon_B}{\varepsilon_F} - \frac{\varepsilon_F}{\varepsilon_B} \right) \right\} .$$

3.37c

These three equations describe the interaction of two counter propagating electric fields inside a medium. The two fields are coupled by $\sigma(2k)$ which could be called the 'standing wave diffraction grating function' and it controls the energy exchange between the beams. Contributions from waves varying as $e^{-3i\omega t}$ or as e^{-3ikz} are neglected and no motion of the absorbing atoms is allowed.

The mirrors determine the boundary conditions and at $z = 0$ at the left mirror $\varepsilon_T = \sqrt{T}\,\varepsilon_F$ and $\varepsilon_B = \sqrt{R}\,\varepsilon_F$. At the right mirror, $z = L$ and we can write down a unitary transformation

$$\begin{pmatrix} \varepsilon_F e^{i\varphi_F} \\ \varepsilon_R \end{pmatrix} = \begin{pmatrix} \sqrt{T} & Re^{i\theta} \\ -Re^{-i\theta}\sqrt{T} & \end{pmatrix} \begin{pmatrix} \varepsilon_I \\ \varepsilon_B e^{i\varphi_B} \end{pmatrix}$$

which determines the boundary conditions there.

The details of the solution are in Appendix D and just the over all scheme will be described here. Since the input is a single valued function of the

output it is easier to solve for P_I as a function of P_T. For a given P_T, the quantities ε_F, ε_B and $\Delta\tau$ are known through the boundary conditions at $z = 0$. Solving Eqs. 3.7, ε_F, ε_B and $\Delta\tau$ at $z = L$ may be obtained by iteration. At $z = L$,

$$P_I = \frac{\varepsilon_F^2 + R\varepsilon_B^2 - 2\sqrt{R}\,\varepsilon_F\varepsilon_B \cos(\Delta\tau - \theta)}{T} . \qquad 3.39$$

Computer plots have been made using the above procedure with R, θ, Y and α as variable parameters. In Fig. 6 a comparison is made between a calculation using the simple model of Chapter 2, and the above model. The tractable model of Chapter 2 did not include the spatial modulation of the nonlinearity due to the standing waves whereas the iterative model does include these effects through the $\sigma(2k)$ term. Presumably, due to this, the iterative model gives lower thresholds as seen in Fig. 6. The qualitative features are the same in both models.

Bloch Model (including standing waves).

R	Ø	$\Delta\omega T_2'$	ΔZ	$\alpha L/2$	P_{max}
0.9100000	0.2500000	2.4500000	0.0200000	1.4100000	10.000
0.9100000	0.1500000	2.4500000	0.0200000	1.4100000	10.000
0.9100000	0.0500000	2.4500000	0.0200000	1.4100000	10.000
0.9100000	0.0100000	2.4500000	0.0200000	1.4100000	10.000
0.9100000	0.	2.4500000	0.0200000	1.4100000	10.000
0.9100000	-0.0100000	2.4500000	0.0200000	1.4100000	10.000
0.9100000	-0.0500000	2.4500000	0.0200000	1.4100000	10.000
0.9100000	-0.1500000	2.4500000	0.0200000	1.4100000	10.000
0.9100000	-0.2500000	2.4500000	0.0200000	1.4100000	10.000

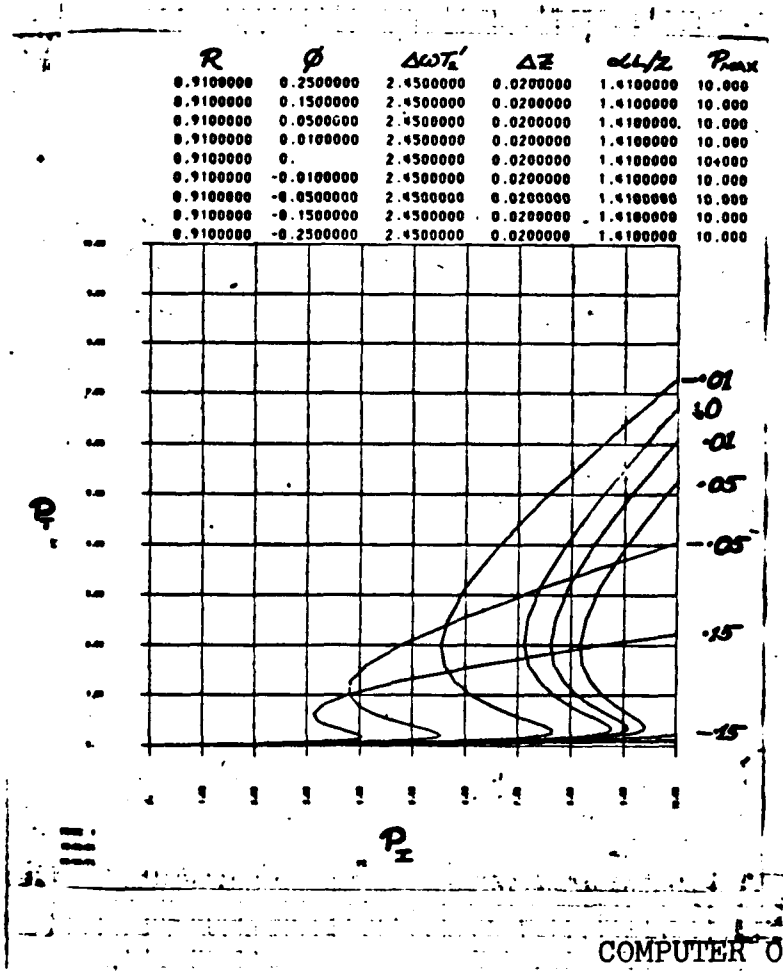

Using Eq.2.3 (no standing waves).

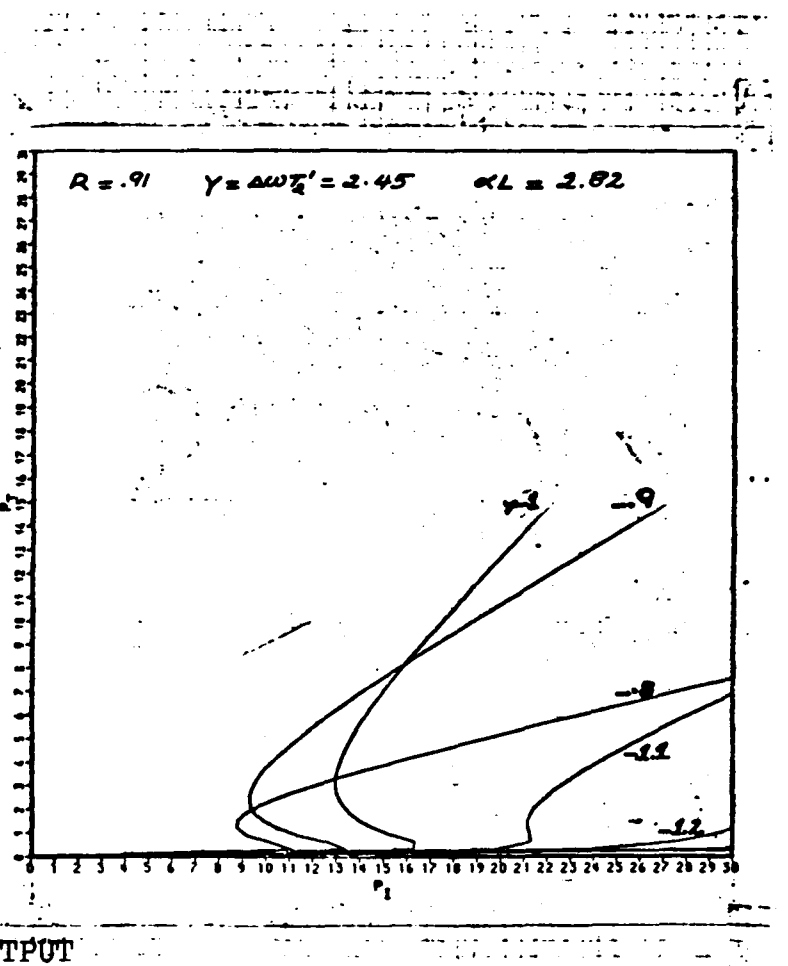

COMPUTER OUTPUT

Figure 6

CHAPTER 4

BISTABILITY AND DIFFERENTIAL GAIN IN A SODIUM-FILLED FABRY-PEROT INTERFEROMETER

4.1 INTRODUCTION

In the initial stages of the sodium vapor experiment[5] we were aware only of the absorptive bistability. The Doppler broadening of the sodium lines hence presented a conceptual problem. The saturation mechanism is the optical pumping of the sodium atoms in the F = 1 (or 2) ground state to the F = 2 (or 1) ground state (Fig. 7). For most laser frequencies, atoms tuned to resonance by the Doppler effect saturate at very low power, and recovery (T_1 process) occurs only after unpumped atoms enter the laser beam region. At higher powers, the resultant velocity hole widens in proportion to the driving field (power broadening). Because the absorbed power is consequently approximately linear in the driving cavity field, one did not expect the device to work. It is only at high powers, where even the wings of the Doppler line are partially saturated, that one expected the device to work.

To make the absorber homogeneous and also to prevent detrimental condensation of the sodium vapor on the mirror surfaces argon was to be used as a buffer gas. As will be discussed later, the results were dramatic without argon and in fact deteriorated with the addition of buffer gas. With further experimental support it was

realized that the nonlinear refractive index of the D line was making the device work. The origin of the nonlinear refractive index was the reshuffling of the ground state population between the hyperfine states due to the optical pumping. The phase shift imposed upon the optical field by an atom depends upon which ground hyperfine state the atom is in. Since the ground state population is sensitive to the light intensity one obtains a nonlinear phase shift.

Explicit calculation of the nonlinear phase shift due to the sodium D_2 transition was made.[18,19] The maximum nonlinear phase is the difference in the phase obtained by assuming the ground state hyperfine populations with Boltzman distribution to that obtained by assuming the atoms to be optically pumped completely into one of the ground state hyperfine levels. As a function of the light frequency and intensity the nonlinear phase varies between zero and the maximum value that we had calculated as shown in Fig. 8. There are three different frequencies for which the phase is not intensity dependent. At the frequency ν_1 exactly halfway between the two ground state hyperfine levels, the cross over frequency, there is no intensity dependent population change. At the other two frequencies, ν_2 and ν_3, there is no difference in the phase due to the two ground state levels. Hence at these frequencies we do not expect any nonlinear phase shift, and the device must work purely with nonlinear absorption.

4.2 THE SODIUM EXPERIMENT

A tunable jet-stream dye laser (with a folded cavity[21] configuration) was used, with an argon laser as the pump (Fig. 9). The 50 mW single mode output was controllable in frequency by 3 etalons inside the laser cavity. The dye laser is described elsewhere.[20]

The frequency jitter of the feedback-locked output was less than 2 MHz. The dye laser intensity was varied from zero to its maximum value by a Zenith (M-40R) acousto optic modulator (to plot directly the output versus input curve). The modulator further changed the frequency of the return beam through it by 80 MHz (twice the frequency of the diffracting acoustic carrier in the modulator) and thus prevented any instabilities from feeding back into the dye laser. A servo-system was used with the modulator to cut down intensity fluctuations to less than 1%. The beam had a diameter of 1.65 mm and a maximum power of 13 mW before the device.

The device consisted of a 11 cm FP interferometer with Na vapor at 10^{-4} to 10^{-5} Torr pressure (LN_2 trapped diffusion pump) in the 2.5 cm region midway between the mirrors. The sodium vapor was contained in a copper cell with heaters around it. (The sodium density was varied by changing the servo-controlled cell temperature.) The 90% reflecting mirrors were at the end of narrow tubes coming from the cell. The cold narrow tubes reduced detrimental

condensation of sodium on the mirror surfaces. The optical transmission of the properly tuned FP without sodium vapor was about 45% and we attributed the loss to the nonflatness of the mirror surfaces and small sodium deposits on the mirrors. The transmitted and incident intensities were displayed as vertical and horizontal deflections on an oscilloscope. The vertical gain of the scope was adjusted so that the empty FP input-output relationship was a 45° line.

Absolute frequency calibration of the dye laser with respect to the sodium hyperfine lines was very accurately done with a saturation spectroscopy setup.[22,23] We had sodium vapor (at about 10^{-5} Torr) in a pyrex cell. Heater tapes were wound around the cell and the absorption was thereby varied. The laser beam was split into 2 beams, a strong and a weak one (Fig. 10). The strong one was aligned to go back on itself after attenuation, providing the saturation signal; the weak one served as a reference to eliminate noise. The cell was placed in between a pair of Helmholtz coils putting out a sinusoidal ±40 Gauss peak field, with the axis of the coil along the light beam. A circular polarizer with a crossed polarizer was placed in front of the cell to prevent feedback to the laser. By varying the laser frequency a saturation signal was obtained at each of the hyperfine lines and an inverted signal at the cross-over points, which occurred exactly in between the set of hyperfine states, separated by the ground state splitting. Cross-overs also occurred in between the

excited state separation. These signals served as excellent frequency standards and we knew the frequency of the laser accurately to within 10 MHz.

The laser was then locked to an evacuated FP containing a set of confocal mirrors of 15 cm radius. The evacuated FP feedback provided a fast frequency stability of 2 MHz, though it had a drift of 100 MHz/hour.

4.3 RESULTS AND DISCUSSIONS

The presence of nonlinearity and the availability of sufficient light intensity to observe the nonlinearity were established by looking at the transmission of the sodium vapor without the cavity mirrors. In Fig. 11 the effect of saturation is seen and the fact that the curve does not have a unity slope at higher input intensities is due to the Doppler broadening. On putting the mirrors back on the FP and peaking up the finesse of the cavity bistable curves were seen. Figure 12 is one such bistable curve. With the FP in the scanning mode the outputs were asymmetric. The direction of the asymmetry depended upon the sign of the nonlinear index, and in Fig. 13 the change in the index sign is shown for different laser frequencies. There were three frequencies where the nonlinear index was zero (i.e., the FP outputs were symmetric): about 400 MHz below the transitions from the ground state F = 2, (ν_2) at the cross over halfway between F = 1 and F = 2 (ν_1) and about 300 MHz above the F = 1 transition (ν_3). As mentioned earlier, the

theoretical calculations (Fig. 8) do indicate the absence of nonlinear refractive index at these frequencies. At 400 MHz below the ground state F = 2 transitions, purely absorptive bistability[1,2,3,4] was seen with the highest available laser power. On the other hand the nonlinear index bistability was quite dramatic at much lower powers. In Fig. 14 the effect of changing the initial mistuning of the FP, (with the mistuning in units of frequency) is shown. The surprisingly small frequency shifts of the FP, with only a 2 MHz laser stability was possible as these data were taken quite rapidly and also the experiment was done at times when the ambient room temperature variation was at a minimum. (There were typically two such minima/day, one at 6-8 p.m. and the other at 6-8 a.m.). By varying the absorption, and the cavity detuning the transistor or ac gain curve (Fig. 15) and the clipper characteristic (Fig. 16) were seen. On the ac gain characteristic a 500 Hz modulation was amplified by a factor of 5, but because of the inherent loss of the cavity the overall gain was about 2.5. The reflected output of the clipper displayed a limiter characteristic.

Occasionally, multiple states like in Figs. 17 and 18 were seen. By using an aperture on the output and moving it around, it was found that these were transversely independent curves. On looking into the cell through a viewing port one could see filamentation as reported by Ashkin and Bjorkholm.[19] It was concluded that these

transverse filaments acted independently of each other. This process is very suggestive of a futuristic optical device with the several transverse optical beams producing multiple device action in a single unit.

Addition of a buffer gas (argon) considerably increased the bistability threshold. This is because collisions with argon make the absorption line of sodium more homogeneous. Nonlinear index effects were decreased and the absorption became harder to saturate. A typical absorptive bistability in the presence of the buffer gas is shown in Fig. 19.

SWITCHING TIMES:

With the device in the bistable mode, square, sinusoidal and triangular optical inputs were used (Fig. 20). The observed "turn-on" (transition from weakly to highly transmitting operation in the bistable mode) times were 1-10 μsec. These times are approximately the time required for the intracavity field to optically pump the sodium atoms. The turn on times were shortest when the input was abruptly changed to its highest value. Turn off times were typically 20 to 50 μsec. A thermal atom crosses the 1.65 mm beam in 5 μsec; thus the effective saturated diameter is several times larger. In some of the switch on curves overshoots were seen; a typical characteristic of nonlinear refractive index bistability.

The experimental results agreed qualitatively well with the theoretical results obtained by using a homogeneous, two level atomic system described by the Bloch equations. The sodium experiment revealed the possibility of making lower threshold devices with a wider optical frequency response, using the nonlinear refractive index of the intracavity media. Further, the absorption loss in such a device may be very small. In retrospect, a smaller and faster device could have been made by using a one mm long cell and increasing the sodium density 100 times. Further, by using a focussed beam and a spherical cavity the beam transit time could have been made as fast as a few nanoseconds. Of course, the sodium absorption line may then be different due to collisions.

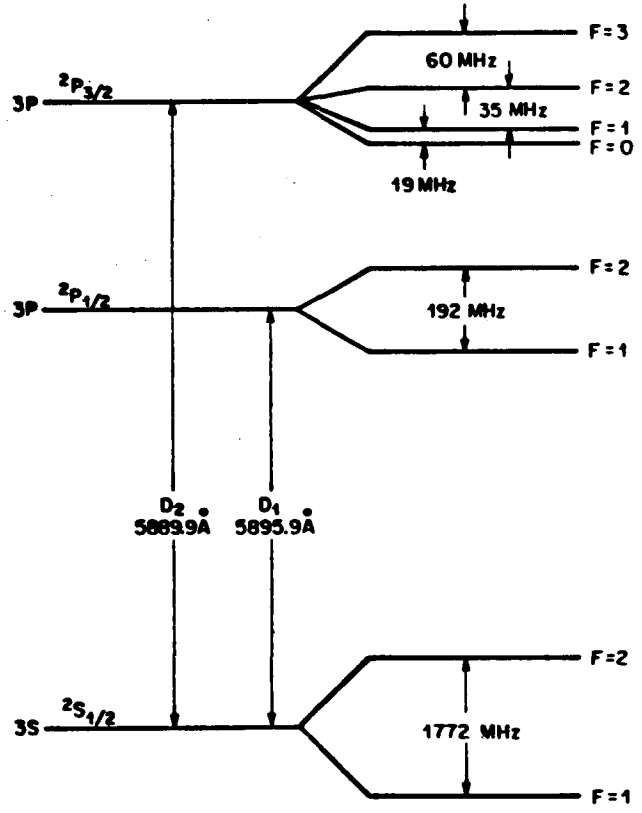

HYPERFINE ENERGY LEVEL STRUCTURE

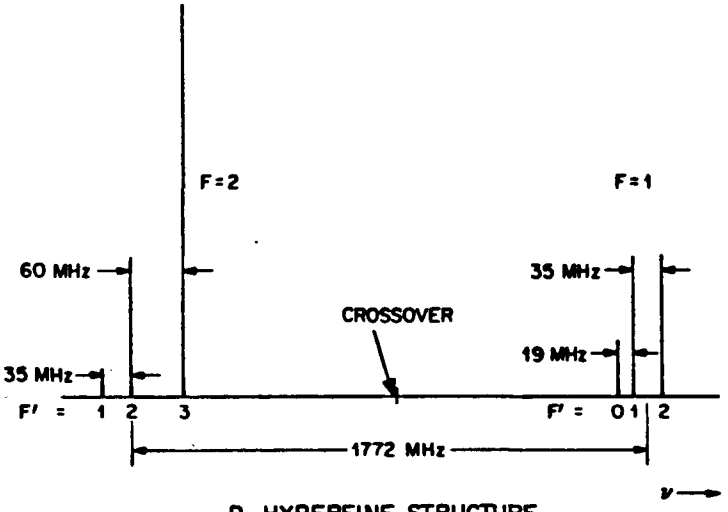

D_2 HYPERFINE STRUCTURE

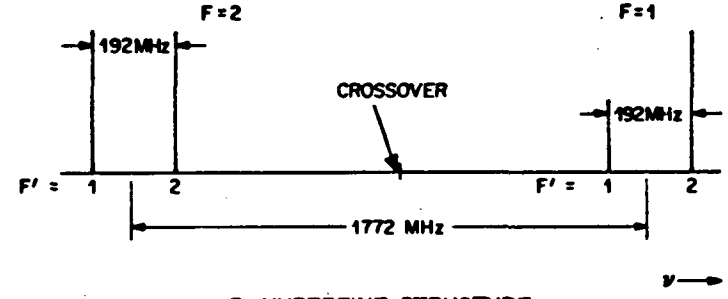

D_1 HYPERFINE STRUCTURE

Sodium energy level diagram and transition

Figure 7

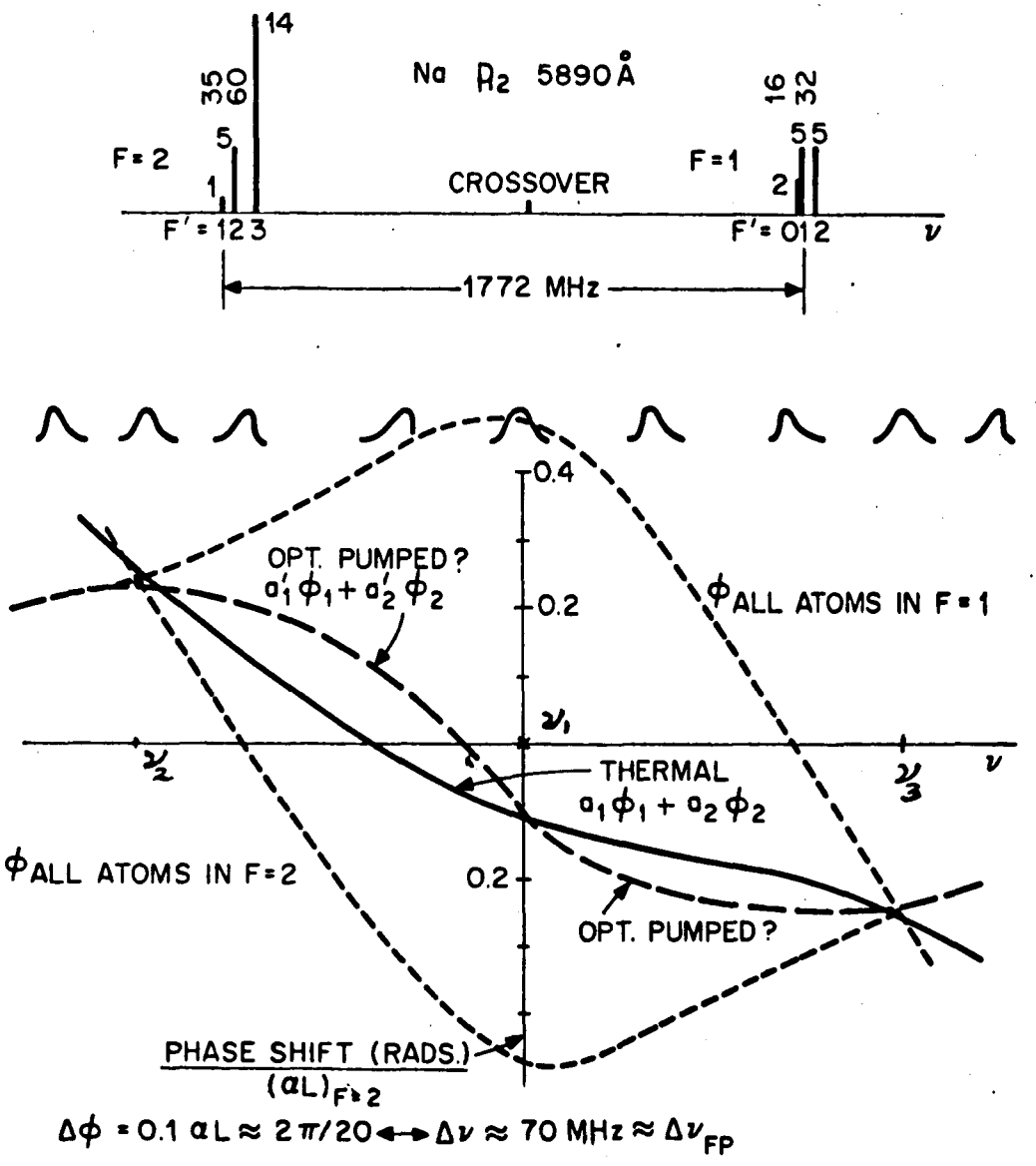

Nonlinear dispersion in sodium D_2 line as a function of laser frequency

Figure 8

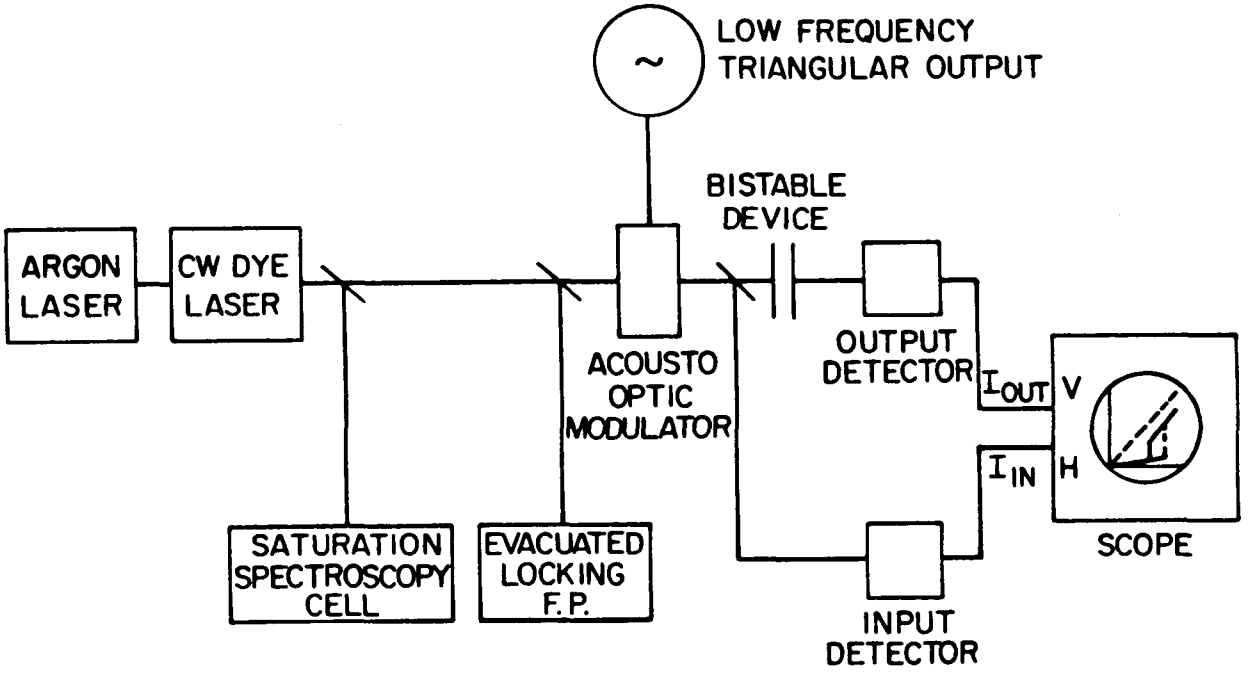

EXPERIMENTAL SETUP

Figure 9

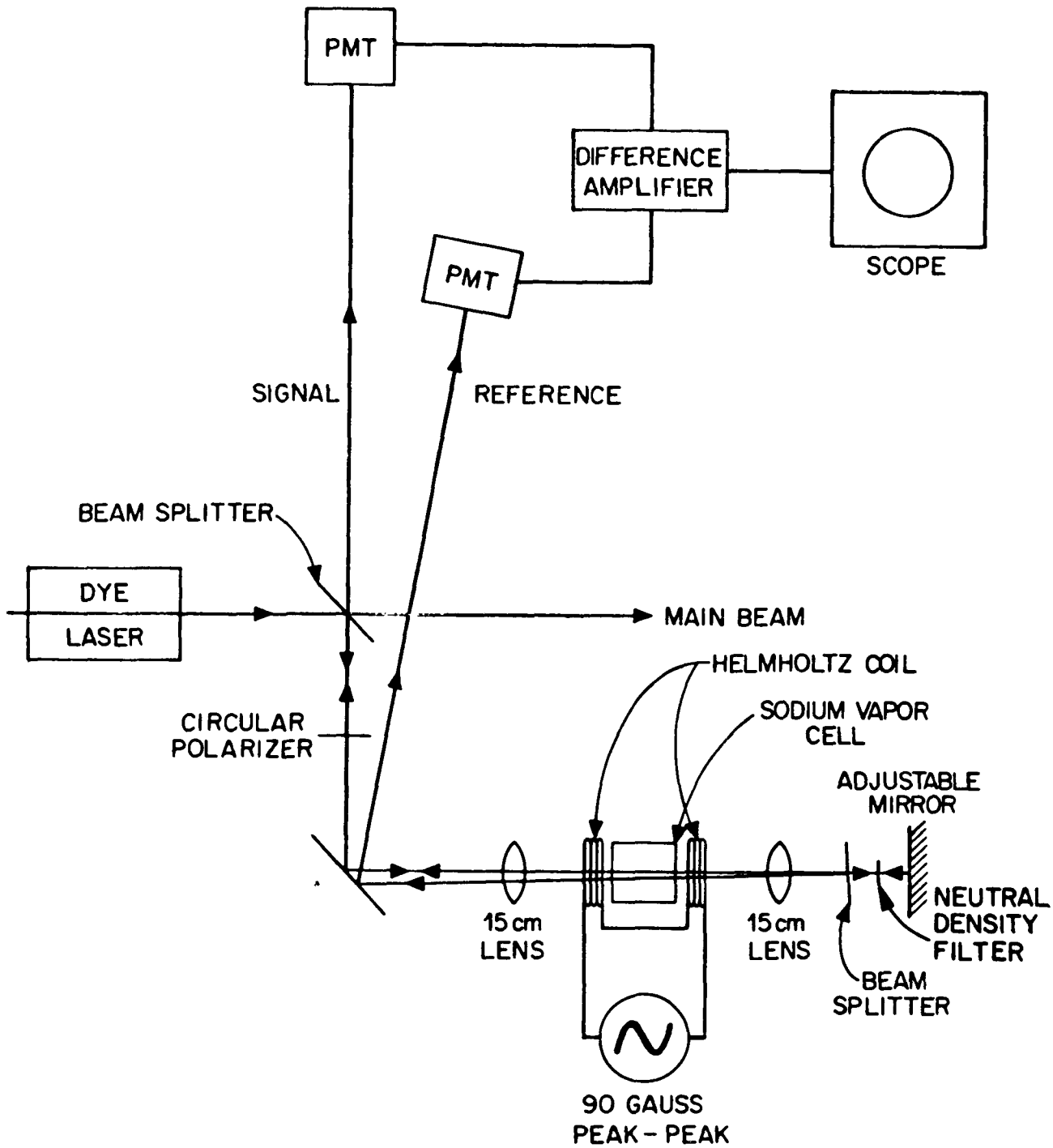

SATURATION SPECTROSCOPY SETUP

Figure 10

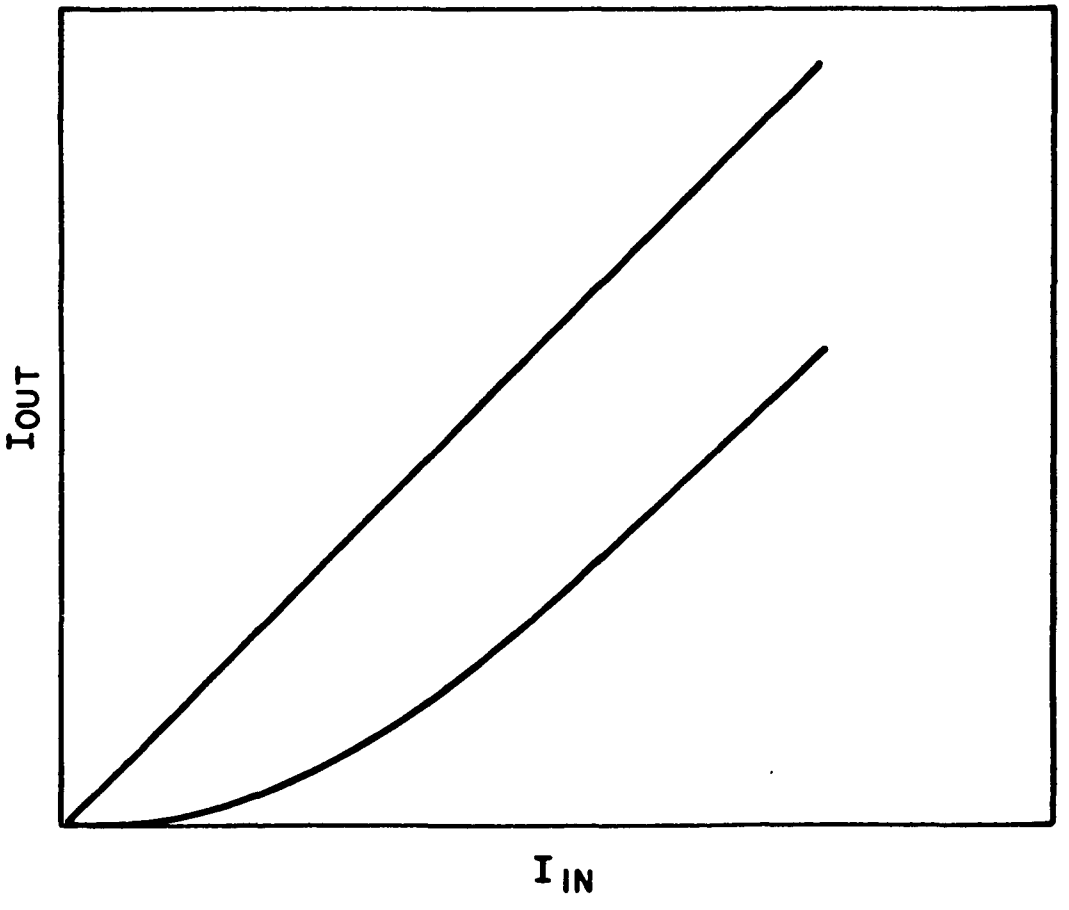

SATURATION WITHOUT A FABRY-PEROT CAVITY

Figure 11

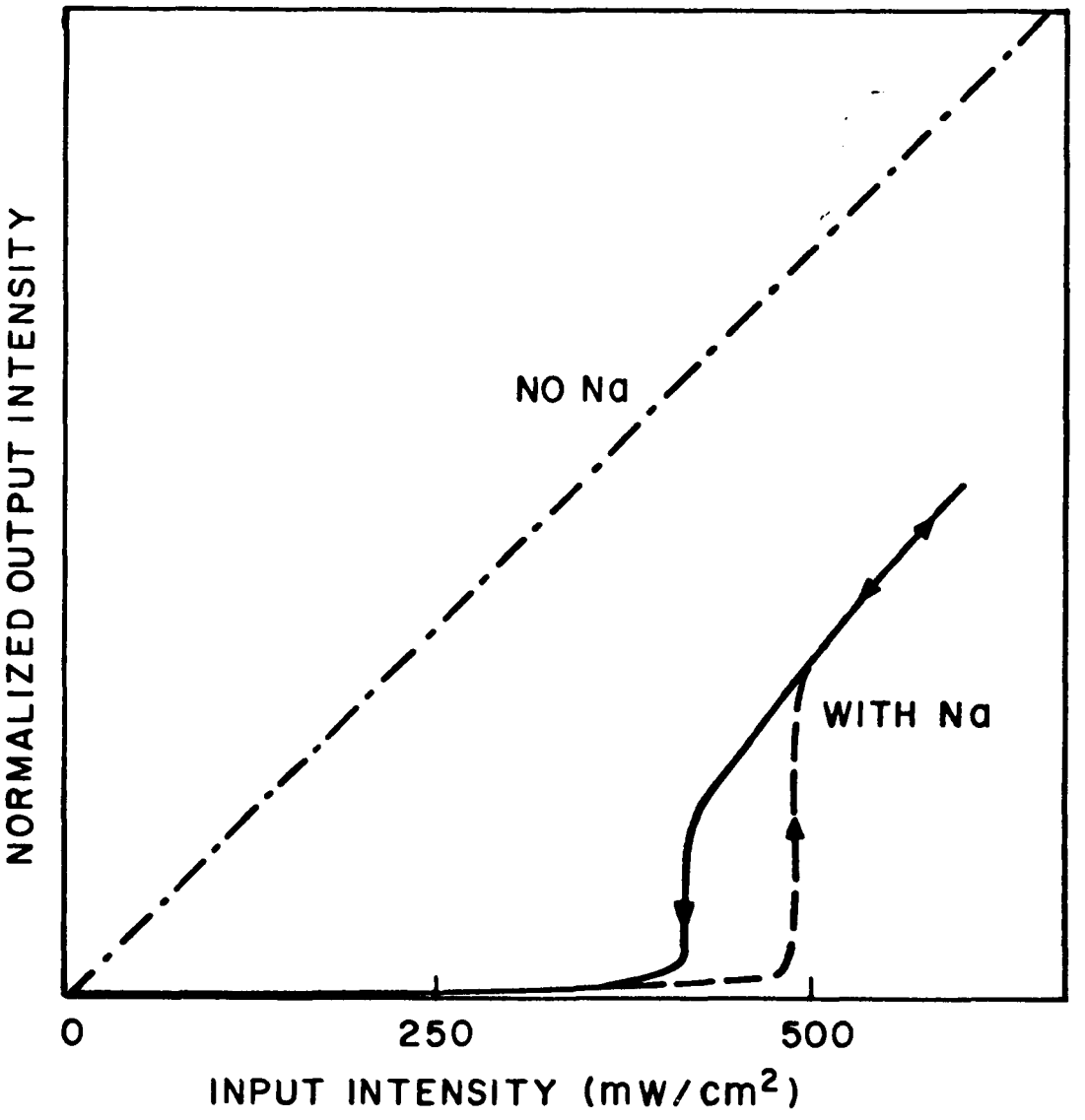

A TYPICAL BISTABLE CURVE

Figure 12

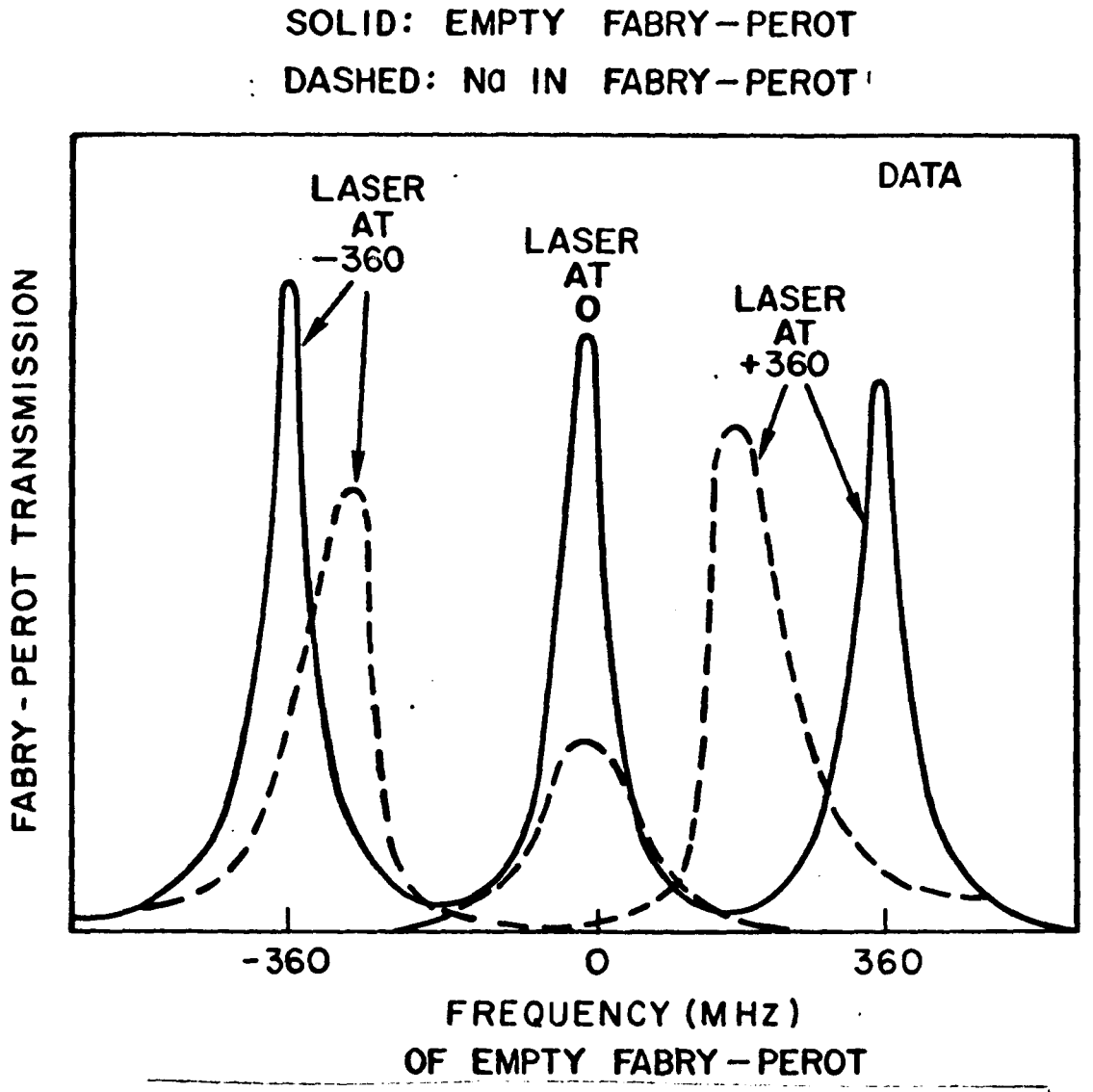

FABRY-PEROT ASYMMETRY

Figure 13

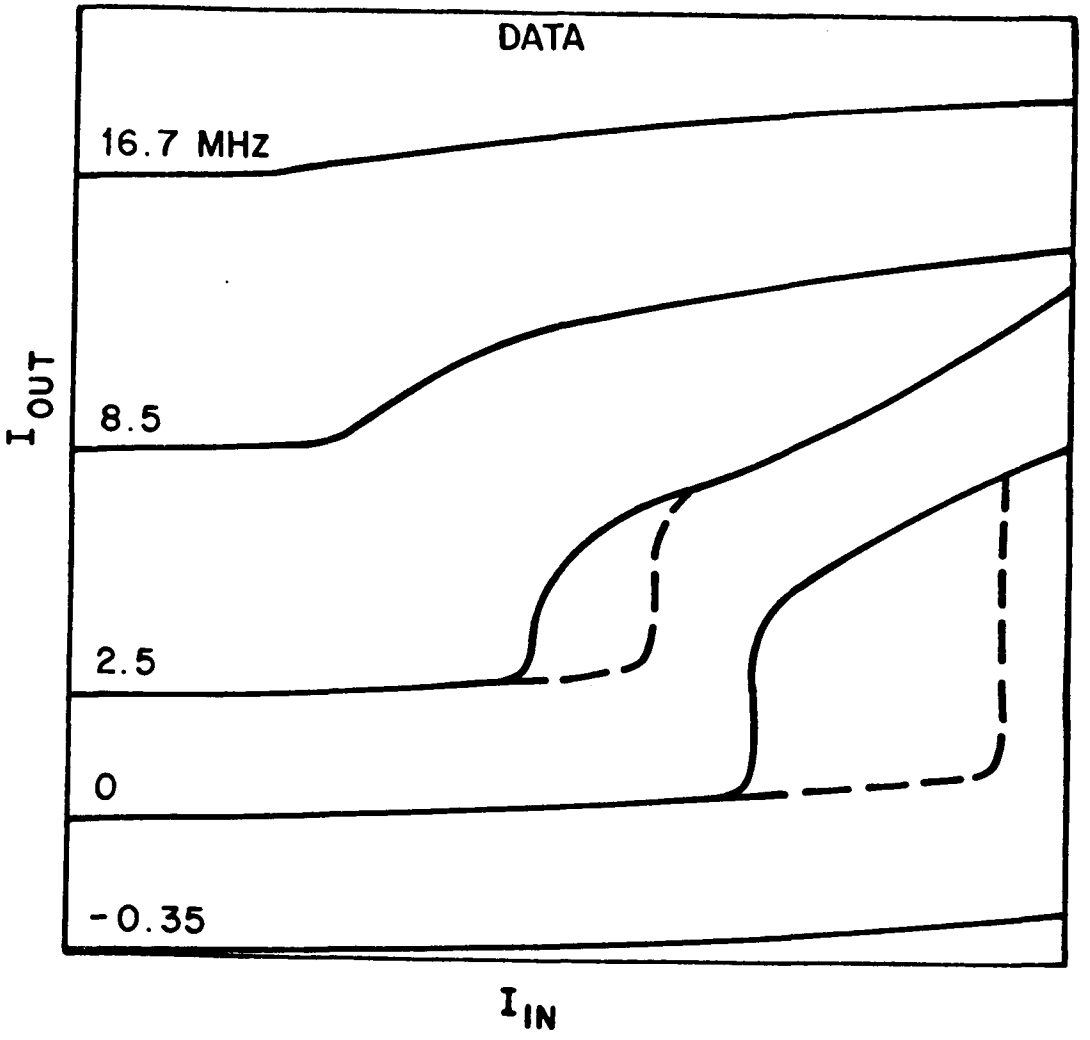

CHARACTERISTIC CURVES FOR DIFFERENT FP DETUNINGS

Figure 14

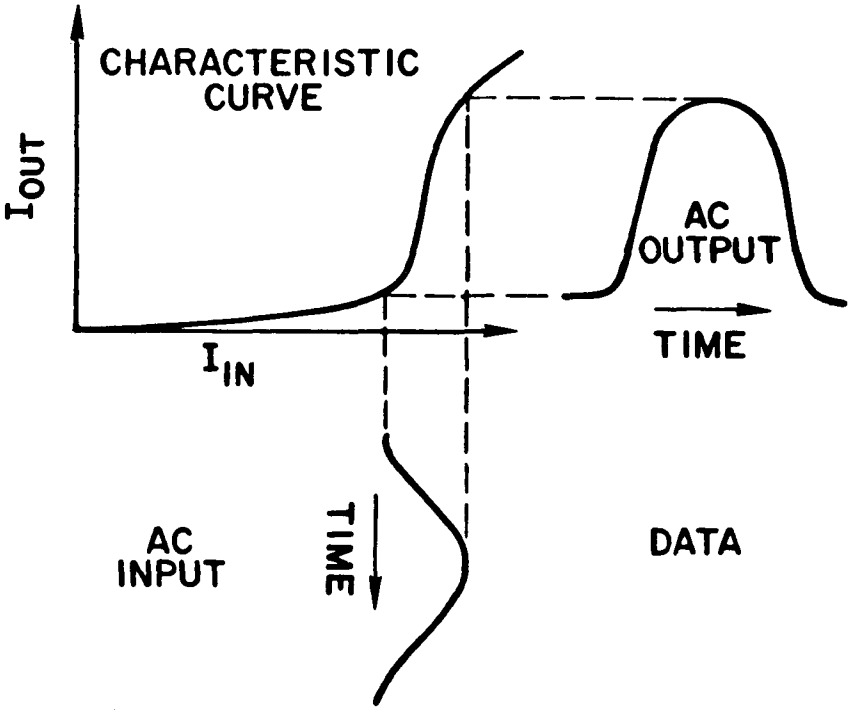

OPTICAL TRANSISTOR

Figure 15

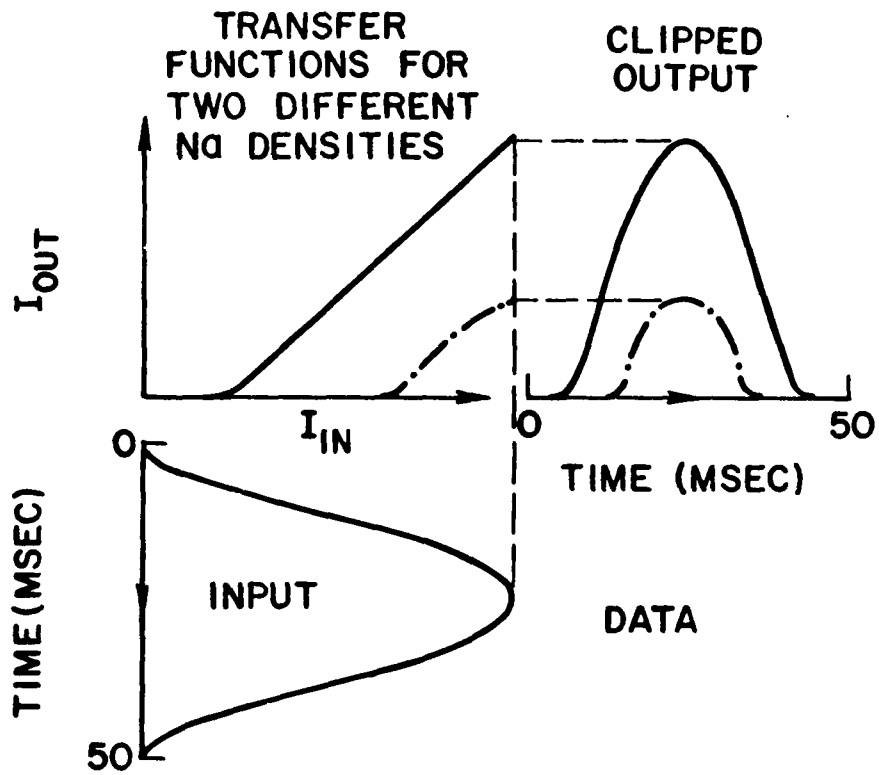

OPTICAL CLIPPER

Figure 16

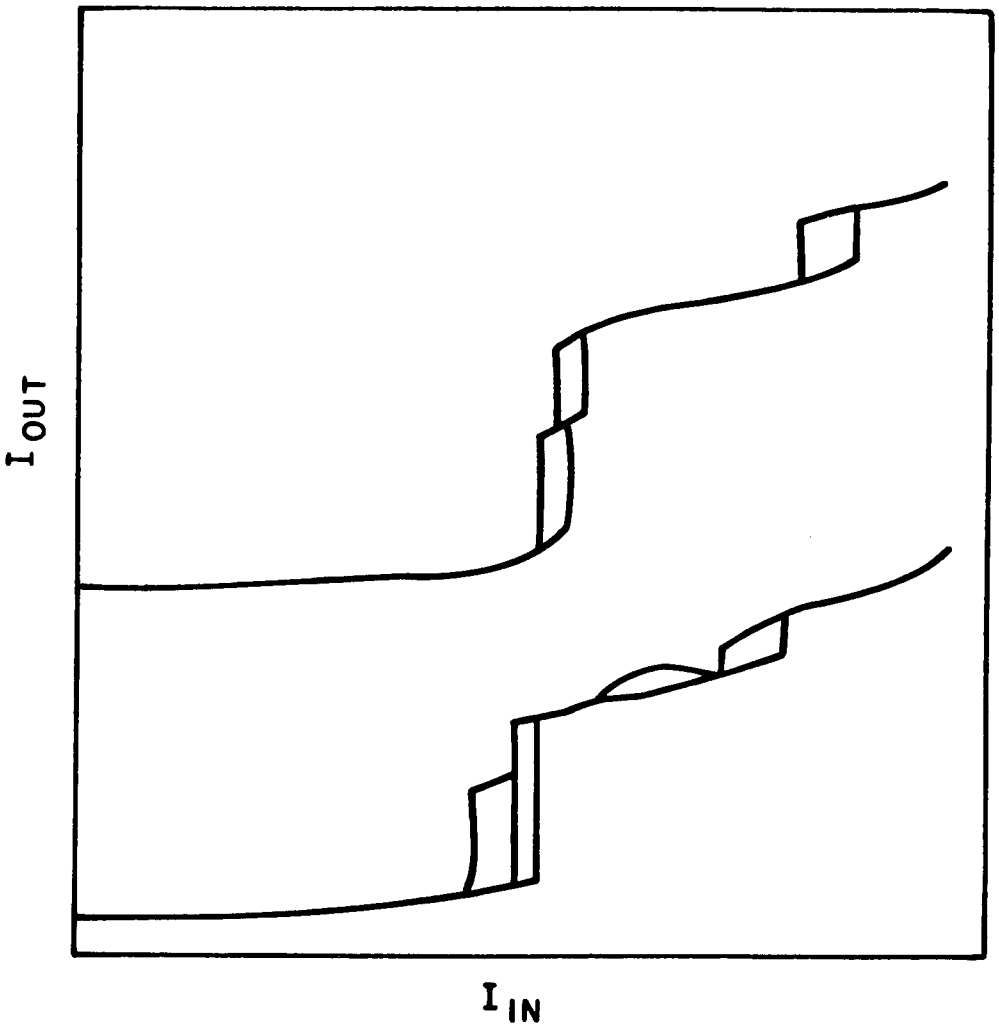

EFFECT OF FILAMENTATION

Figure 17

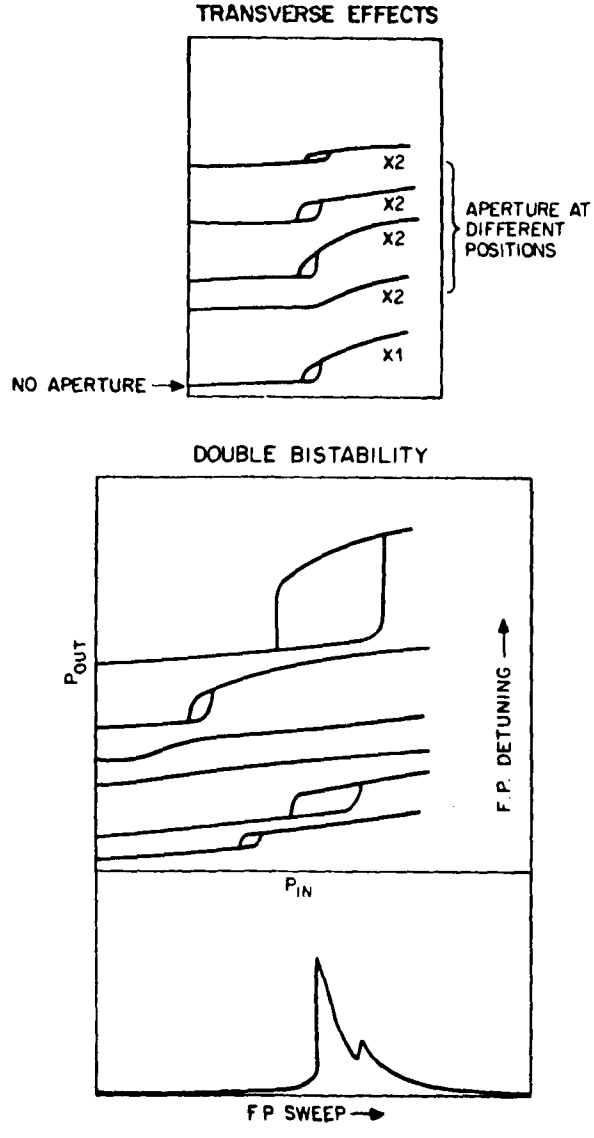

OTHER TRANSVERSE EFFECTS

Figure 18

EFFECT OF BUFFER GAS

(a) 400 mTORR ARGON; LASER FREQUENCY AT D_2; F=2 -500 MHz

(b) 500 mTORR ARGON; LASER FREQUENCY AT D_2; F=2 -400 MHz

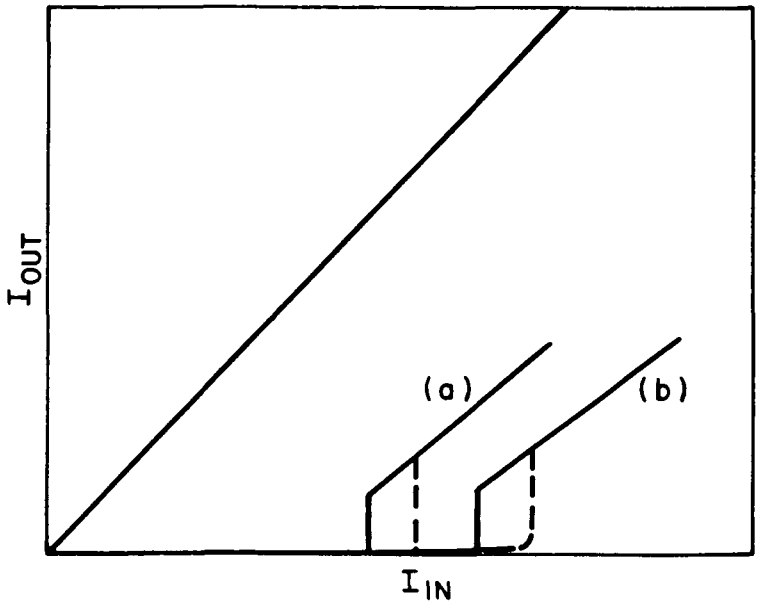

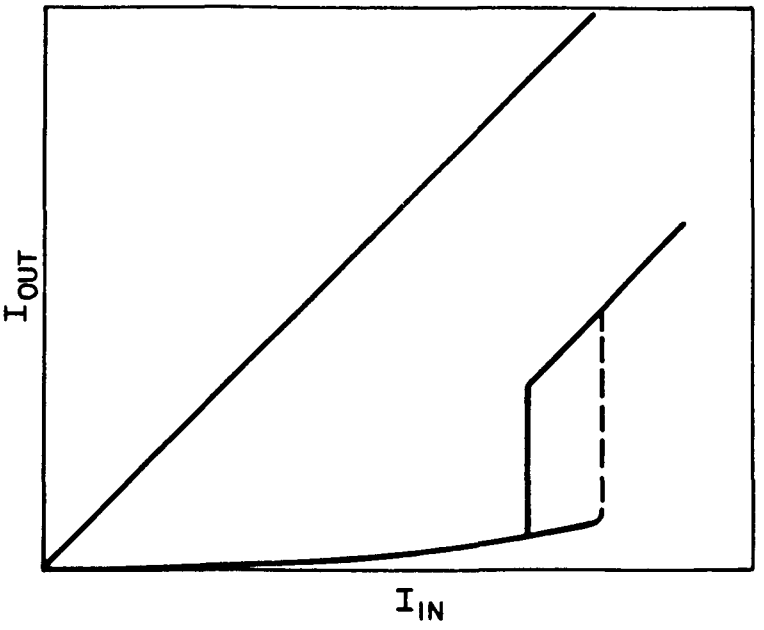

STRONG NONLINEAR DISPERSIVE BISTABILITY

LASER FREQUENCY AT CROSSOVER - 400MHz

PEAK INPUT POWER = 44mW

Figure 19

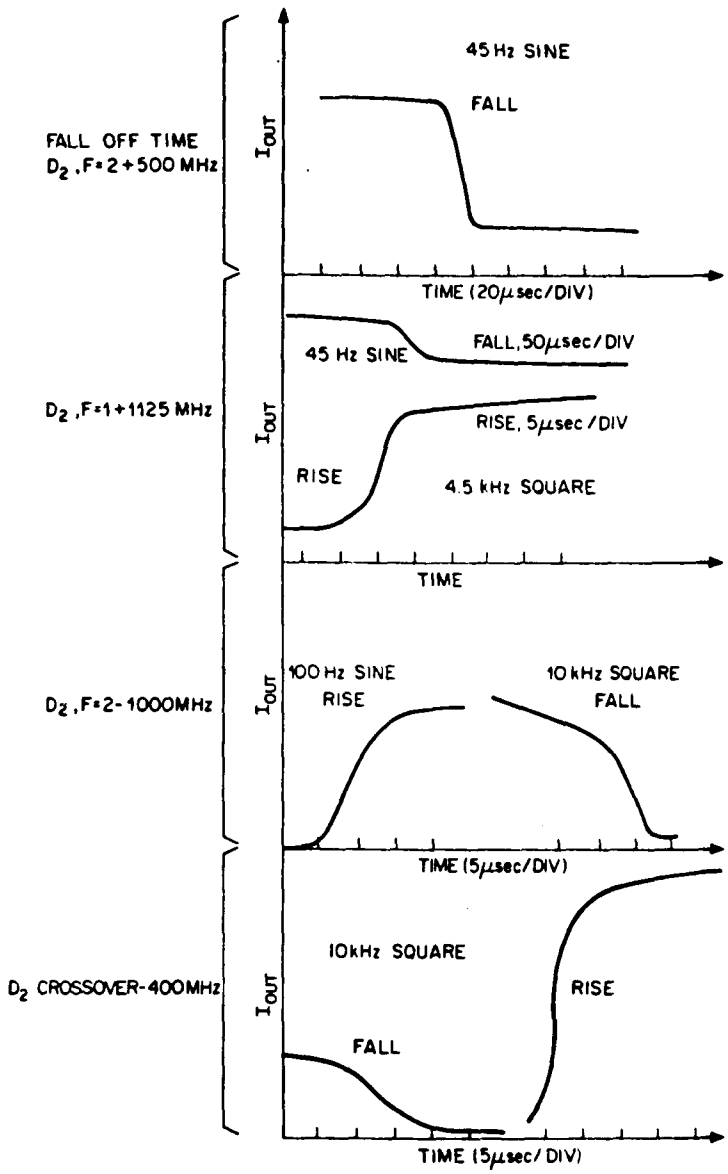

SWITCHING TIMES

Figure 20

CHAPTER 5

THE RUBY DEVICE

5.1 RUBY

The sodium experiment verified and extended the physical principles of an optical element with bistable and ac gain characteristics. For practical applications, a miniature, room temperature, fast, solid state device would be desirable. The next objective was to find a solid state system and several materials were considered (e.g., GaAs). Eventually it was decided to do the experiment using ruby as the nonlinear medium. The advantages were that optical interactions of ruby were well understood and good quality crystals were easily available, and the threshold intensity for observing nonlinearity in the R lines of ruby was reasonable. However the long radiative lifetime of the R lines of ruby (3-5 msec), suggested that the response of the device would be limited to a few milliseconds. Further, because of the temperature-enhanced phonon broadening of the R lines, significant nonlinearity was expected only around 77°K. The device was expected to be a slow, low temperature one. Yet ruby was a good testing ground to see the effects in a solid and also to check if the same principles applied there. Known properties indicated that to use the R lines of ruby, input of a few milliwatts was required. The origin of the nonlinear absorption and dispersion in ruby and their dependence on temperature requires some understanding of the optical spectra of Cr^{3+} ions in

corundum (Al_2O_3). So, this section will be a brief review of this subject.

The Cr^{3+} ion spectrum in Al_2O_3 has been extensively studied by many, in particular McClure[24] and Tanabe and Sugano.[25,26] The resonant R lines have been carefully studied experimentally by Nelson and Sturge.[27,28] The Cr^{3+} impurities enter substitutionally for Al^{3+} in the Al_2O_3 lattice. The electronic transitions of the d electrons of the chronium ion are strongly subjected to the crystal fields. Even though d-d electronic transitions of the Cr^{3+} ions are parity forbidden, the effect of the trigonal part of the crystalline filed is to mix in odd parity states (about 10^{-3} admixture) and hence the d-d transitions are split (R_1 and R_2 lines) and partially allowed having long electric dipole radiative life-times. The fully allowed transitions (pump bands) become broad absorption bands. The optical transitions are well understood and some important features of the electronic energy level diagram of Cr^{3+} in Al_2O_3 (Fig. 21) will be considered.

The $^4A_2$ and ^2E levels are split into the Kramer's doublets by spin-orbit interaction. At liquid helium temperatures the R_1 lines are zero phonon lines and their width is due to inhomogeneous crystal strains. Further, atoms excited to the E state stay there for the radiative lifetime. Due to phonons, rapid (nsecs) thermal equilibration of the excited state population occurs between the $\bar{2A}$ and $\bar{E}$ levels (splitting equivalent to

42°K). Above 10°K, the fractio- of excited atoms in the $\bar{E}$ state is given by the Boltzman distribution. The cw ruby laser used in this experiment (described in the next section) emitted 6934 Å radiation, nearly resonant with the narrow R_1 line[28] at 77°K, about 0.2 Å wide. It was anticipated in this experiment that a shift of the round trip phase due to the resonant R_1 dispersion would be non-linear because the R_1 line was strongly driven. The room temperature R_1 and R_2 lines are about 5 Å wide[28] and are centered at 6943 Å and 6929 Å. Consequently, the laser frequency, which lies between the lines, is weakly absorbed. Fast relaxation effects equalize the excited state populations. Under these circumstances, the line strengths[27] (E1C) are such that the R_1 and R_2 contributions to the non-linear refractive index almost cancel. Therefore, bistable operation was expected only when the device was near 77°K.

5.2 A CW RUBY LASER PUMPED BY 5145 Å ARGON LASER

INTRODUCTION

A laser tunable over the absorption width of the LN_2 R_1 line (0.5 cm^{-1} total width) of ruby was required for studies of the ruby optical memory and amplifier. Monochromatic cw single mode power of several mW was required. Dye laser efficiencies in that region are only about 10% of Rhodamine-6G dye lasers operating near 600 nm. For this and stability reasons we decided to use a ruby laser.[28b]

Argon laser pumped cw ruby lasers have been described by Birnbaum et al.,[29] Szabo,[30] Liao et al.,[31] and Koo et al.[32] The gain of the R_1 transition at LN_2 temperatures is so high that lasing efficiencies of more than 15% should be easy to achieve, although such efficiency has only been reported by Liao et al.[31]

DESCRIPTION

In contrast to earlier designs the output was antiparallel to the pump beam. With vacuum above one face of the ruby, unpleasant optical effects of LN_2 on the pump beam were avoided. The 1/4" diameter, 1 cm long, 0.05% Cr^{3+}, 60° Union Carbide ruby rod had end faces flat to $\lambda/10$. The faces formed a wedge of angle 12±2 secs of arc. The LN_2 face was coated 99+% reflectivity for both 5145 Å and 6934 Å. The vacuum face had 50% reflectivity for 6934 Å and was 3% for 5145 Å. The rod was held in a 0.255" hole in a Varian Conflat® flange and was epoxied in place using stycast 1266 epoxy. The epoxy joint underwent over one hundred room temperature to LN_2 temperature cycles before a small leak developed, which was easily sealed. The flange was mounted on a 1-1/2" i.d. evacuated stainless steel tube with a window at Brewster's angle at the other end, (Fig. 22). Use of VacIon vacuum pump (Varian 911-5011), providing 10^{-4} Torr at the ruby face, avoided oil condensation on the cold ruby face in the vacuum region.

Ocasionally an LN_2-trapped diffusion pump using Santovac^R 5 vacuum pump fluid was used to degas the heated ion pump.

LN_2 FILL

The average frequency of the output depended on the LN_2 temperature which was controlled by pumping on or pressurizing the LN_2 dewar. The Union Carbide DC-5 LN_2 dewar was well suited for this purpose. Since the ruby rod was located close to the top of the dewar the LN_2 level dropped quickly. However, it was undesirable to refill often pumped or pressurized LN_2, because that would reduce greatly the fractional operating time. To postpone the filling time we used a Helium "balloon", a hollow cylinder with an open bottom which was pressurized with gaseous Helium, thereby controlling the LN_2 level in the dewar. When the dewar contained too little LN_2, pressurizing with Helium would not raise the LN_2 level to satisfy a level sensor, and a delay circuit initiated LN_2 filling. We could have instead used an external dewar constantly pumped or pressurized. Under 10 inches Hg pressure (absolute), LN_2 refilling was required only every 2 or 3 hours. The total of filling and repumping consumed about 20 minutes.

LASING CHARACTERISTICS

The argon laser (Coherent Radiation CR53) beam at 5145 Å provided a power of 2W at the ruby rod. The beam was focused by a 15 cm focal length lens into the laser rod

(Fig. 23). All optics were antireflection coated or at Brewster's angle. The 300 mW output was a linearly polarized single transverse mode without spikes apart from mode beating. A collimating lens provided a 2.5 mm diameter beam. The output contained a number of longitudinal modes separated by approximately 8.6 GHz, the free spectral range (c/2nL) of the 1 cm long cavity. The modes spanned a frequency range of more than 60 GHz about the LN_2-R_1 line. This is considerably greater than the normal 15 GHz total width of the R_1 doublet, and is attributed to strains, local heating, and isotopes.[33] Mode pulling effects were also seen. Although the laser output had a number of longitudinal modes, a single mode could be made to dominate (Fig. 24) by bringing different parts of the wedged laser rod under the pump beam. For this reason the laser assembly was on an x-y translator. By pumping or pressurizing the dewar, the frequency of the dominant mode could be tuned over a 20 GHz range.

FABRY PEROT FILTERING

A single output frequency was obtained using an external Fabry-Perot (Burleigh RC-10) interferometer (FP) to filter the ruby laser output. The FP had 95% reflective coated, $\lambda/100$ flat mirrors separated by 2 mm (free spectral range of 75 GHz). The FP spacing was controlled by piezoelectric transducers on one of the mirrors. Using a small 400 Hz modulation on the average DC bias of the transducers,

the output of the FP was maintained at a local maximum of transmitted intensity, corresponding to being resonant with a given mode, by a standard servo technique (Fig. 23). The stabilization corrected for slow, drifts of the FP mainly due to slow temperature fluctuations. The loop correction time was set at about 0.1 sec. By quickly changing the transducer bias we could lock onto a different mode. There was a 25% transmission loss in the FP due to absorption in the coatings and surface irregularities of the mirrors. The ruby laser delivered more than 300 mW power distributed among 7 or 8 different modes. By moving the laser assembly, more than 75 mW was obtained in various filtered single modes. By sweeping the FP through a free spectral range and passing the light through a ruby absorber we could see the relative absorption of the different modes directly (Fig. 25).

FREQUENCY CALIBRATION

The absolute frequency was measured with a high resolution grating spectrometer. The mode frequencies relative to one another were measured with respect to a He-Ne laser line with a FP. The He-Ne line was also used to make sure that we were always using the same order of the FP. Before each measurement the DC bias on the FP transducers was adjusted to put the He-Ne line on the negative vertex of the triangular voltage used for scanning the FP (Fig. 25).

Using data obtained as illustrated in Fig. 25 the absorption spectrum of a 0.9 mm long, 0.05% concentration, 0° ruby was measured and is presented in Fig. 26.

AMPLITUDE STABILIZATION AND MODULATION OF THE BEAM

To correct for amplitude fluctuations and to directly plot out the output intensity as a function of the input intensity an acousto-optic modulator (Zenith - Model M-40R) was used. The modulator had a quartz block in which, 40 MHz sound waves were produced by an external RF voltage applied to several PZT hammers on one side of the block. The modulator is aligned so that the light beam is at normal incidence to the sound waves. The modulator was mounted on an X-Y-Z translator with fine controls to rotate the modulator about the Y axis. The modulator was aligned so that the light beam was at normal incidence to the sound waves. The output consisted of a row of spots lying in the plane containing the incident light beam and the sound waves. The several spots correspond to the several orders of light Bragg scattered by the ultrasound waves. By fine tuning the tilt of the modulator a maximum of 67% of the incident light was coupled into the first order scattered beam. The amount of light scattered into the first order depends on the amplitude of the sound wave. Varying this amplitude in accordance with the applied modulation on the RF voltage produced a corresponding

amplitude modulation of the light in the scattered beam. The nonscattered beam was modulated inversely. Using an aperture, the scattered beam was isolated.

A feedback circuit (Fig. 27) receiving a signal from the sampling photomultiplier generated an error with respect to a DC voltage level set by the potentiometer. The output was held constant at any value from zero to the maximum modulator light output by varying the potentiometer setting. The amplitude noise was less than a few percent. A 2Hz triangular modulation was superposed on the optical beam to directly plot the characteristic curve.

MEASUREMENT OF NONLINEARITY

A 1 cm long 0.045% concentration and 60° oriented crystal was mounted inside the dewar (Fig. 28). The c axis of the ruby was determined roughly and the axis was set approximately perpendicular to the polarization of the light. The modulator was turned on with 10 cps, triangular input. The outputs of the I_{in} photomultiplier (RCA 7102) and the I_{out} photomultiplier were fed to the horizontal and vertical amplifiers of the Tektronix 564 scope. The top of Fig. 29 shows traces of the curves obtained by scanning the locking FP. The FP was then locked onto the least absorptive mode and the gain of the 564 scope was adjusted to produce a 45° line on the scope. Then the FP was locked onto the most absorptive mode, and the slope of the line was measured. This gave the linear absorption length αL. An αL of 6.6 was measured on the particular trace on Fig.29 . Then

introducing a 7.5 cm lens the beam was focused onto the crystal. A dramatic increase in the transmission was seen upon saturating the absorption line (Figures 30 and 31). This experiment established that there was sufficient nonlinearity and laser intensity to construct a device using ruby as the intracavity nonlinear medium. The next step was to design an appropriate cavity.

5.2 DESIGN OF THE DEVICE CAVITY

There was an important criterion in the design of the device cavity. To obtain the maximum nonlinearity in the ruby, it was essential to focus the beam. So the cavity had to be mode matched for an incoming spherical beam. Further the cavity had to be tunable. Initial experiments were performed with plane FP cavities, made up of nearlyparallel faced ruby with a wedge angle of 12±2 secs of arc (for tuning purposes). But the peak transmissions of the cavities without much intracavity absorption were as low as 10% on account of the wedge and poor mode match with the incoming spherical beam. So a plano concave FP cavity for the device, with minimum diffractive losses was designed. For the design, the propagation of Gaussian beams through media of different indices had to be understood. So a formalism to handle Gaussian beam propagation was developed and then applied to the plano concave geometry. The reader may look up Ref. 34 for further details.

Green's Function Approach: Consider the incoming field to be of the form

$$E(r,z,t) = \varepsilon(r,z)e^{i(kz-\omega t)} + c.c., \qquad 5.1$$

where $\varepsilon(r,z)$ is a slowly varying envelope (only in spatial coordinates). Let us not consider the $e^{i\omega t}$ term for the moment. Then $E(r,z) = \varepsilon(r,z)e^{ikz} + c.c.$; an azimuthally symmetric wave propagating in the z direction. On substituting into the wave equation $(\nabla^2+k^2)E = 0$ and using SVEA we get

$$\left(\nabla_t^2 + 2ik\partial_z\right)\varepsilon(r,z) = 0, \qquad 5.2$$

where

$$\nabla^2 = \nabla_t^2 + \partial_z^2 \ . \qquad 5.3$$

Eq. 5.2 is mathematically identical with the 2D Schrödinger's Equation. To solve this equation expand ε in terms of its Fourier components. Then,

$$\varepsilon(x,y,z) = \int e^{i(px+qy+sz)}\,\tilde{\varepsilon}(p,q,s)dpdqds, \qquad 5.4$$

substituting in Eq. 5.2 we get

$$\int(-2ks-q^2-p^2)\tilde{\varepsilon}(p,q,s)e^{i(px+qy+sz)}dpdqds = 0, \qquad 5.5$$

clearly $\tilde{\varepsilon}(p,q,s) = \tilde{\varepsilon}(p,q)\delta(s + \frac{p^2+q^2}{2k})$ is a solution. The solution may be generally written as

$$\varepsilon(x,y,z) = \int e^{i(px+qy) - i\left(\frac{p^2+q^2}{2k}\right)z} \tilde{\varepsilon}(p,q)\,dpdq \,, \qquad 5.6$$

where $\tilde{\varepsilon}(p,q)$ is any function of p and q.

Assume at $z = 0, \varepsilon = \delta(x)\delta(y)$, i.e., a point source like an aperture. Then $\tilde{\varepsilon}(p,q) = \frac{1}{(2\pi)^2}$. Then Eq. 5.6 may be evaluated, so that

$$\varepsilon(x,y,z) = -\frac{ik}{2\pi z} e^{ik(x^2+y^2)/2z} \,. \qquad 5.7$$

Hence one could write down a Green's function,

$$G(x,x_0,y,y_0,z,z_0) = \frac{-ik}{2\pi(z-z_0)} e^{-ik\left[\frac{(x-x_0)^2+(y-y_0)^2}{2(z-z_0)}\right]} \,. \qquad 5.8$$

Hence the field at a point (x,y,z), is related to the field at a point (x_0,y_0,z_0) by

$$\varepsilon(x,y,z) = \int dx_0 dy_0 dz_0 G(x,x_0,y,y_0,z,z_0)\varepsilon(x_0,y_0,z_0). \qquad 5.9$$

This relationship holds even if x_0, y_0, and z_0 are complex. In particular, a form of the electric field suitable for describing Gaussian wave propagation is obtained by setting $x_0 = y_0 = 0$ and $z_0 = -ia$ with $a \geq 0$. Then

$$\varepsilon(r,z) = -\frac{ik}{2\pi(z+ia)}\, e^{-\frac{ikr^2}{2(z+ia)}}, \qquad 5.10$$

and the intensity

$$I(r,z) = |\varepsilon(r,z)|^2 = \frac{k^2}{4\pi^2(z^2+a^2)}\, e^{-\frac{kr^2}{(z^2+a^2)}} . \qquad 5.11$$

Hence the radius of the beam defined to be the 1/e point of the intensity, varies with z as,

$$r^2 = \frac{a}{k}\left(1 + \frac{z^2}{a^2}\right) \quad \text{or}$$

$$r^2 = r_0^2\left(1 + \frac{z^2}{k_0^2\, r_0^4}\right), \qquad 5.12$$

where r_0 is the beam radius at $z = z_0$.

We can also find a definite relationship for the radius of the phase front (surface of constant phase) R, with respect to the beam parameters a and k. Thus

$$\phi(r,z) = -\tan^{-1}(a/z) + kz - \frac{kr^2 z}{2(z^2+a^2)} = \text{constant}, \qquad 5.13$$

defines a phase front, and $\phi = \mathrm{Im}(\ln\varepsilon)$. Eq. 5.13 implies that

$$\left(\frac{\partial\phi}{\partial z}\right)_{z,\,r=0} \Delta z = -\left(\frac{\partial\phi}{\partial r^2}\right) r^2 , \qquad 5.14$$

where Δz and r are small. Then

$$R(z) = \frac{1}{2}\left(\frac{r^2}{\Delta z}\right) \quad \text{which reduces to}$$

$$R(z) = -\frac{1}{2}\frac{(\partial\varphi/\partial z)_{z,r=0}}{(\partial\varphi/\partial r^2)_{z,r=0}} \quad , \quad \text{and} \qquad 5.15$$

substituting for φ from 5.13 we get

$$R(z) = \left(\frac{z^2 + a^2 + a/k}{z}\right) . \qquad 5.16$$

Now that we have the formulae for R(z) and r we can discuss the details of the device cavity.

DETAILS OF THE DESIGN

The eventual design of the cavity was based on the ease and economy of construction and also to have the option of changing the thickness of the ruby crystal retaining the same spherical mirror. The cavity is in three pieces, a plane parallel faced ruby, a quartz spacer and a concave quartz mirror (Fig. 32). One end of the ruby is 90% reflective coated and the end inside the cavity is multi-layer antireflection coated. For perfect mode matching condition, the design is for a beam radius r_0 on the reflective face of the ruby and a phase front of radius R = radius of curvature of the mirror at z = T.

The electric field in region I is (Fig. 32),

$$\varepsilon_I = \frac{i\delta}{z + iA} \exp\left[+ 1 \left\{- \frac{Kr^2}{2(z+iA)} + Kz\right\}\right]$$

$$+ \frac{i\delta\rho}{(z'+iA)} \exp\left[i \left\{ \frac{- Kr^2}{2(z'+iA)} + Kz\right\}\right], \qquad 5.17$$

where ρ is the reflection amplitude at the boundary at z=L.The field in region II is

$$\varepsilon_{II} = \frac{i\beta}{z + iA} \exp\left[i \left\{- \frac{kr^2}{2(z+ia)} + (KL + k(z-L))\right\}\right], \qquad 5.18$$

where $a = kr_0^2$, $A = Kr_0^2$ and δ and β are constants to be determined from the boundary and normalization condition. Since the boundary conditions are,

$$\varepsilon_I\Big|_{r=0,z=L} = \varepsilon_{II}\Big|_{r=0,z=L}, \qquad 5.19$$

$$\frac{\partial\varepsilon_I}{\partial r^2}\Big|_{r=0,z=L} = \frac{\partial\varepsilon_{II}}{\partial r^2}\Big|_{r=0,z=L}, \qquad 5.20$$

we get,

$$\frac{(1+\rho)\delta}{L + iA} = \frac{\beta}{L + ia} \quad \text{and} \qquad 5.21$$

$$\frac{k}{L + ia} = \frac{K}{L + iA}. \qquad 5.22$$

From 5.22 it is clear that the spot size is independent of the medium.

Hence from 5.21 and 5.22

$$\varepsilon_{II} = \frac{i\beta}{(z+L(n/N-1) + in/N\ A)} \exp\left[-\frac{ikr^2}{2(z+L(n/N-1) + in/N\ A)}\right].$$

5.23

The radius of the phase front in region II is,

$$R(z) = \frac{\{z+L(n/N-1)\}^2 + \frac{n^2A^2}{N^2} + \frac{An}{kN}}{z + L(n/N-1)} \quad . \qquad 5.24$$

Experimentally, we found nonlinear absorption at intensities of a few hundred W/cm^2 for an $\alpha L = 1$. With single mode powers of 20 mW or more and a beam radius $r_0 = 20\ \mu$ on the face of the ruby one could have an intensity of 1.5 KW/cm^2 and with 90% mirror reflectivity one could easily get intracavity intensities of 150 W/cm^2 or more.

By trial and error a mirror radius of 0.87 cm was chosen. For $r_0 = 20\ \mu$, A = 0.6478 cm and hence for the phase front to have a radius of curvature equal to that of the mirror at z = T, one must have,

$$T + L(n/N-1) = 4.423 \text{ mm} \quad . \qquad 5.25$$

To satisfy Eq. 5.25 for different ruby thicknesses, retaining the same spherical mirror one should have different spacers between the ruby and the mirrors. The spacer thickness S for the different sample lengths was given by

$$S = T-L = 4.423 - Ln/N - 0.233 \text{ mm},$$

where the 0.233 mm difference arises from the geometry of the curved mirror with a coated diameter of 4 mm. For ruby thicknesses of 5, 3 and 1 mm, the spacer thicknesses were 0.767, 2.136 and 3.505 mm respectively.

MODE MATCHING THE DEVICE CAVITY

Perfect mode matching of the cavity implied 100% of the output in the TEMoo mode of the cavity. There were four parameters to be matched: the spot size, (1 degree of freedom), location of the beam waist on the face of the ruby (1 degree of freedom), perpendicularity of the beam to the ruby face (2 Degrees of freedom) and the beam must feedback from the concave mirror onto the incident beam (2 degrees of freedom). Experimentally all these parameters could be satisfied by using 2 lenses. A combination of a 15 cm and 10 cm antireflection coated lenses was used. In the later data the 15 cm lens was replaced by a 10 cm lens. The laser beam diameter was calculated and the lenses were placed at the appropriate distance from the device cavity to produce a 40 μm spot on the ruby. Since both lenses had X-Y-Z translation giving 6 degrees of freedom and the sample mount had 2 degrees of freedom, a rotation about the vertical axis plus an up and down tilt, we had in all, sufficient degrees of freedom to satisfy the above 6 conditions. The lenses were moved in a particular order to collapse all the

transmitted laser spots of the cavity into a single one. But, by doing so, one obtained one or a combination of the cavity modes. By scanning the cavity spacing, the TEMoo mode intensity was peaked by moving the foci of the lenses. Figure 33 gives typical He-Ne laser outputs of the cavity-run on a strip-chart, while the cavity spacing was tuned by changing the LN_2 temperature by pumping on the liquid. A number of effects (e.g., the nonspherical intracavity surface of the ruby) allowed only 40% (6328 Å) maximum transmission. The low intensity room temperature finesse was about 18. Mirror reflectivities R = 0.91, and transmissivities T = 0.09. In contrast to the properly mode matched cavity data shown in Fig. 33, figures 34 and 35 show outputs of an improperly mode matched FP cavity and a cavity in which the ruby has been replaced by a flat quartz mirror.

HOUSING OF THE CAVITY: DEWAR AND SAMPLE HOLDER

To vary the temperature of the device a Janis Supervaritemp dewar was used in conjunction with a temperature controller (Lake Shore Cryotronix Inc.). The temperature servo guaranteed a thermal stability of the sample holder of better than a tenth of a degree. The dewar had a central cylindrical chamber of 1.45" diameter into which the device could be inserted. At the bottom of the dewar were optical ports through which the laser beam could be made to pass through the device. To vary the cavity spacing of the device we used pressure tuning with helium gas. A glass jacket with antireflection coated windows

was designed to fit into the sample chamber of the dewar. Then the device consisting of a ruby mirror, a quartz washer and a quartz mirror fitted inside the 1/4" bore of a spring loaded brass cylinder, was held at the end of a 1/4" stainless steel rod which was supported by the sides of the glass jacket by Teflon washers (Fig. 36). The brass cylinder at the the bottom had up and down tilt, controllable from outside the dewar. With the stainless steel tube held at the top by a quick coupler it was easy to align the device quite perpendicular to the incident laser beam. These degrees of freedom are in principle not essential as in the process of mode-matching the freedom of using two lenses would suffice. However, this enabled the use of the center portion of the lenses to avoid astigmatism. With liquid helium in the dewar the temperature of the sample could be varied from 4°K to room temperature by a heater coil wound around the brass cylinder housing the device samples. The temperature was detected by a calibrated GaAs diode, whose output went to the temperature controller supplying the current to the heater coil (Fig. 36).

The top of the glass jacket had arrangements for letting in helium and also a pumping port for lowering the pressure inside. A pressure regulator was attached in series with the mechanical vacuum pump. With a controlled helium flow this formed a pressure servo system to maintain the pressure inside constant. At liquid nitrogen temperatures a scan over a free spectral range was possible by

changing the helium pressure by a few inches of mercury. The longer 5 mm ruby samples with thin washers were more stable under pressure tuning than the short 1 mm sample with the thickest washer, which is ascribed to the lesser effect of fractional optical path length changes due to pressure fluctuations. The optical transmission of the dewar was only 70% due to window reflections.

FARADAY ISOLATOR

When the device cavity was properly mode matched with the laser beam, the reflected beam from the cavity fed back into the laser and created frequency and amplitude noise in the laser output. To prevent this feedback a Faraday isolator was used. This consisted of two dysprosium glass rods of 6 cm length joined together lengthwise with index matching lens cement. The rods were inserted into the axial bore of a Bendix water cooled solenoid which put out 1669 Gauss per ampere current. With the Verdet constant at 6934Å, in order to rotate the polarization of the light by 45°, a 2.6 kG magnetic field was needed. At the entrance of the solenoid a Nicol prism was placed with its transmission axis parallel to the incident light polarization. (The laser light was almost completely linearly polarized.) But during quite a bit of the data taking the inside bore of the solenoid heated up, the Verdet constant decreased and the return beam being no longer

rotated by 90°, fed back into the laser and produced instabilities. This problem was overcome by having the glass rods enclosed in a water cooled copper sleeve. At normal operation the Isolator worked at a current of 15.75A at 60 volts.

5.4 EXPERIMENTAL RESULTS AND COMPARISON WITH THEORY

In this section the experimental work will be summarized and will be compared with the known information about ruby and the analytical model for the device.

In most of the data the peak transmission of the device cavity for the TEMoo mode was around 33%. Since the sample was held at the end of a long holder, there was some noise pickup, which gradually spoiled the mode match. So the lenses had to be adjusted often to maintain proper mode match. But the stability of the laser, the feedback system and the short term stability of the sample itself were sufficient for taking reasonable data. Even though the initial data were taken on a storage scope, in the later stages of the experiment with improved stability the characteristic curves were directly photographed with the light intensity being scanned as slow as 0.2 cps. (The photographs of the earlier data on the storage scope, were not very clear on account of the poor contrast and non-uniform diffusion of the phosphorescent material on the scope screen.)

The 5 mm, 0.05% Cr^{3+}, 0° ruby was the first sample tried. It became harder to mode match the device at lower temperatures on account of increased absorption in the sample. Even though better mode matching was possible at higher temperatures, in the process of cooling the sample, due to the instabilities in the dewar, sample holder etc., the mode matching deteriorated. The peak transmitted intensities were of the order of a few hundred watts/cm^2. After futile efforts at trying to mode match the cavity at 77°K, the experiment was tried at 120°K. Surprisingly, the device exhibited good bistability and ac gain (Fig. 37). On warming the sample, dramatic bistable curves were seen at all temperatures (Fig. 38). The room temperature result in Fig. 39 clearly shows a limiter, ac gain, discriminating pulse amplifier and a bistable characteristic, for various cavity detunings. This result was very much in conflict with our picture of the nonlinearity in ruby, as the phonon broadened R lines of ruby contribute very little nonlinear refractive index or absorption and also the refractive index contribution of the R_1 and R_2 line nearly cancel each other at room temperature. To pinpoint the origin of the nonlinear refractive index (since the cavity output as a function of detuning was asymmetric), further data were needed. The response of the device to square input pulses was studied next.

The switching times depended on the nature of the characteristic curve (slow for bistability and faster for

the transistor mode) varying from a few msec to 20 msec (Figs. 40, 41, 42 and 43). Further, the switching times were independent of the temperature. We were able to elminate the dominance of thermally induced refractive index for the following reasons. From Refs. 35, 36 and 37 we see that the switching times for thermal effects would be of the order of $\frac{c_v \rho r_0^2}{(2.41)^2 K}$, where c_v is the specific heat, ρ the density, r_0 the beam radius and K the thermal conductivity. At 300°K this time is of the order of 8 μsec and at 100°K it is as fast as 70 nsec for a beam radius of 20 μ. The lack of any temperature dependence of the switching times was an evidence against any thermal effect. Further, the amount of phase shift needed for the device operation, with thermally induced refractive index and length changes, required much higher levels of laser power.

With the elimination of thermal refractive index as the main cause, the similarity of the device response time to the radiative lifetime of the $\bar{E}$ state strongly pointed to a radiative refractive index change. Closer inspection of the ruby spectrum revealed yet another source of nonlinearity. There is a substantial amount of excited state absorption owing to the long lifetime of $\bar{E}$ state and due to strong parity mixing transitions to highly phonon coupled bands.[38,39,40] Figure 44a is the excited state absorptions as measured by Fairbanks et al[40], and Fig. 44b is the measurement of Kushida[38]. These absorptions have weak

temperature dependence, and have a significant refractive index contribution. Further, the strong U and the Y pump bands and the huge absorption at the far off charge transfer bands (40,000 cm^{-1} away) have a large refractive index tail near the R lines. The values of the refractive index are different for an atom in the ground state and one in the excited $\bar{E}$ state as the latter is closer in frequency to these non-resonant bands. In a subsequent calculation of the phase shift due to these bands the shape and size of the absorption of these bands is assumed to be unchanged for the pumped and unpumped system, but the different detuning of the laser from the center of the bands for the ground and the excited state is taken into account. The maximum non-linear phase shift is given by $\frac{1}{2}(1+w)(\varphi^e-\varphi^g)$ where w is the difference in the fractional population of the upper and lower state (Ref. Chap. 3). The total dispersive contribution from all transitions with the atom in the ground state is φ^g and φ^e is that with the atom in the excited state. Tables 1 and 2 list the different dispersive phase shift contributions by a 1 cm long, 0.05% Cr^{3+} ruby. A point to be noted is that the dispersive contributions of all the states decay with the $\bar{E}$ lifetime of a few millisecs. Since the $\bar{E}$ radiative lifetime varies only by 20% in going down to LN_2 temperatures, we expect the ruby device to have switching speeds almost independent of temperature, as observed.

In the analytic model we put in the values of dispersion and absorption calculated for ruby (Table 1 and

2) with a sample thickness of 5 mm. The model predicted that the system would be hardly bistable at room temperature and would start to show bistability around 120°K (Figs. 45-48). But when the length of the sample was increased to 1 cm, (equivalent to doubling the nonlinearity) the theory (Figs. 49-52) showed a remarkable similarity to the experimental results (Figs. 37-39). The room temperature bistability was as good as experimentally seen, and the intensity thresholds for these effects were lower than that in the experiment. In the computer model, the Orbach relaxation of the Kramer's doublet was taken into account and the contribution from the R_2 transition was also included. Not included were the standing wave effects inside the cavity.

The next sample tried was the 5 mm, 60°, 0.03% Cr^{3+} ruby. This hardly showed any bistability at room temperature, and if we compare with the predictions of the theory for a 5 mm sample of 0.05% Cr^{3+}, this is not surprising. But at lower temperatures, i.e., around 120°K and below, the sample did go bistable and the results are shown in Figs. 53 and 54.

A 0.03% Cr^{3+}, 60°, 3 mm and a 0.05% Cr^{3+}, 0°, 0.9 mm samples were tried next and the results are shown in Figs. 55-58.

Since the 0.9 mm sample did not absorb as much as the thicker samples around 77°K, we decided to look for a change in the sign of the dispersion as the temperature of the sample was lowered below the laser temperature.

With the laser at 77°K and the sample at 65°K the FP profile had the opposite asymmetry (Figs. 59 and 60) implying that the nonlinear dispersion at lower temperatures is dominated by the R_1 line contribution, since the R_1 dispersive contribution due to both the ground state transition change sign below 77°K (Table 1).

The experimental data support our understanding of the transitions in ruby and also the basic theory of the device. In conclusion we would like to spell out the results of the ruby experiment point by point.

In the case of ruby, nonlinear refractive index contributions dominates over absorptive bistability. The origin of the nonlinear dispersion is the temperature insensitive, nonresonant excited pump and charge transfer band contribution (made nonlinear by the change of ground state population due to the R line transition) and the temperature dependent resonant R line contribution. At room temperature the nonresonant contribution dominates over the R line contribution, but at lower temperatures the R lines become more important. The device is under thermal equilibrium during operation, and there is very little thermal contribution to the nonlinear dispersion. The excited state contribution for a 5 mm, 0.05% concentration sample seems to be just enough nonlinearity for seeing room temperature bistability. Lowering the concentration to 0.03% we do not have sufficient nonlinearity for the device to operate at room

temperature. The threshold for the operation of the device is a few hundred watts/cm^2 experimentally, though the theory predicts lower thresholds. This could probably be accounted for on the basis of the cavity losses.

The switching time of the device is of the order of a few msecs to 20 msecs and corresponds to the order of magnitude of the ^2E lifetime of 3 to 5 msecs. Since the nonlinearity is controlled by the variation of the ^2E level population, this is a reasonable result.

An additional experimental result is the observation of overshoots in the output when the device is switched on and off by a square wave light pulse (Fig. 43). This was predicted theoretically (Sec. 2.2) for a purely dispersive device.

The ruby study shows that by driving a weakly absorbing transition, thereby changing the population distribution, it is possible to obtain large nonlinear refractive index contributions from nonresonant levels. This effect may be exploited in other materials such as semiconductors with exciton or impurity level transitions. We believe similar devices of micron dimensions containing 10^3 active centers with cross section 10^{-11} cm^2 can be constructed. Such devices would require approximately 10^{-7} watts for center lifetimes of nanoseconds.

TABLES

Table 1.

Maximum phase contribution from the R_1 and R_2 transitions for a 1 cm, 0.05% Cr^{3+}, 0° ruby. The laser has the dominant mode frequency at 77°K which is measured to be 14417.22 $\pm$ 0.05 cm^{-1}. The linewidths and the shift of the resonant frequency with temperature are obtained from Ref.28. The value of F_a and F_b are calculated for an intensity of 10 W/cm^2.

Table 2.

Nonresonant phase contribution at room temperature. The The center frequencies of the transitions and their linewidths have been obtained from Ref.38 and 40.

There are also specific contributions from the excited state transitions. The absorption lines are approximated by simple Lorentziansand they are also assumed to be homogeneously broadened.

	T (°K)	$\frac{\Delta\omega_{T_2}-\omega_0}{\omega_{T_2}-\omega_{T_1}}$	$\frac{\Delta\omega_{T_2}-\omega_{T_1}}{\omega_{T_2}-\omega_{T_1}}$	$\frac{\Delta\omega_0(T_1)}{\omega_0-\omega_L}$	$\frac{\Delta\omega_0(T_2)}{(\omega_0-\omega_L)}$	$\frac{\Delta\omega_0(T_1)}{\Delta\omega_{T_2}+\Delta\omega_{T_1}}$	$\frac{\Delta\omega_0(T_2)}{\Delta\omega_{T_2}+\Delta\omega_{T_1}}$	Γ $\omega 10^{12}$ cm^{-1}	$T_2=\frac{2}{\Gamma}$ cm	T_1 10^{-12} cm	$\frac{1}{2}\pi^2\frac{T_2}{\Delta\omega_0 T_2}$	$\frac{T_2}{\Delta\omega_0 T_2}$	$\int\sigma_\perp dv$ $\times 10^{-19}$cm	$\int\sigma_0 dv$ $\times 10^{-19}$cm	$\int\sigma_0 dv$ $\times 10^{-19}$cm	$a_0=\frac{T_2}{A}\int a_0 dv$ cm^{-1}	$a_0=\frac{T_2}{A}\int a_0 dv$ cm^{-1}	$\frac{a_0}{(1+\gamma_0^2)}$	$\frac{a_0}{(1+\gamma_0^2)}$	$\phi_0=\frac{a_0\gamma_0}{(1+\gamma_0^2)}$	$\phi_0=\frac{a_0\gamma_0}{(1+\gamma_0^2)}$	T_1T_2 10^{-24}cm^2	$F=\frac{1}{2}\pi^2 T_1T_2$	$F=\frac{1}{2}\pi^2 T_1T_2$	$\theta=(1+F)\frac{\phi_0^2}{\gamma_0^2}$	(1-θ)
R_1	65	.15	.138	-.05	.342	.088	.48	.11	18.18	12.3	1.6	2.73	2.9	1.28	1.62	11.85	14.99	3.33	.194	5.33	1.69	5	11.2	14	.656	.344
	70	-.200	.08	-.05	.342	.03	.422	.116	17.24	12.3	.517	7.28	2.9	1.28	1.62	11.24	14.22	8.87	.263	4.59	1.91	2.12	4.75	5.94	.646	.354
	77	-.288	0	-.05	.342	-.05	.342	.141	14.18	12.3	-.709	4.85	2.9	1.28	1.62	9.24	11.70	6.15	.477	-4.36	2.313	1.74	3.9	4.87	.633	.367
	85	-.500	-.212	-.05	.342	-.262	.13	.182	10.99	12.45	-2.88	2.0	2.9	1.28	1.62	7.16	9.07	.77	1.81	-2.22	3.62	1.36	3.05	3.81	.621	.379
	100	-.730	-.442	-.05	.342	-.492	-.1	.282	7.09	12.6	-3.49	-.709	2.9	1.28	1.62	4.62	5.85	.35	3.89	-1.22	-2.76	.89	2.0	2.49	.603	.397
	120	-1.82	-1.53	-.05	.342	-1.58	-1.18	.647	3.09	12.75	-1.02	-3.65	2.9	1.28	1.62	2.01	2.55	.985	.178	-1.00	-.65	.39	.874	1.09	.587	.413
	150	-3.14	-2.85	-.05	.342	-2.9	-2.51	1.45	1.38	12.6	-4.0	-3.46	2.9	1.28	1.62	.899	1.14	.053	.087	-.212	-.30	.174	.39	.49	.570	.430
	200	-6.74	-6.45	-.05	.342	-6.5	-6.1	3.34	.599	12.0	-3.89	-3.65	2.9	1.28	1.62	.39	.494	.024	.034	-.093	-.124	.072	.16	.20	.552	.448
	250	-15.8	-15.5	-.05	.342	-15.55	-15.16	8.29	.241	11.1	-3.75	-3.65	3.3	1.45	1.85	.178	.227	.012	.016	-.045	-.058	.027	.06	.076	.542	.458
	300	-20.0	-19.7	-.05	.342	-19.75	-19.36	13.10	.153	10.05	-3.02	-2.96	3.5	1.54	1.96	.12	.153	.012	.0156	-.036	-.046	.015	.03	.04	.535	.465
R_2	65	.15	-	29	-	28.85	-	.11	18.18	12.3	525	-	1.7	1.65	-	-	-	-	-	-	-	2.23	5.82	-	-	-
	70	-.2	-	29	-	28.8	-	.116	17.24	12.45	497	-	1.7	1.65	-	-	-	-	-	-	-	2.15	5.61	-	-	-
	77	-.288	-	29	-	28.7	-	.141	14.18	12.6	407	-	1.7	1.65	-	-	-	-	-	-	-	1.79	4.67	-	-	-
	85	-.5	-.212	29	29	28.5	-	.16	12.5	12.75	359	-	1.7	1.65	-	-	-	-	-	-	-	1.59	5.22	-	-	-
	100	-.73	-.442	29	29	28.3	28.6	.21	9.52	12.6	271	-	1.7	1.65	-	8.0	-	-	-	.006	-	1.20	4.17	-	-	-
	120	-1.82	-1.53	29	29	27.2	27.3	.5	4.00	12.75	109	-	1.7	1.65	.05	3.36	-	-	-	.015	-	.51	1.33	-	-	-
	150	-3.14	-2.85	29	29	25.9	26.2	1.1	1.82	12.6	47.1	47.7	1.75	1.7	.05	1.58	-	.0007	-	.036	-	.23	.60	-	-	-
	200	-6.74	-6.95	29	29	22.3	22.6	3.3	.61	12.0	13.6	13.8	1.8	1.75	.05	.543	-	.003	-	.041	-	.13	.34	-	-	-
	250	-15.8	-15.5	29	29	13.2	13.5	5.7	.35	11.1	4.62	2.0	1.8	1.75	.05	.312	-	.014	-	.065	-	.039	.101	-	-	-
	300	-20.0	-20.0	29	29	9	9	10	.2	10.05	1.8	1.8	1.9	1.85	.05	.188	.005	.044	.001	.079	.002	.02	.052	-	-	-

Table 1

FINAL STATE	TRANSITION FREQUENCY ω_T (cm^{-1})	$\Delta\omega_g = \omega_T - \omega_{LASER}$	$\Delta\omega_e = \omega_T - 2\omega_{LASER}$	α (PEAK) (cm^{-1})	WIDTH Γ (cm^{-1})	$T_2' = \frac{2}{\Gamma}$ (cm)	$y_g = \Delta\omega_g T_2'$	$y_e = \Delta\omega_e T_2'$	$\frac{\alpha_g}{(1+y_g^2)}$	$\frac{\alpha_e}{(1+y_e^2)}$	$\phi^g = \frac{\alpha_g y_g}{(1+y_g^2)}$	$\phi^e = \frac{\alpha_e y_e}{(1+y_e^2)}$
$^4T_2$	18179	3762	-10655	3.3	2143	.00093	3.5	- 9.9	.249	.033	.72	-.327
$^4_aT_1$	24393	9976	-4441	3.6	2453	.00082	8.18	- 3.64	.053	..253	.434	-.921
$^2_bT_2, ^2_cT_1, ^2E$	31964	17547	3130	0.48	1964	.001	17.6	3.13	.002	.044	.035	.138
$^2_bT_2, ^2_cT_1, ^2E$*	32607	—	3807	1.41	2143	.000933	—	3.55	—	.104	—	.368
$^2_bT_1$*	37143	—	8342	1.61	2321	.00086	—	7.17	—	.031	—	.220
$^4_bT_1$	39036	24619	10202	1.29	3214	.00062	15.3	6.33	.005	.030	.077	.190
$^2_cT_2, ^2A_2$	41071	—	12271	2.03	2500	.0008	—	9.82	—	.021	—	.206
CHARGE TRANSFER BANDS $t_{2g}^3, ^2E_g, ^2T_{1g}$	54400	39983	25600	73.5	6000	.00033	13.2	8.53	.419	.9960	5.53	8.50
									TOTAL		6.95	8.37

* TRANSITION TO THESE STATES OCCUR ONLY WHEN THE ATOM IS IN ^2E STATE

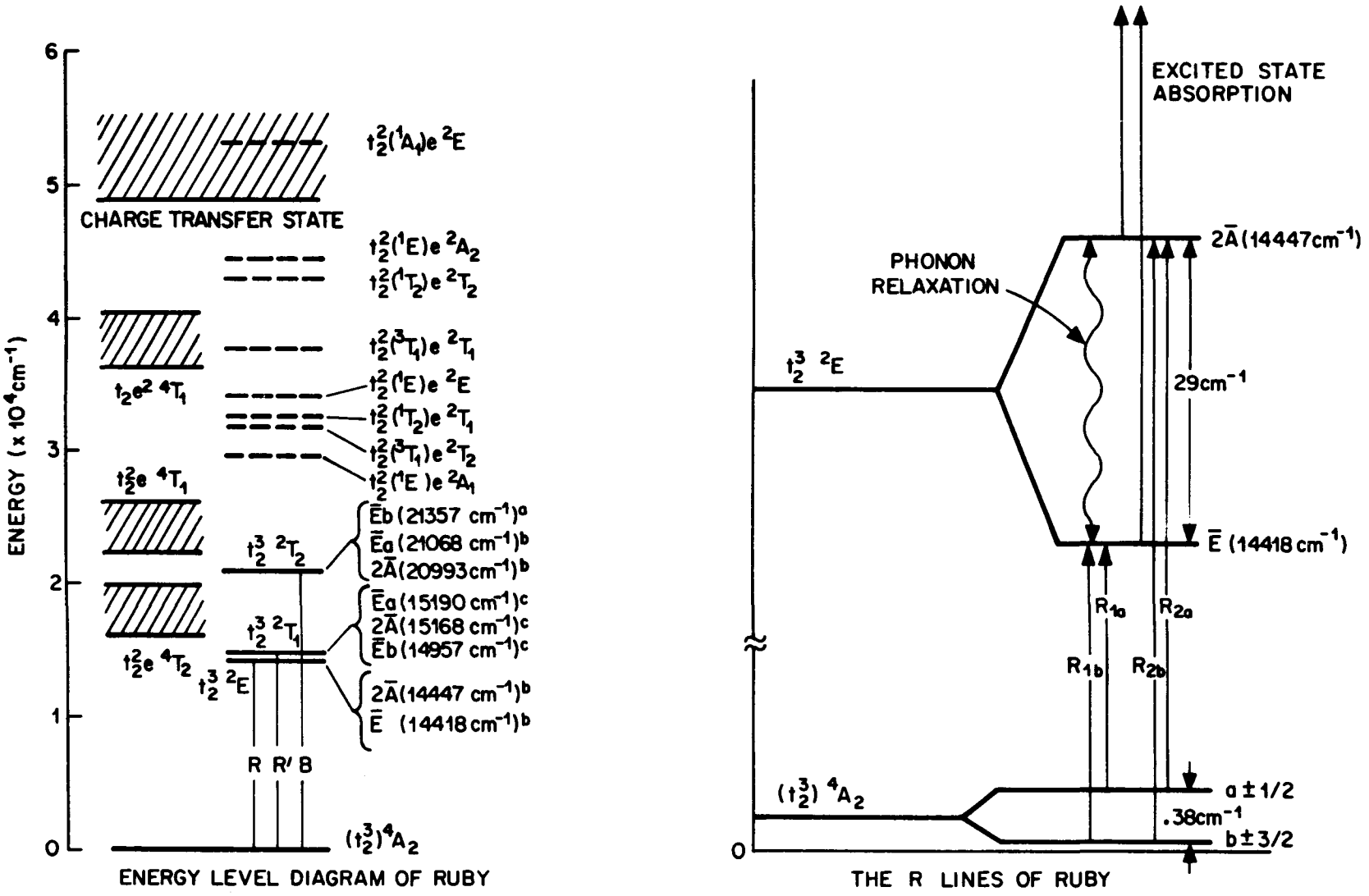
ENERGY (x 10⁴cm⁻¹)
CHARGE TRANSFER STATE
ENERGY LEVEL DIAGRAM OF RUBY
EXCITED STATE ABSORPTION
PHONON RELAXATION
29cm⁻¹
.38cm⁻¹
THE R LINES OF RUBY

Figure 21

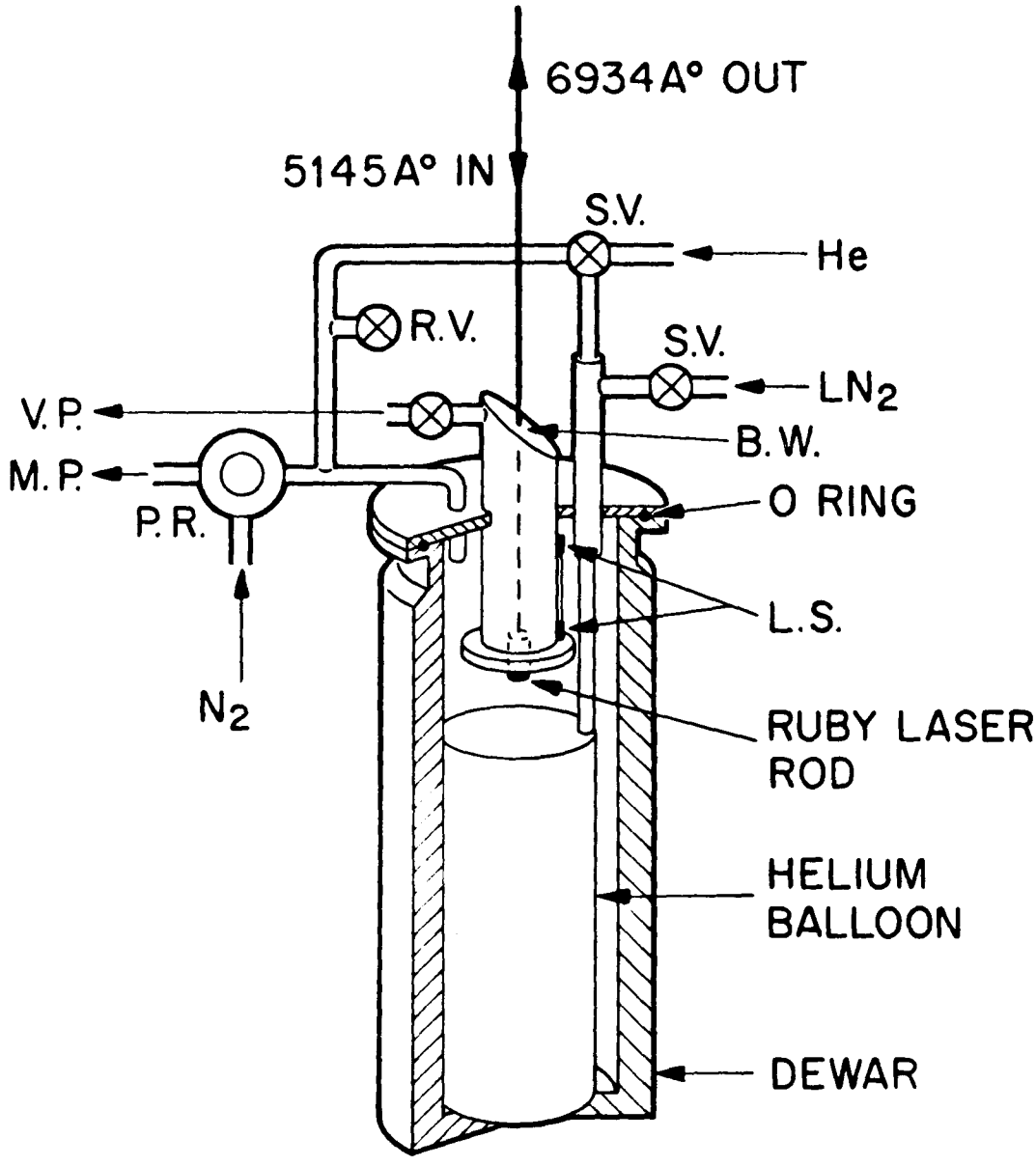

Fig. 22 Ruby laser design. M.P.-mechanical pump, P.R.-pressure regulator, V.P.-Vacion vacuum pump, R.V.-relief valve, S.V.-solenoid valve, B.W.-Brewster's windows, L.S.-level sensors.

Figure 22

Ruby laser pumping and F.P. locking scheme.

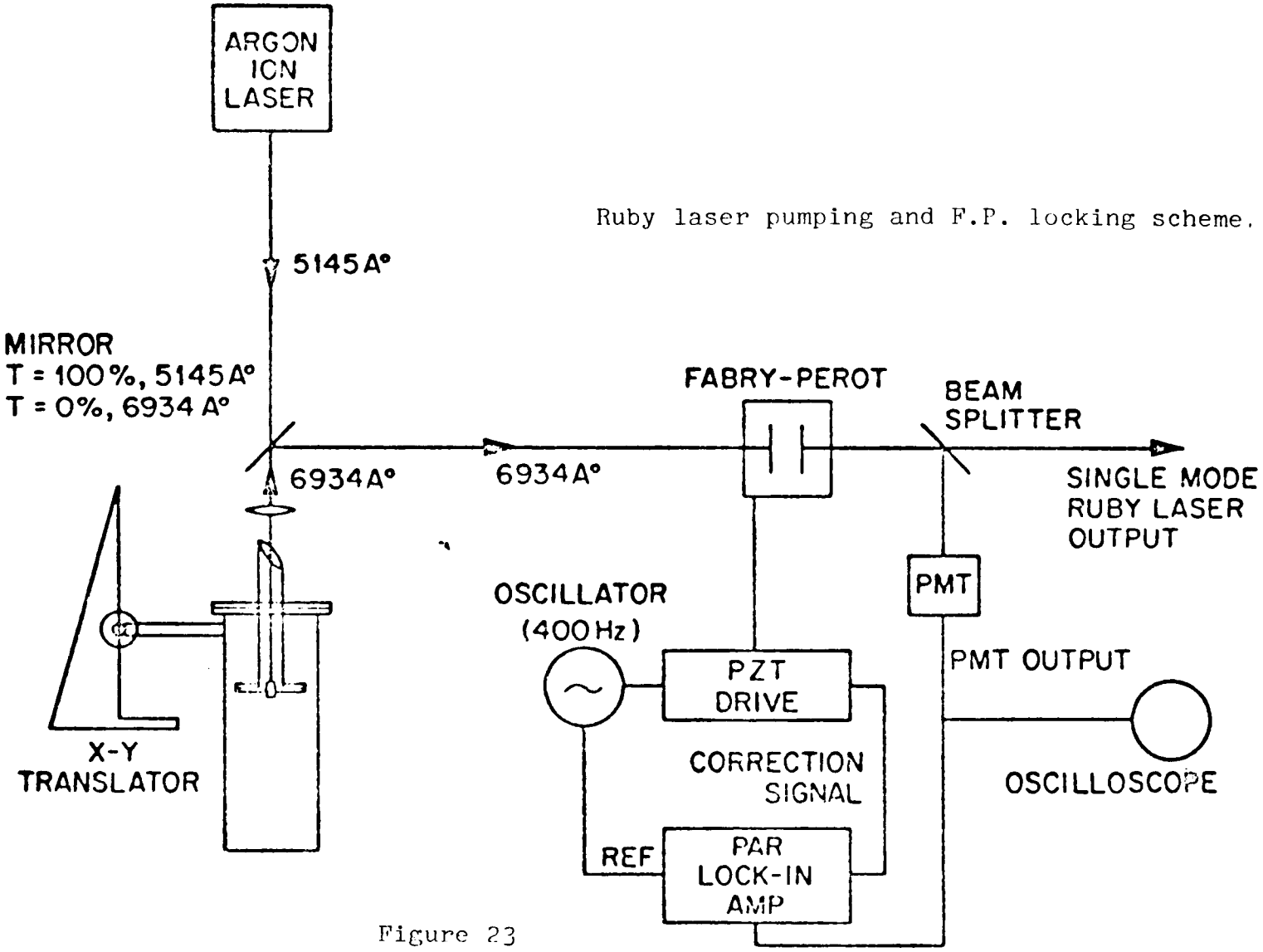

Figure 23

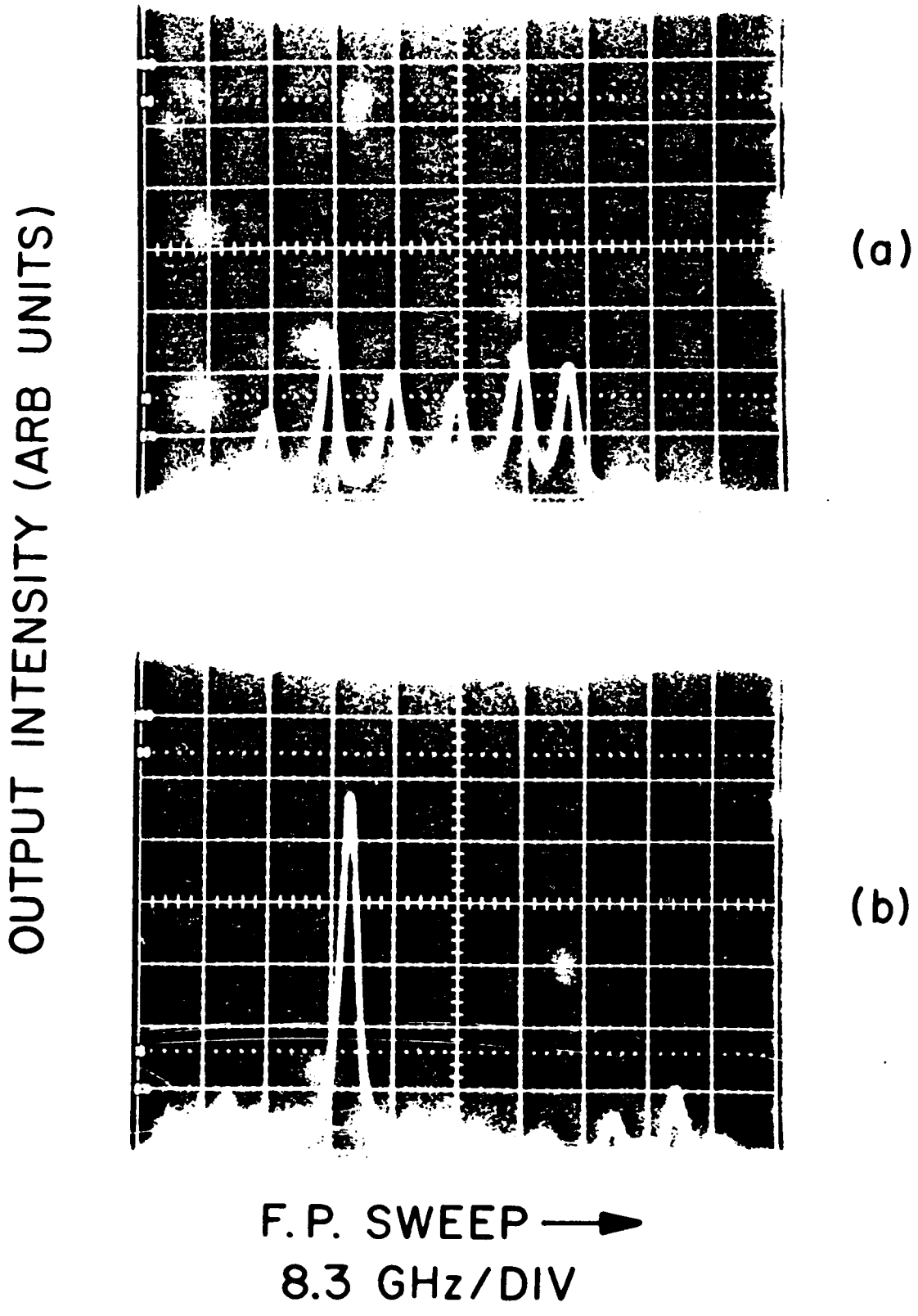

Fig. 24 (a) A typical mode pattern of the ruby laser output

(b) Mode pattern with a dominant mode.

Fig. 25 Incident and transmitted mode pattern through a ruby absorber. The detector for transmitted modes was insensitive to the He-Ne laser line. There is almost complete transmission in the last few modes on the right.

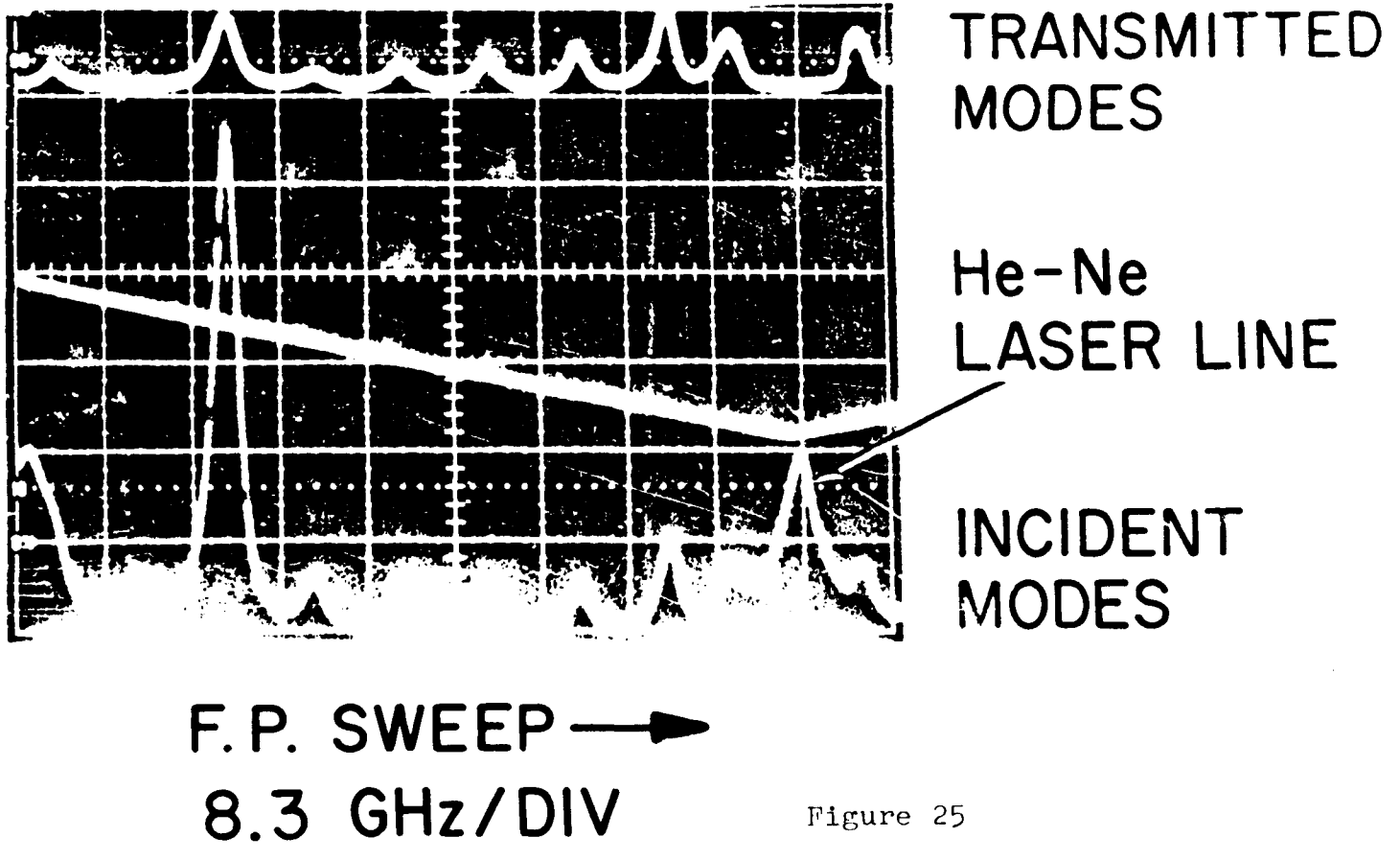

Figure 25

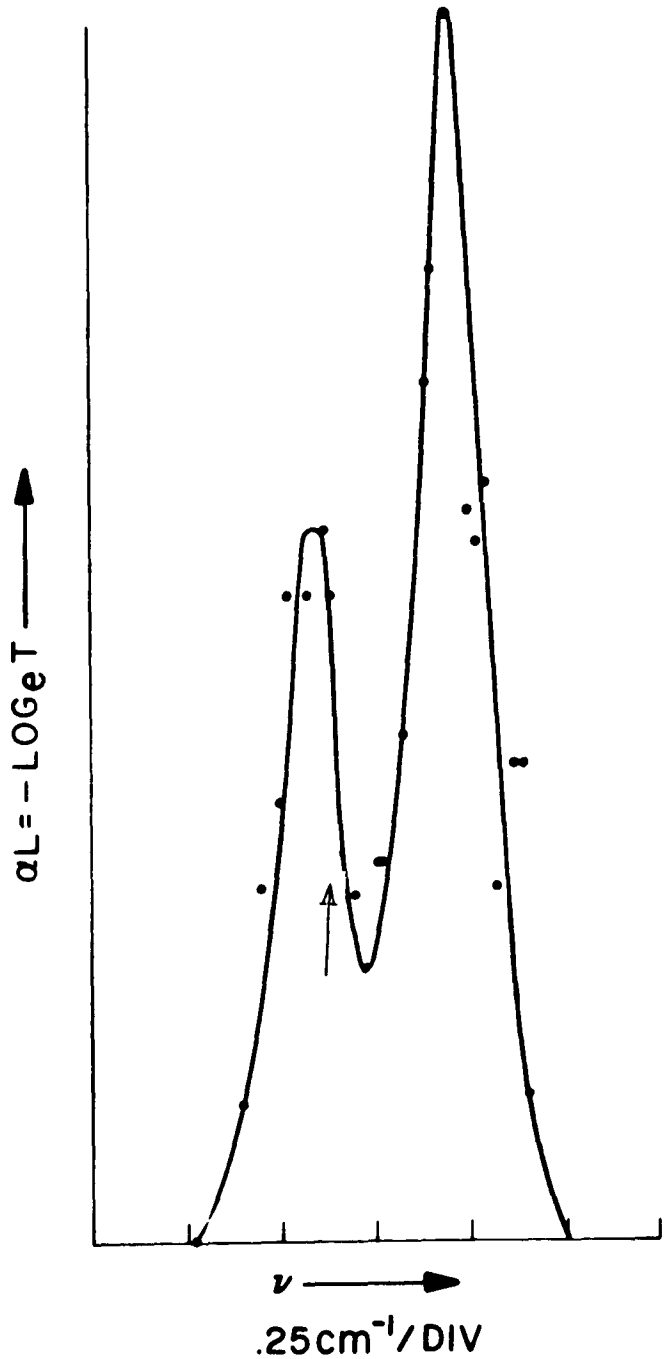

Fig. 26 Absorption profile of a .05%, Cr^{3+} concentration 0° and 0.9 mm thick ruby sample. the peak α measured was 14.7 cm^{-1}, where $\alpha = -L^{-1} \ln (T)$, and T is the fractional light transmission.

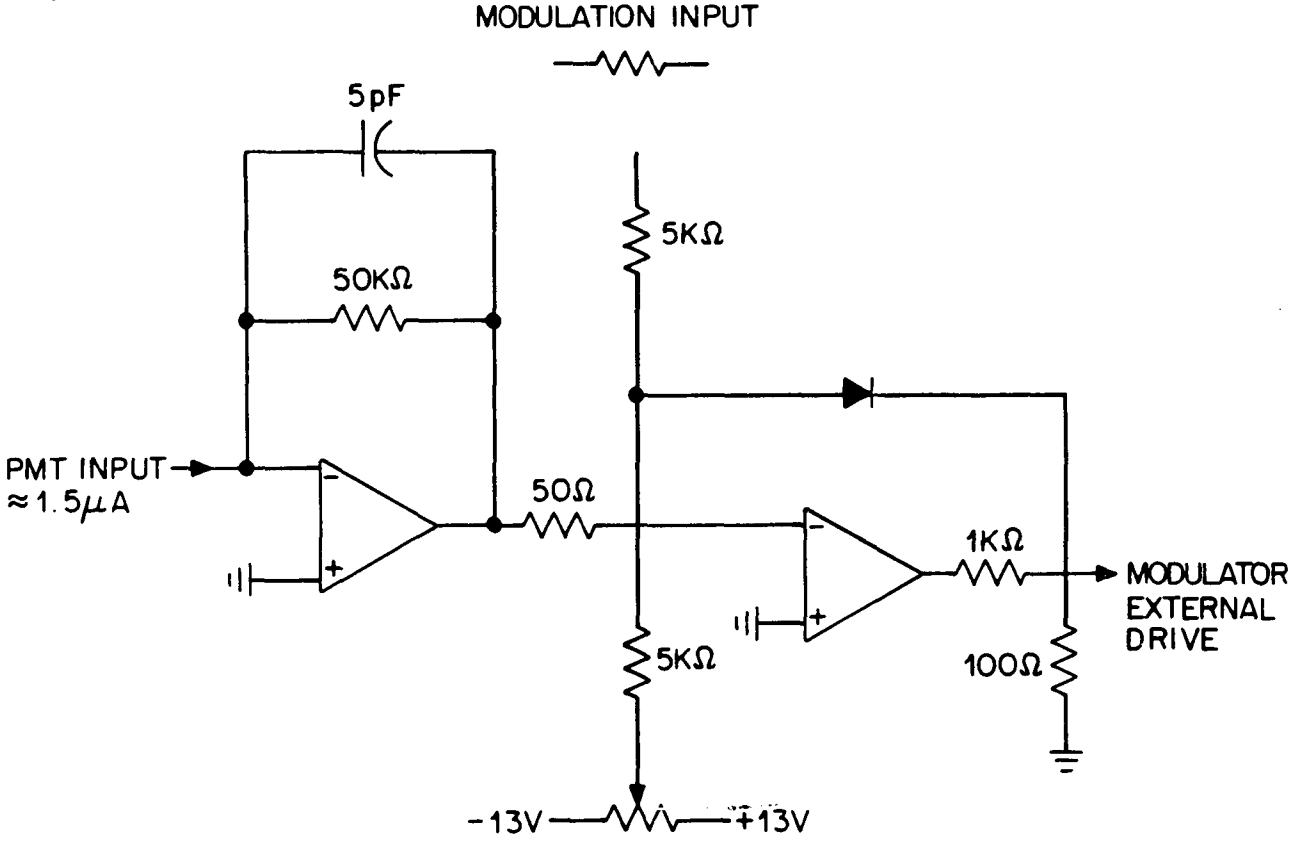

AMPLITUDE STABILIZING MODULATOR FEED-BACK CIRCUIT

Figure 27

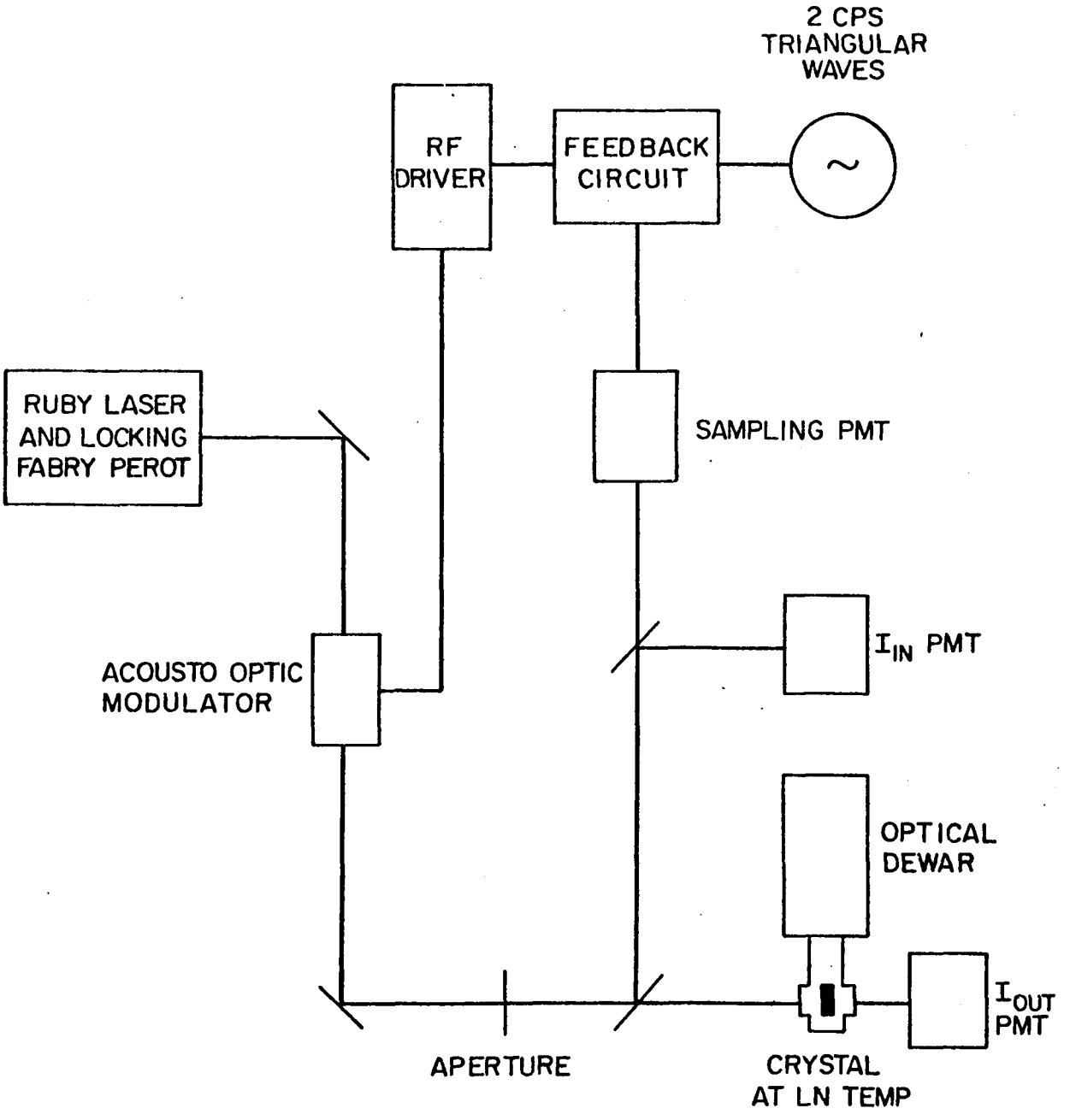

SET-UP FOR MEASURING NONLINEARITY IN RUBY

Figure 28

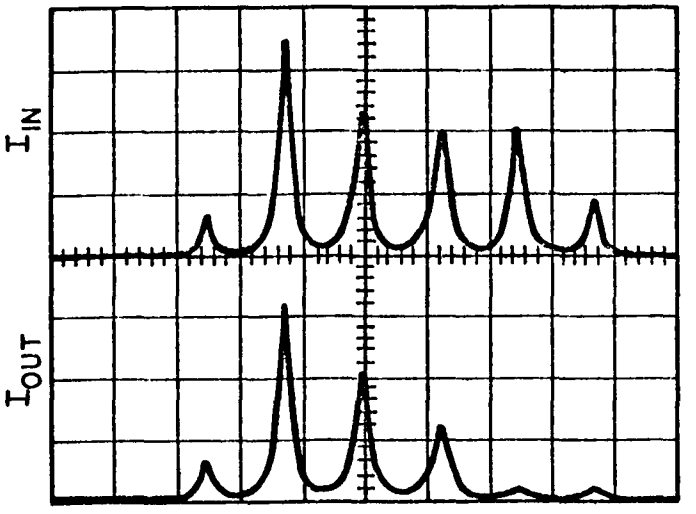

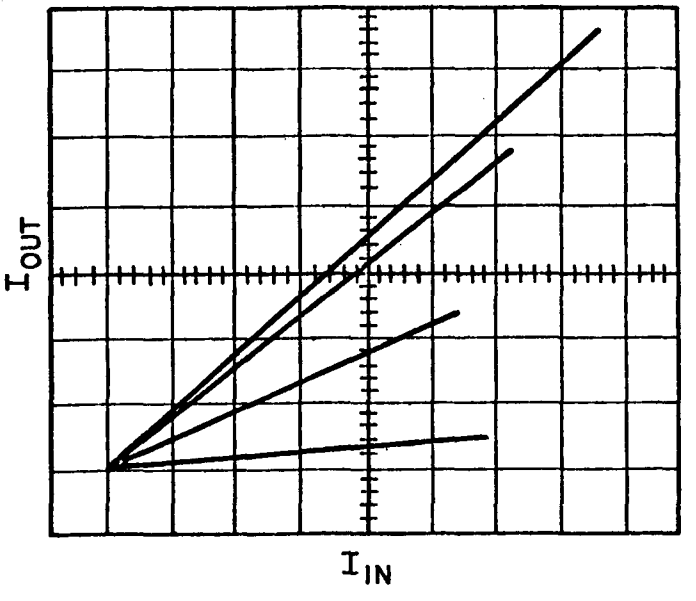

FIG. 9 SIMULTANEOUS ABSORPTION DISPLAYS

Figure 29

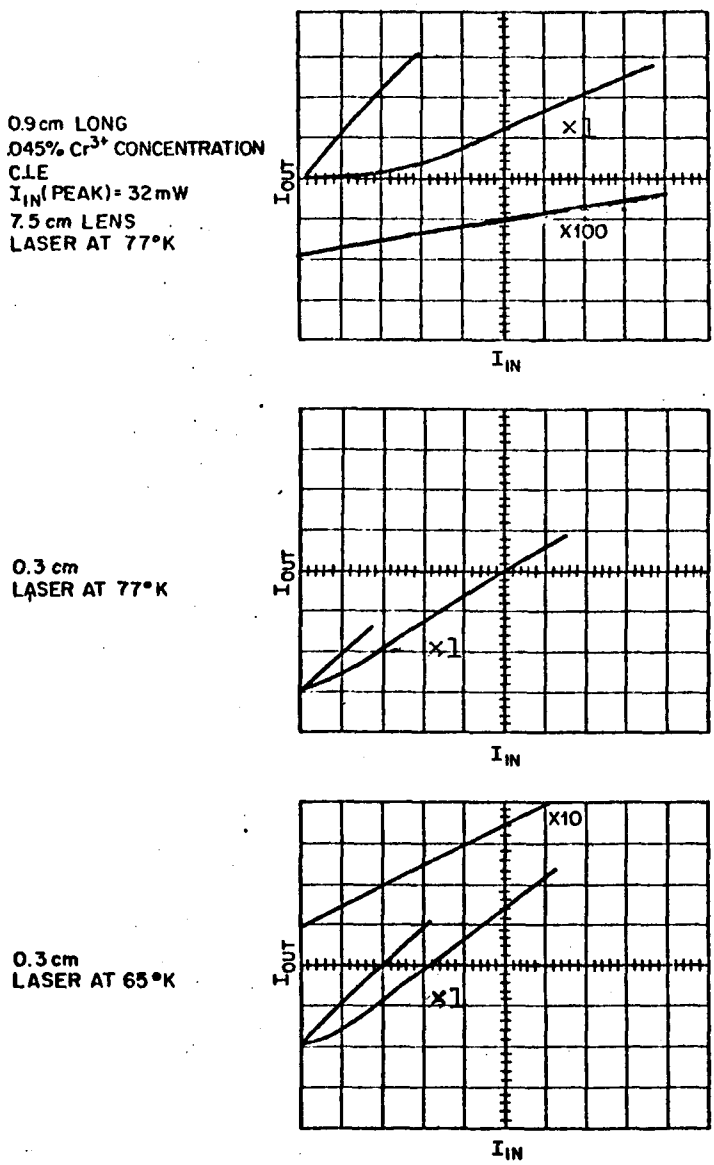

FIG.10 ONSET OF NONLINEARITY ON INTRODUCING A LENS

The vertical trace expansion is indicated by x10 and x100.

Figure 30

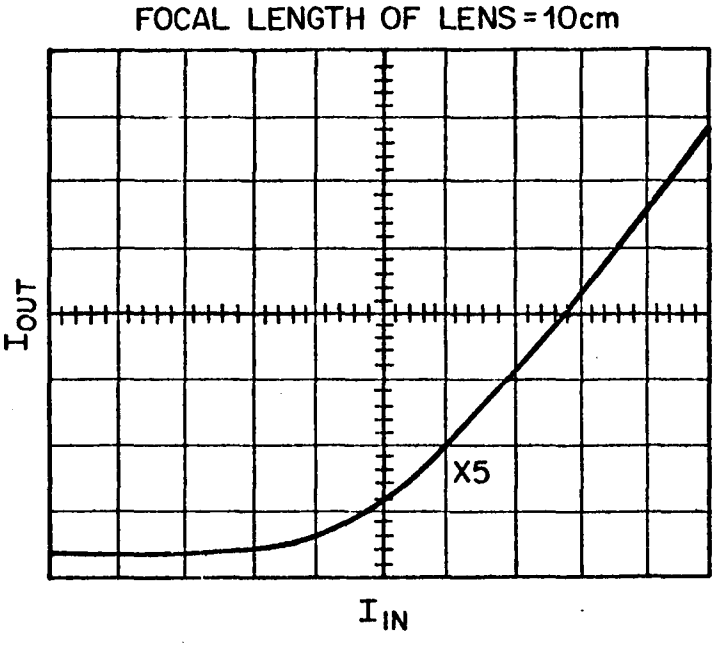

The vertical trace expansion is indicated by x5.

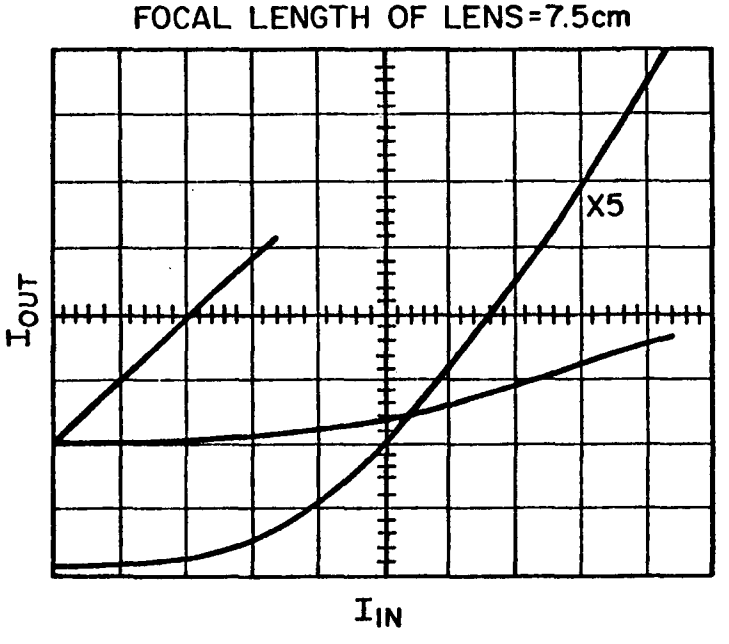

FIG.11 DEPENDENCE OF SATURATION ON FOCAL LENGTH OF THE LENS

FIGURE 31

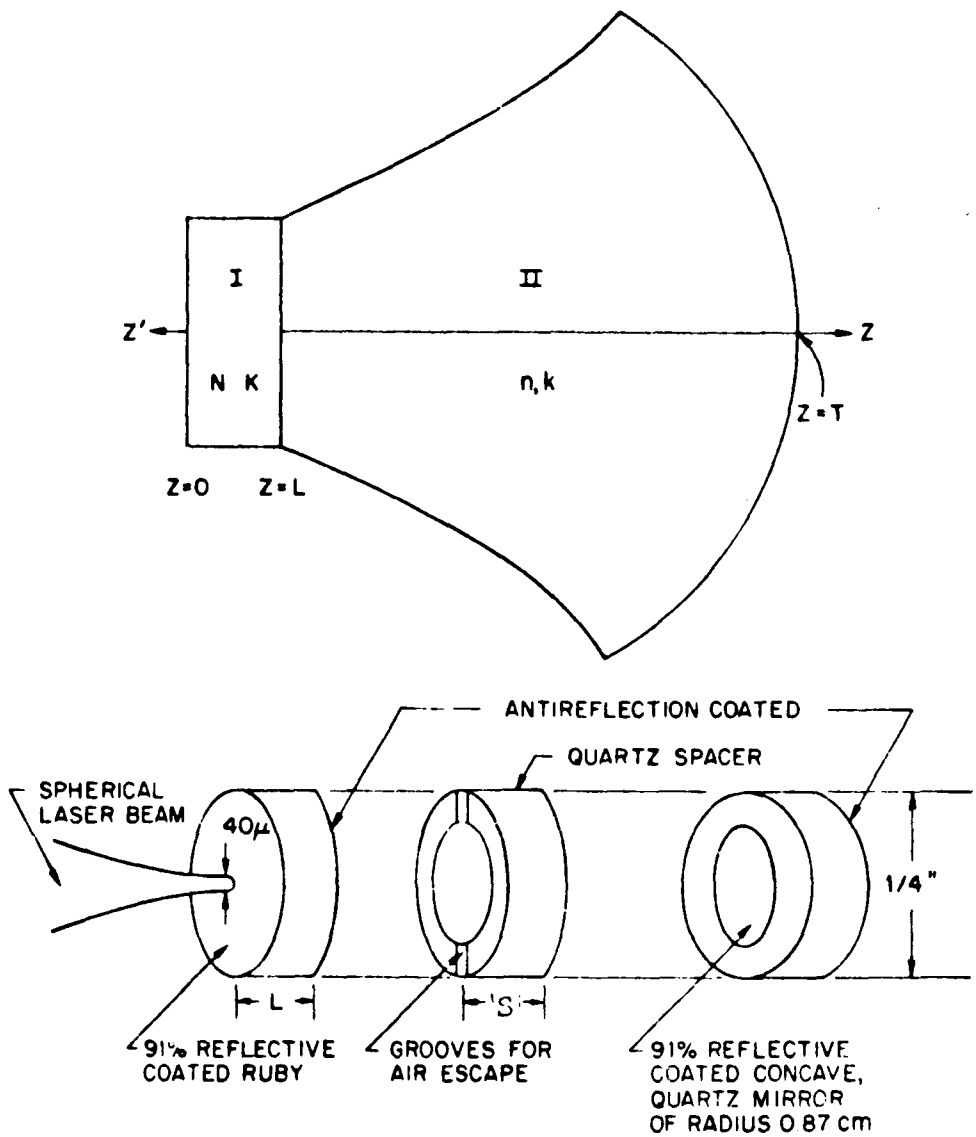

The device cavity.

Figure 3c

He - Ne LASER
CAVITY WITH 3mm RUBY INSIDE, IMMERSED IN LN
MAXIMUM TRANSMISSION IN TEM_{00} = 40%
CAVITY SWEPT BY PUMPING ON LN

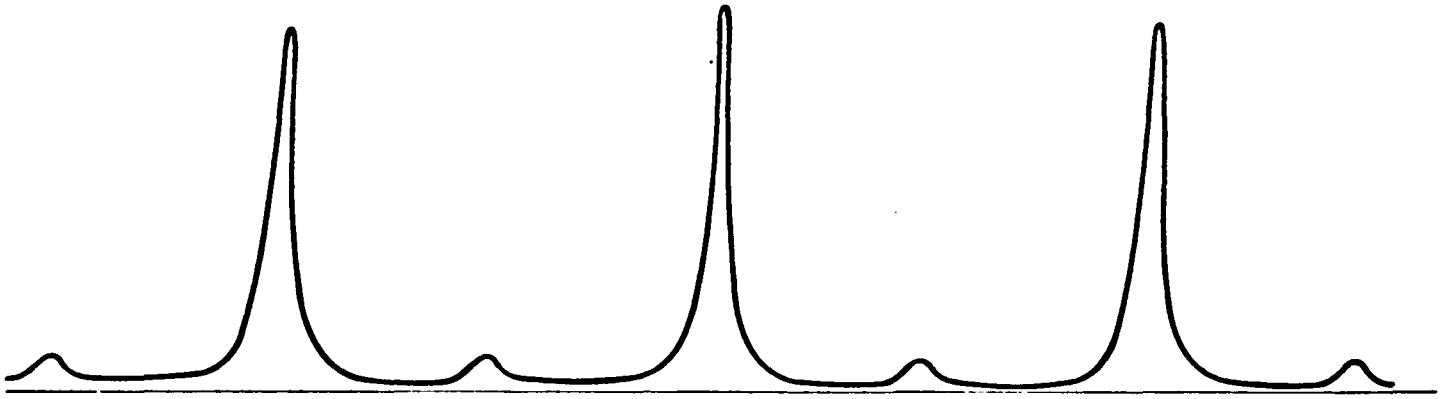

Figure 33

CAVITY AT ROOM TEMP WITH .05%, 0°, 5 mm RUBY.

NEUTRAL DENSITY 1.6 IN THE INPUT BEAM AND HENCE SYMMETRICAL OUTPUT.

20% MAXIMUM TRANSMISSION IN TEM_{noo}.

CAVITY SWEPT BY HEATING THE SAMPLE AND THEN LETTING IT COOL.

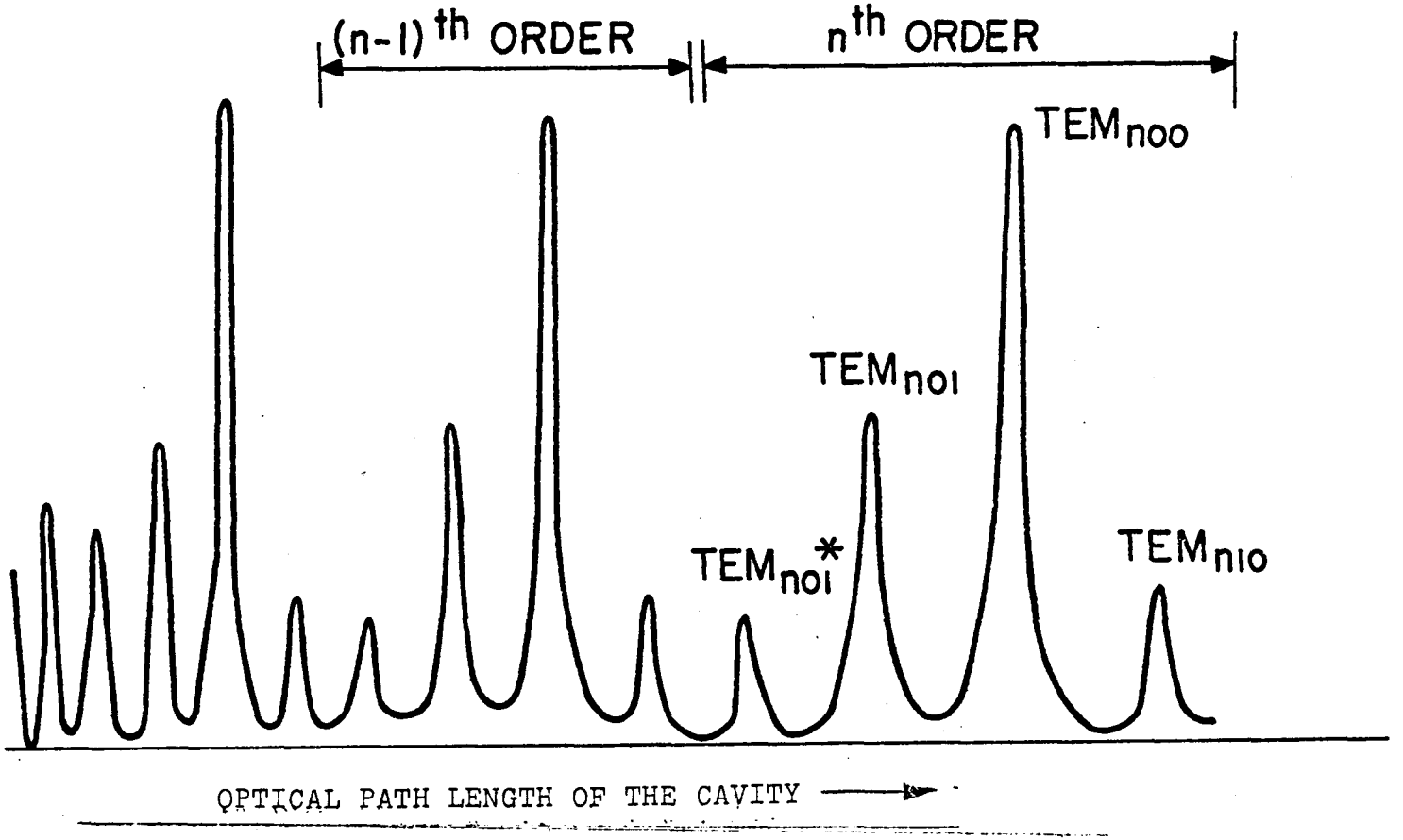

Figure 34

RUBY REPLACED BY 5 mm, QUARTZ MIRROR (FLAT)
PEAK TRANSMISSION IN TEM_{noo} IS 54 %

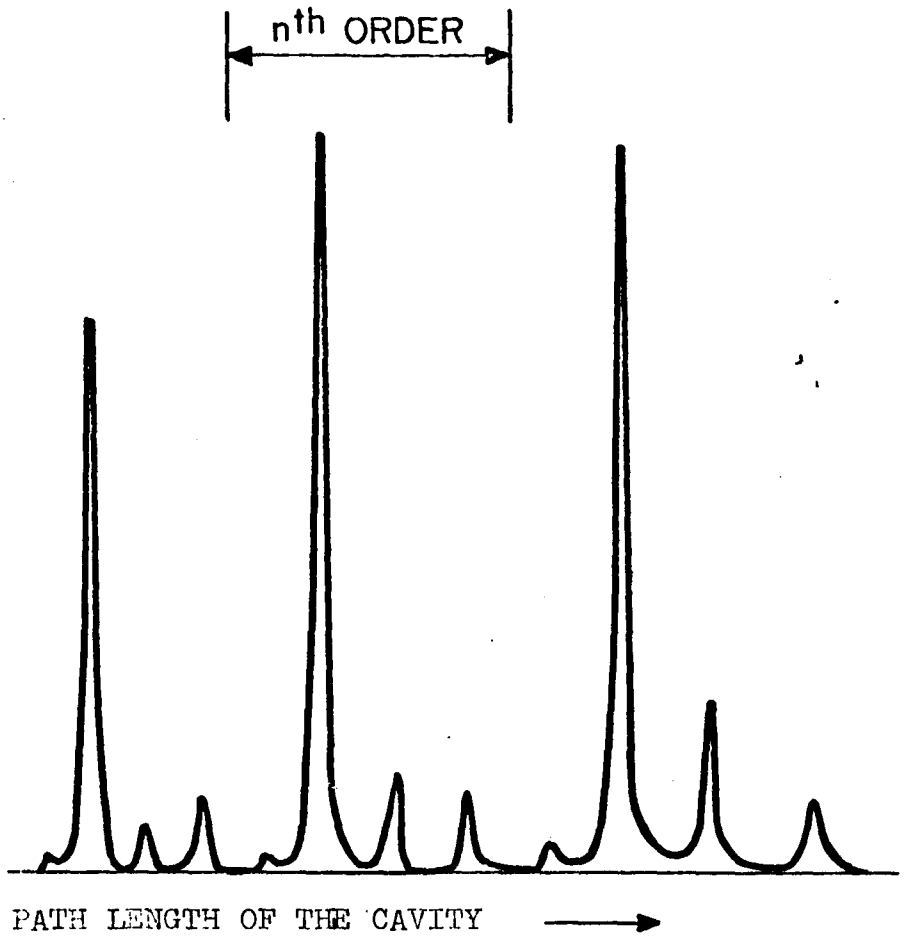

Figure 35

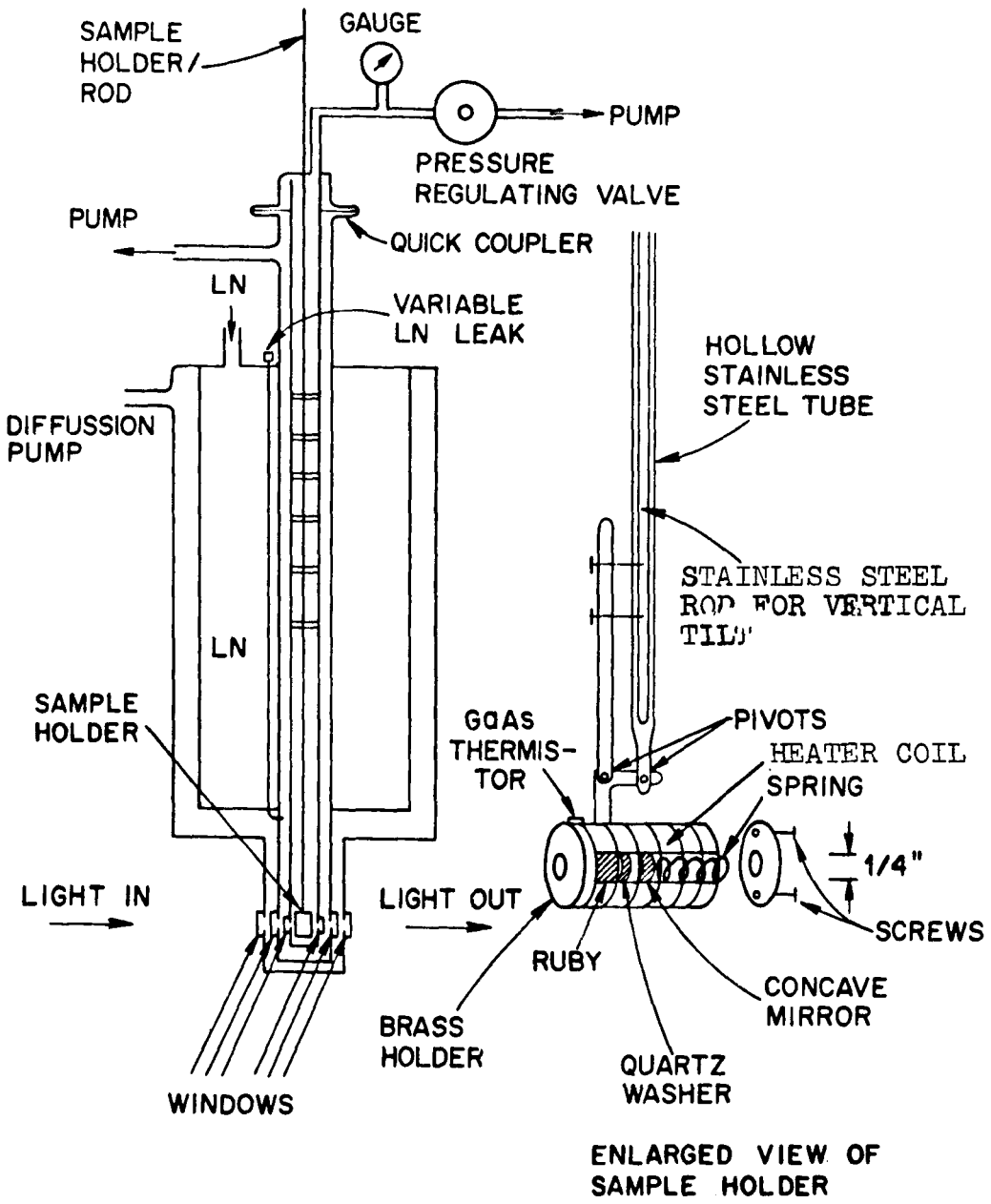
SAMPLE HOLDER/ ROD
GAUGE
PUMP
PRESSURE REGULATING VALVE
PUMP
QUICK COUPLER
LN
VARIABLE LN LEAK
HOLLOW STAINLESS STEEL TUBE
DIFFUSSION PUMP
STAINLESS STEEL ROD FOR VERTICAL TILT
LN
SAMPLE HOLDER
GaAs THERMIS-TOR
PIVOTS
HEATER COIL
SPRING
1/4"
LIGHT IN
LIGHT OUT
SCREWS
RUBY
CONCAVE MIRROR
BRASS HOLDER
QUARTZ WASHER
WINDOWS
ENLARGED VIEW OF SAMPLE HOLDER

Figure 36

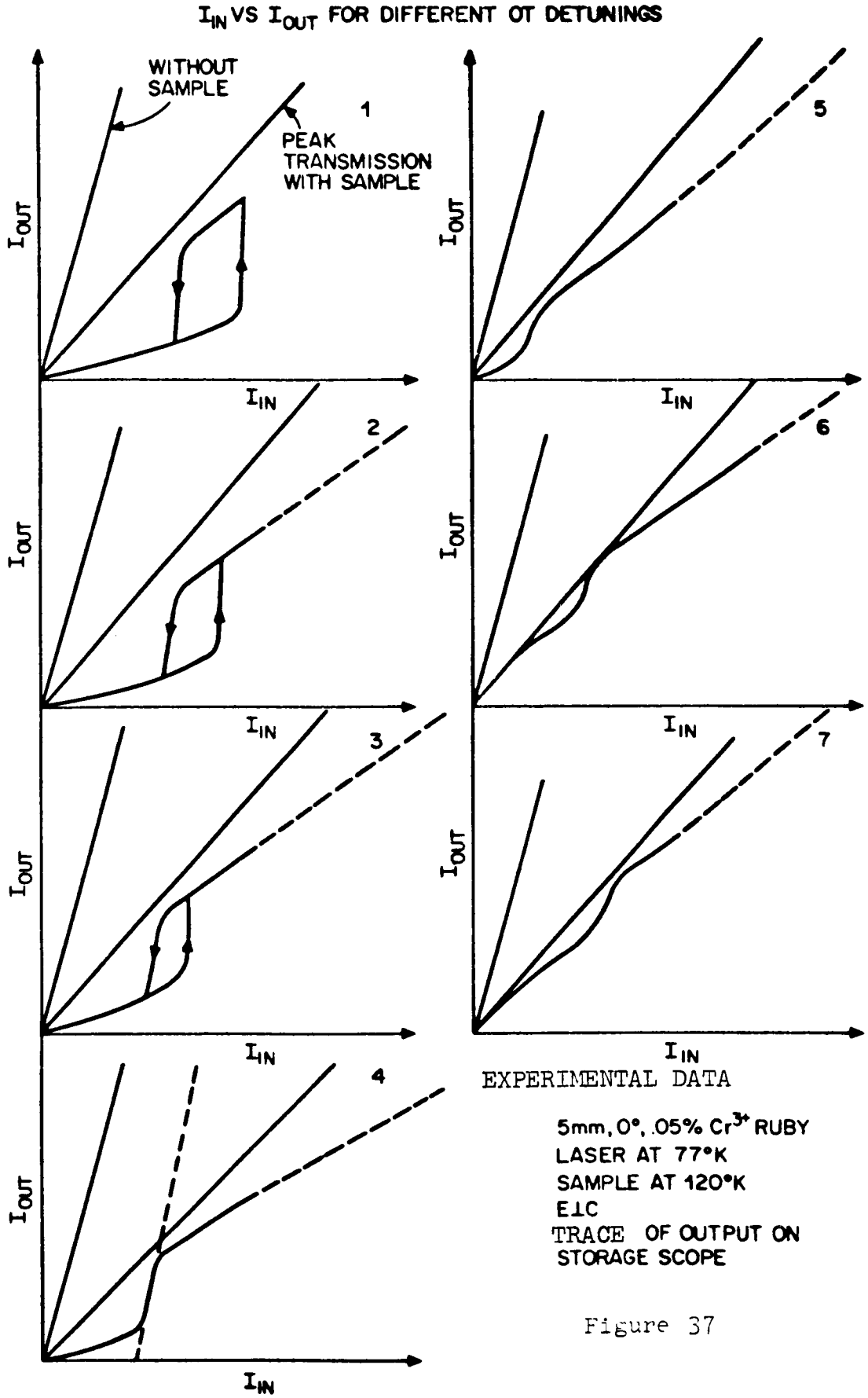
I_{IN} VS I_{OUT} FOR DIFFERENT OT DETUNINGS
WITHOUT SAMPLE
1
PEAK TRANSMISSION WITH SAMPLE
2
3
4
5
6
7
I_{OUT}
I_{IN}
EXPERIMENTAL DATA
5mm, 0°, .05% Cr^{3+} RUBY
LASER AT 77°K
SAMPLE AT 120°K
E⊥C
TRACE OF OUTPUT ON STORAGE SCOPE

Figure 37

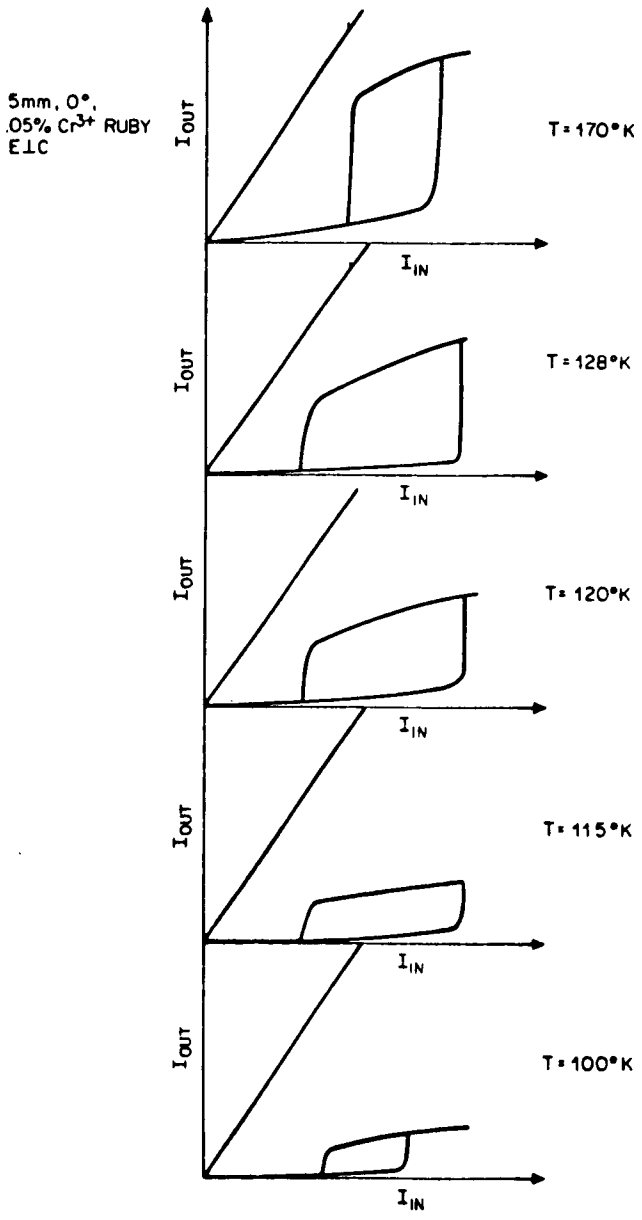

Fig. 38 Characteristic curves for a 5 mm, 0.05% Cr^{3+}, 0° device at different temperatures.

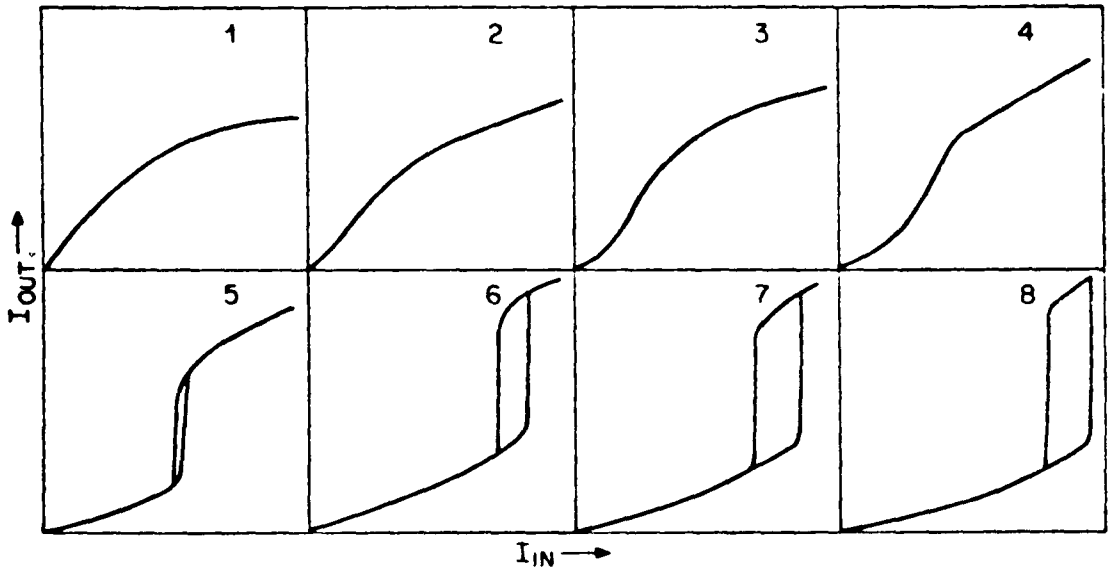

ROOM TEMPERATURE BISTABILITY

- I_{IN} VS I_{OUT} FOR DIFFERENT DETUNINGS
- 5mm, 0°, .05% CONCENTRATION RUBY
- E⊥C
- I_{IN} (MAX) IS 21mW INCLUDING LOSSES IN DEWAR

Figure 39

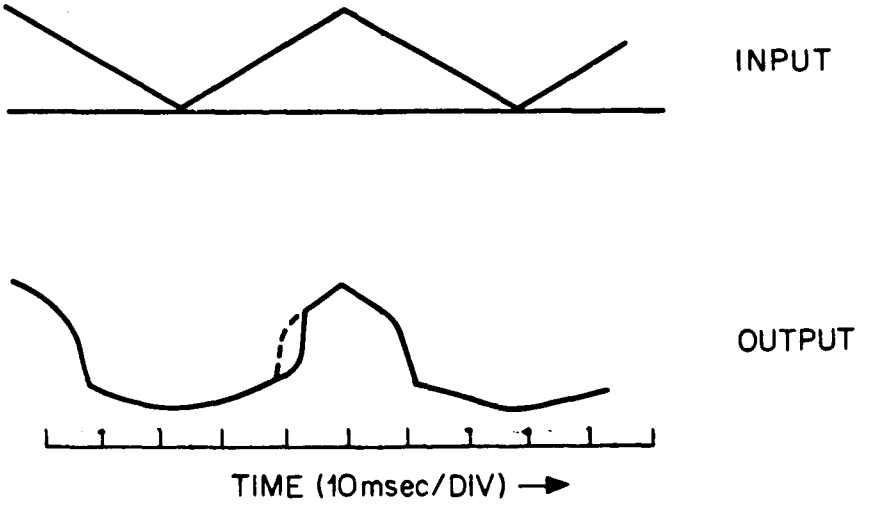

ASYMMETRIC RESPONSE TO TRIANGULAR
INPUT UNDER BISTABLE OPERATION

Figure 40

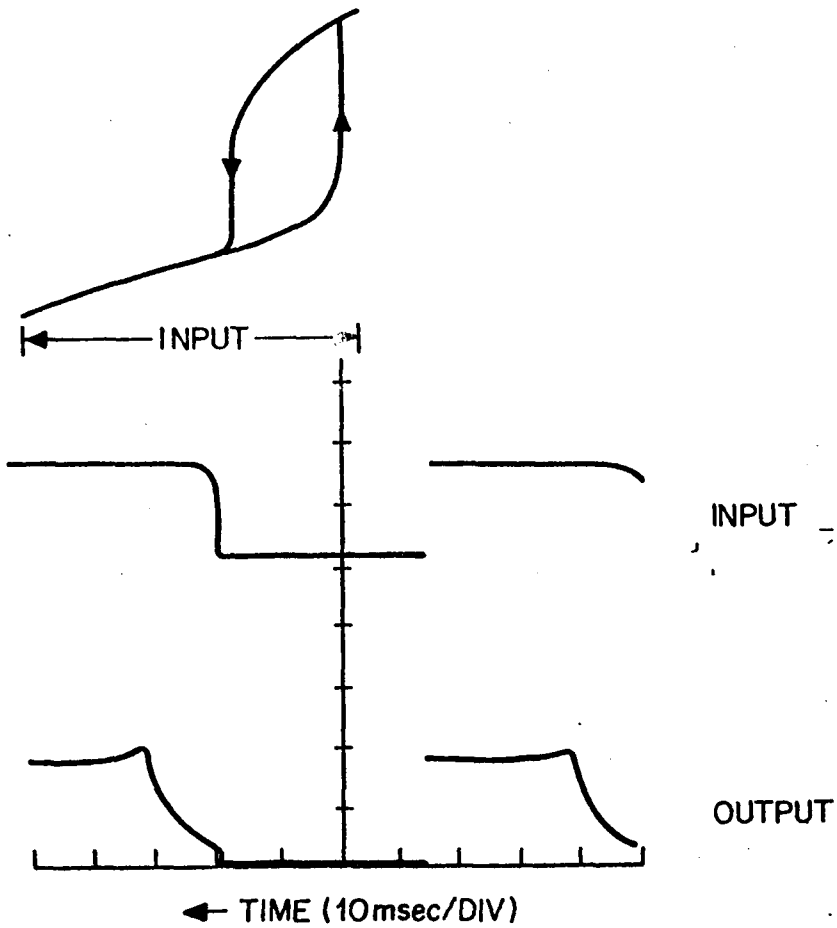

Figure 41

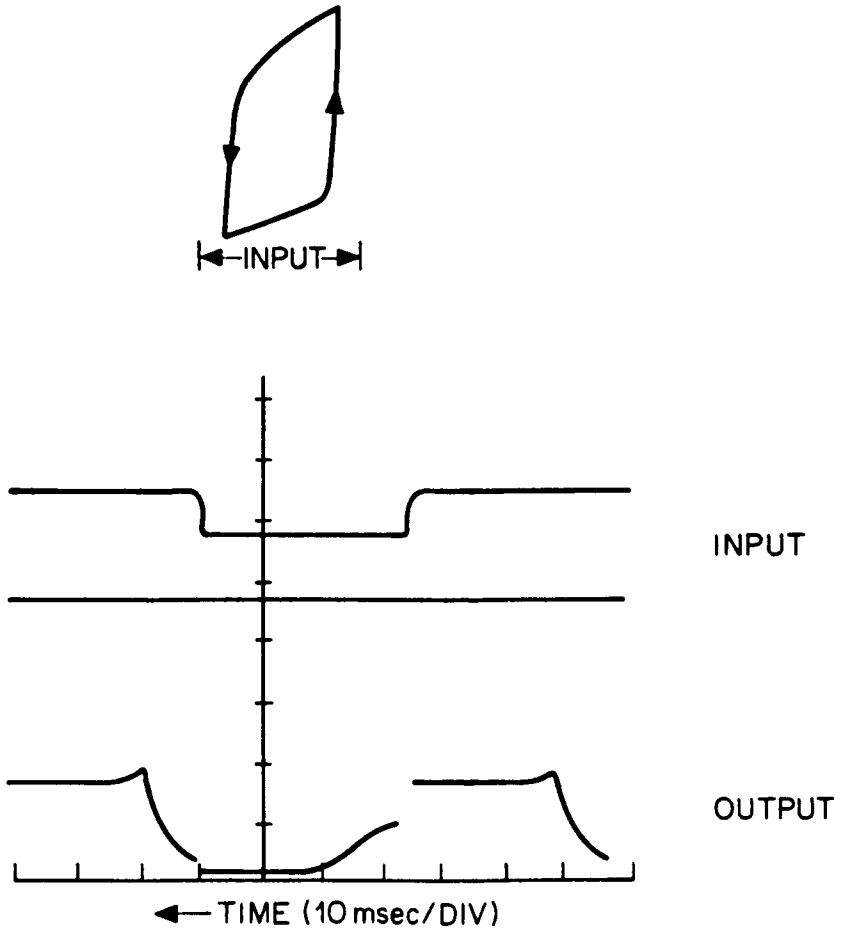

Figure 42

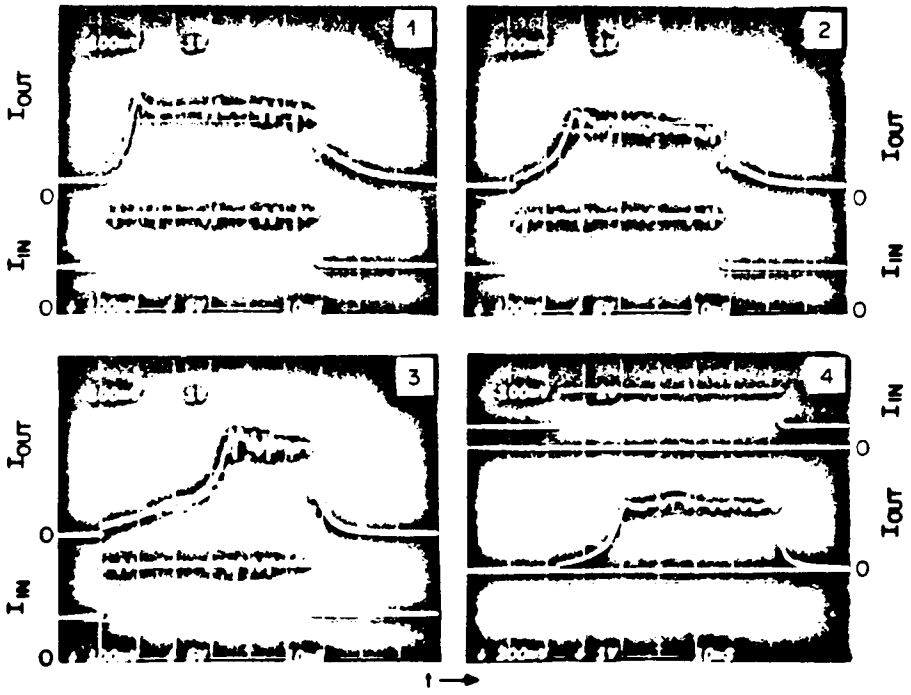

RISE AND FALL TIMES

- 80Hz SQUARE MODULATION ON A DC LEVEL
- ① TRANSISTOR MODE
- ③ BISTABLE MODE
- NOTE OVERSHOOT IN THE RISE AND FALL, IN ①, ② & ③

Figure 43

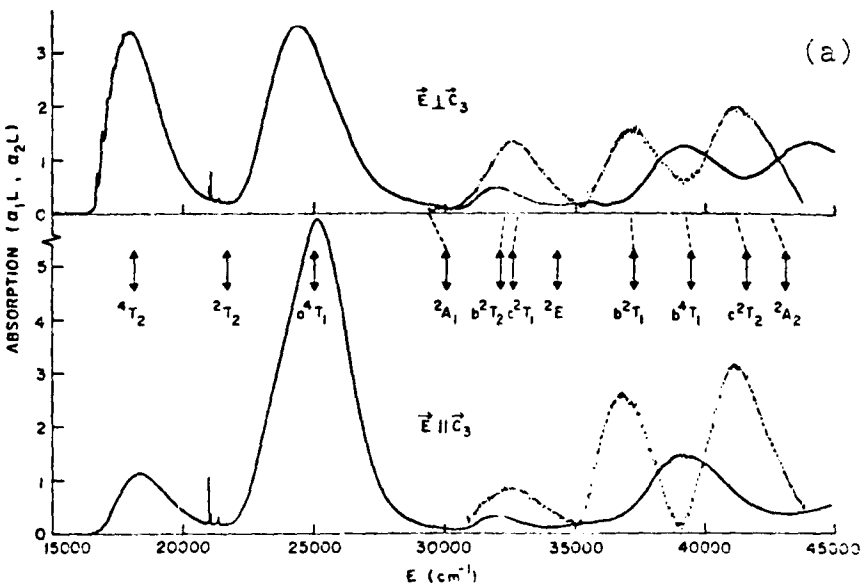

Ground- and excited-state absorption spectra of ruby (sample 3) at 103 K. The excited-state spectra are shifted by the ^2E state energy and normalized to 100% population in the metastable excited states.

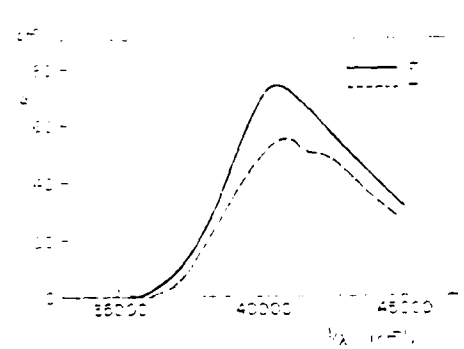

Absorption spectrum of ruby in the excited states at room temperature

Figure 44

Computer plot of the characteristic curves using Eq.2.3 and the data of table 1 and 2. The mistuning angle is indicated for each curve (in radians).

.5 cm long, .05% concentration ruby.

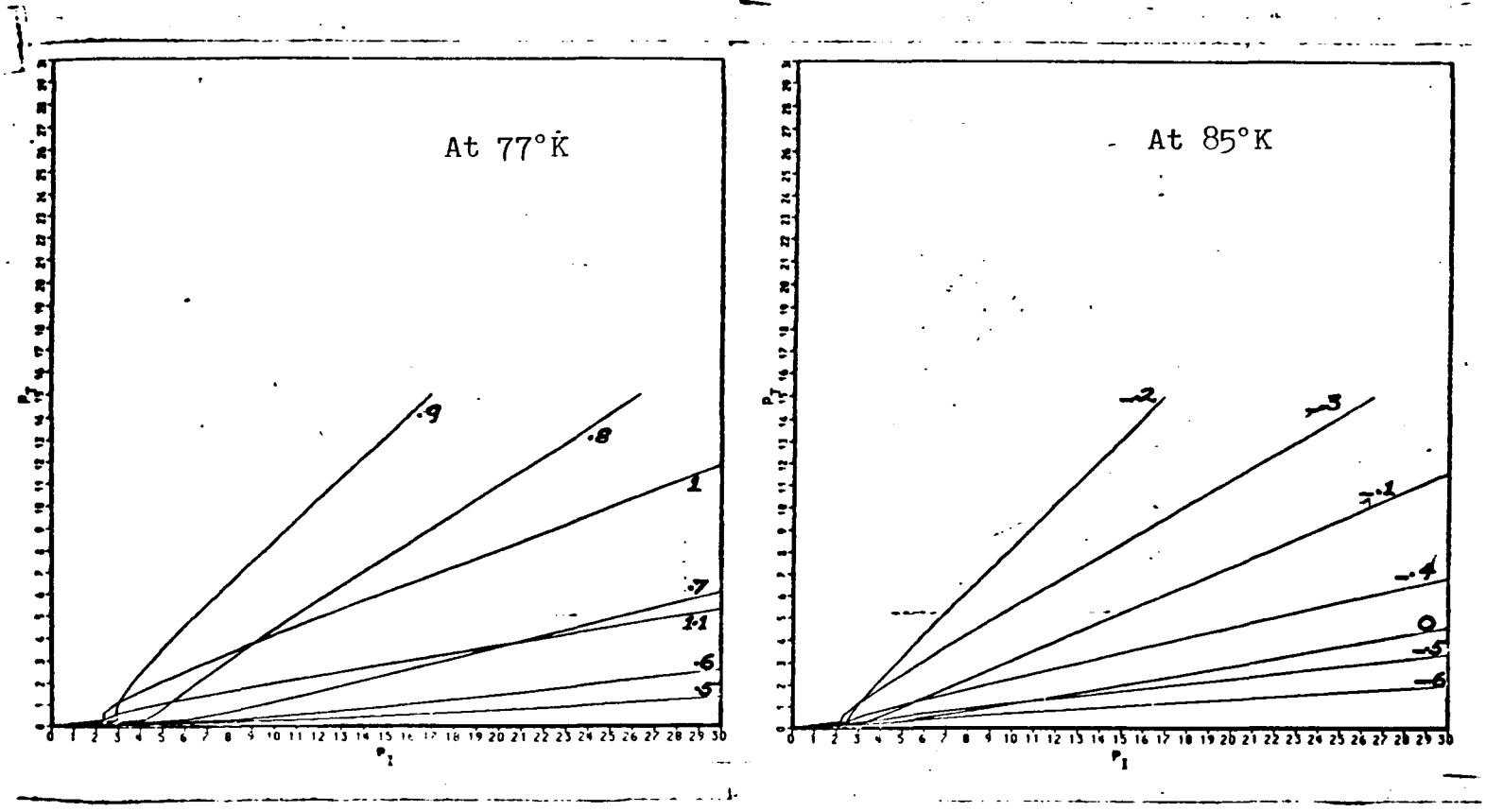

Figure 45

Computer plot of the characteristic curves using Eq.2.3 and the data from table 1 and 2. The mistuning angle (in radians) is indicated for each curve.

.5 cm long, .05% concentration ruby

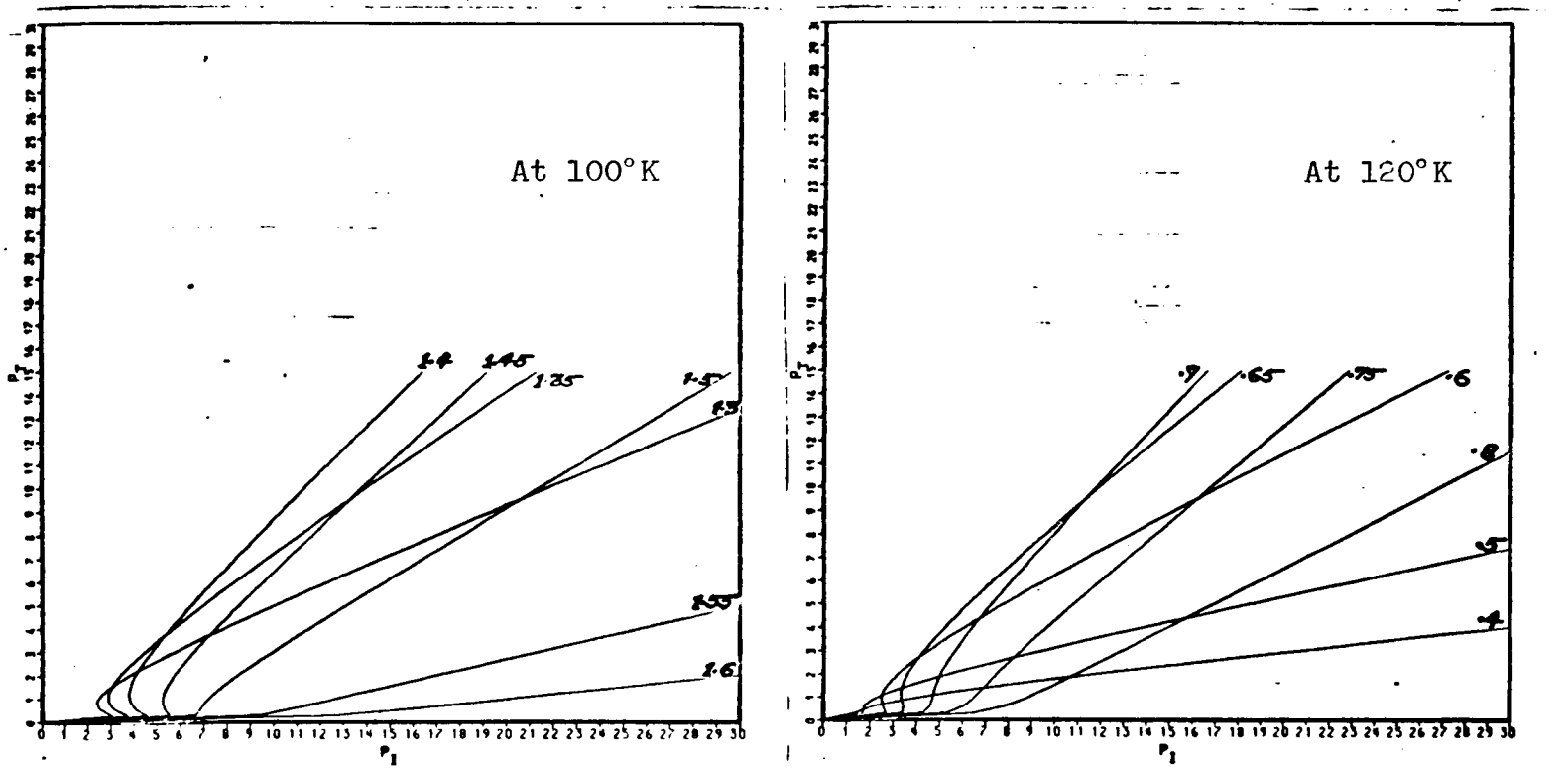

Figure 46

Computer plot of the characteristic curves using Eq.2.3 and the data from tables 1 and 2. The mistuning angle (in radians) is indicated for each curve.

.5 cm long, .05% concentration ruby.

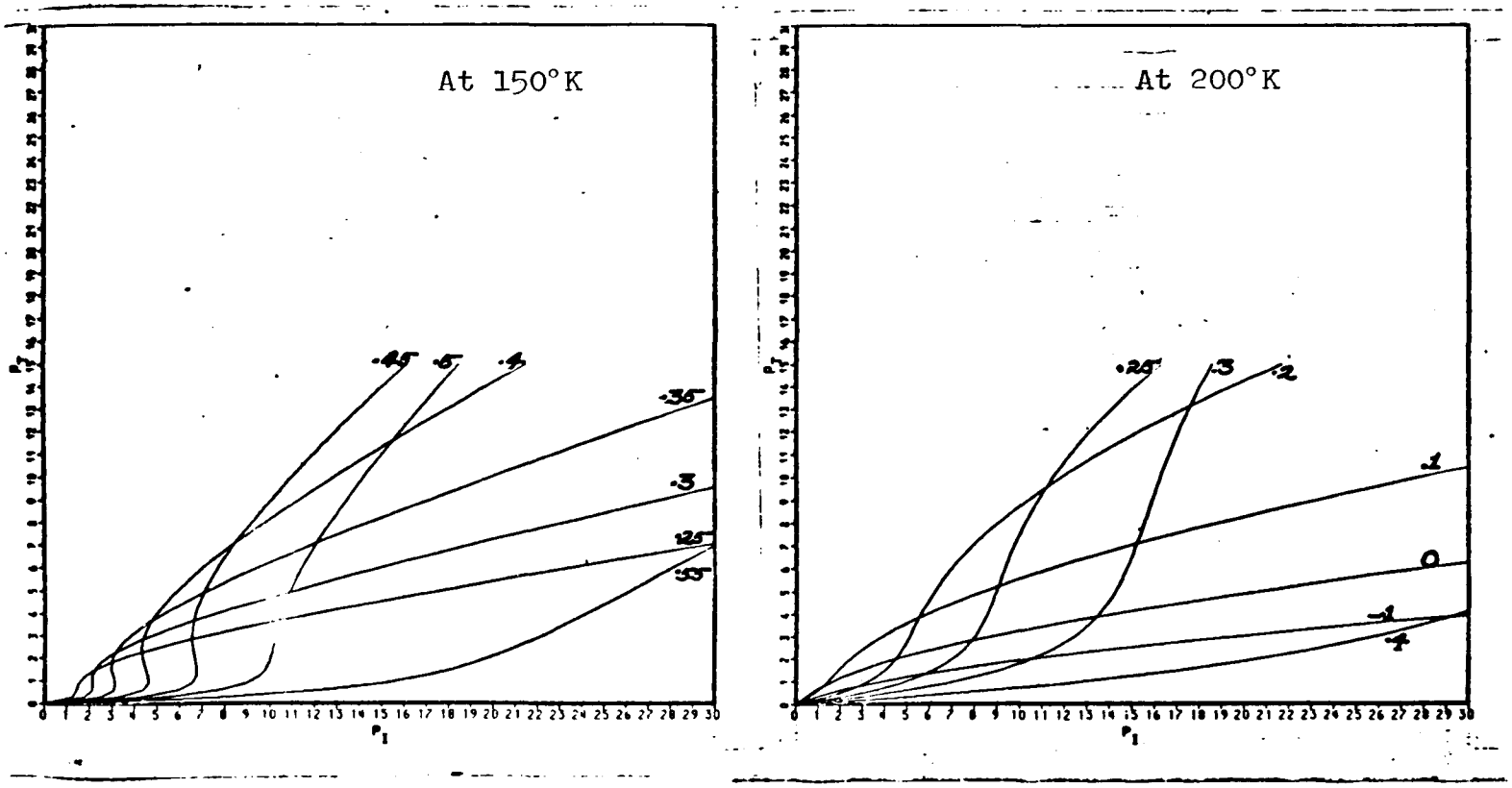

Figure 47

Computer plots of the characteristic curves using Eq.2.3 and the data from tables 1 and 2. The mistuning angle (in radians) is indicated for each curve.

.5 cm long, .05% concentration ruby.

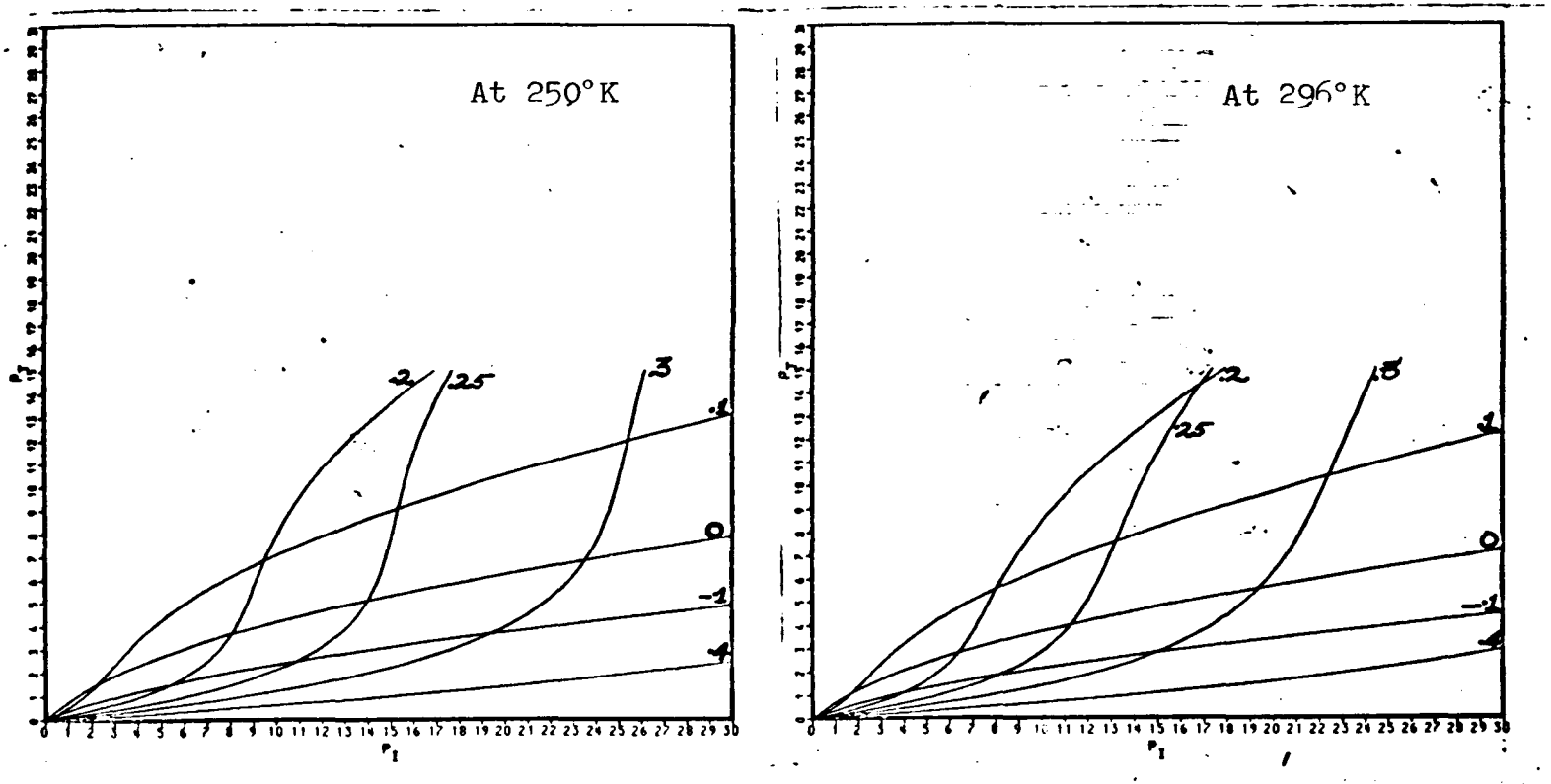

Figure 48

Computer plots of the characteristic curves using Eq.2.3 and the data from table 1 and 2.

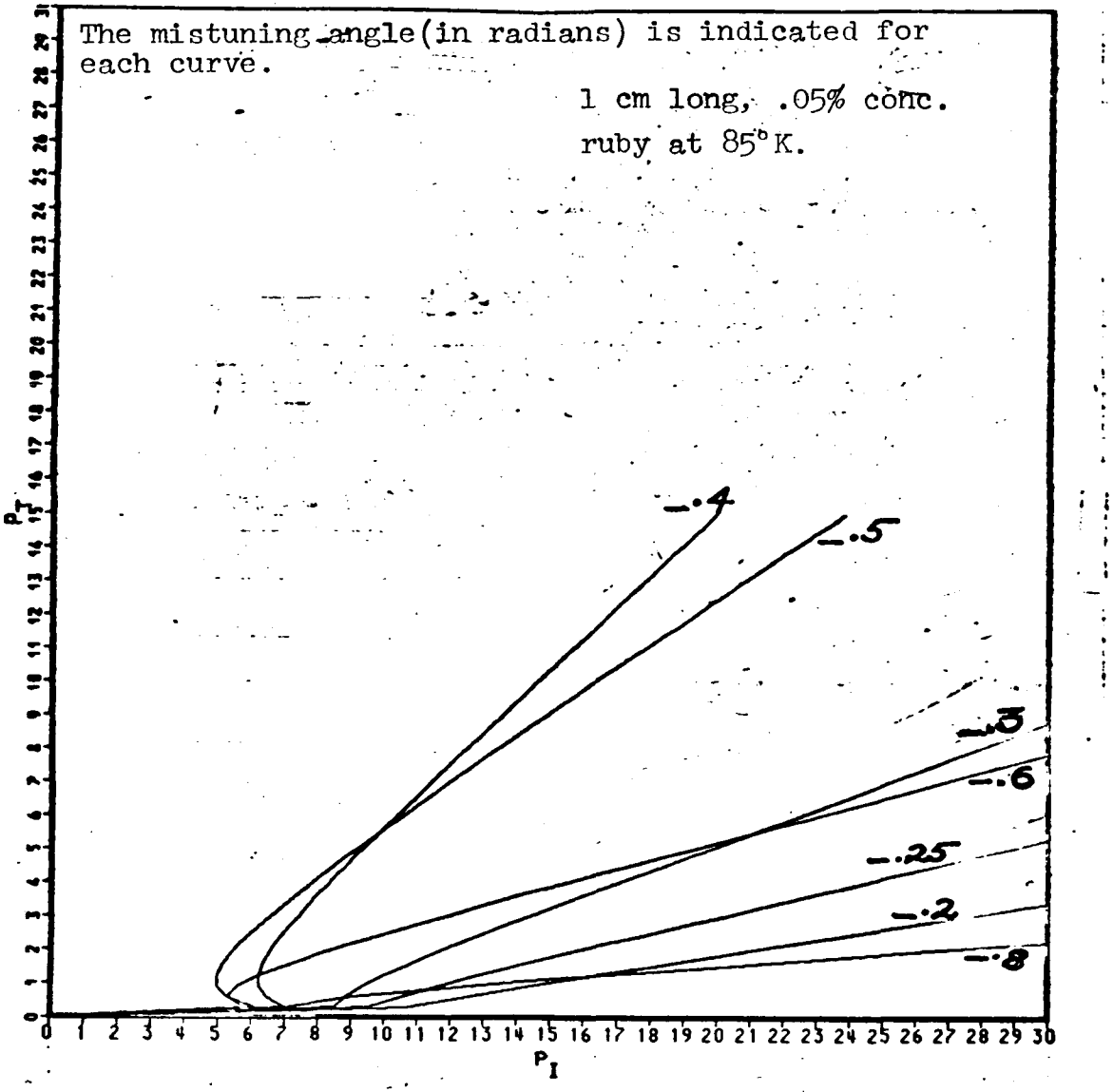

Figure 49

Computer plots of the characteristic curves using Eq.2.3 and the data from tables 1 and 2. The mistuning angle (in radians) is indicated for each curve.

1 cm long, .05%-concentration ruby

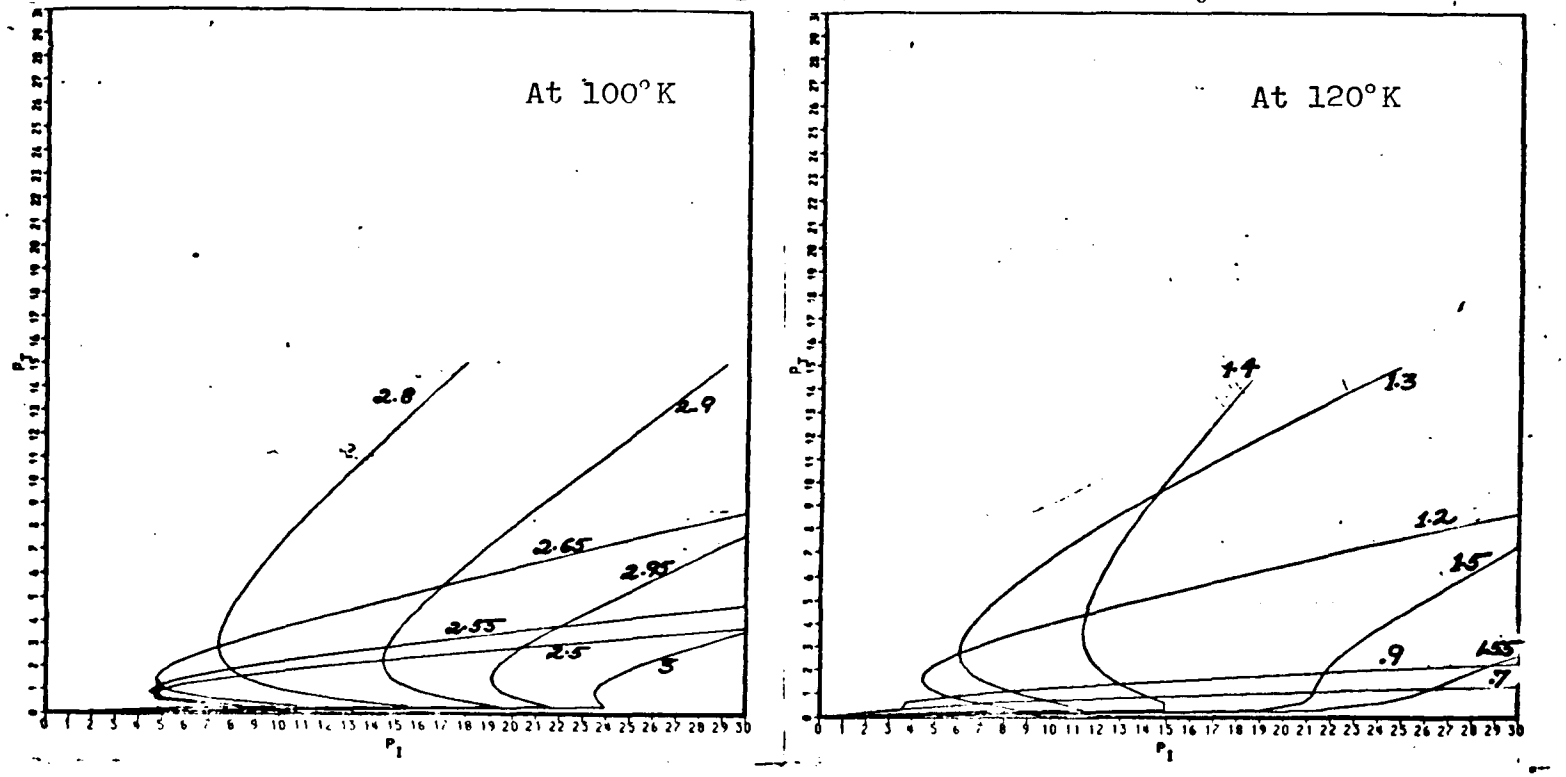

Figure 50

Computer plots of the characteristic curves using Eq.2.3 and the data from tables 1 and 2. The mistuning angle (in radians) is indicated for each curve.

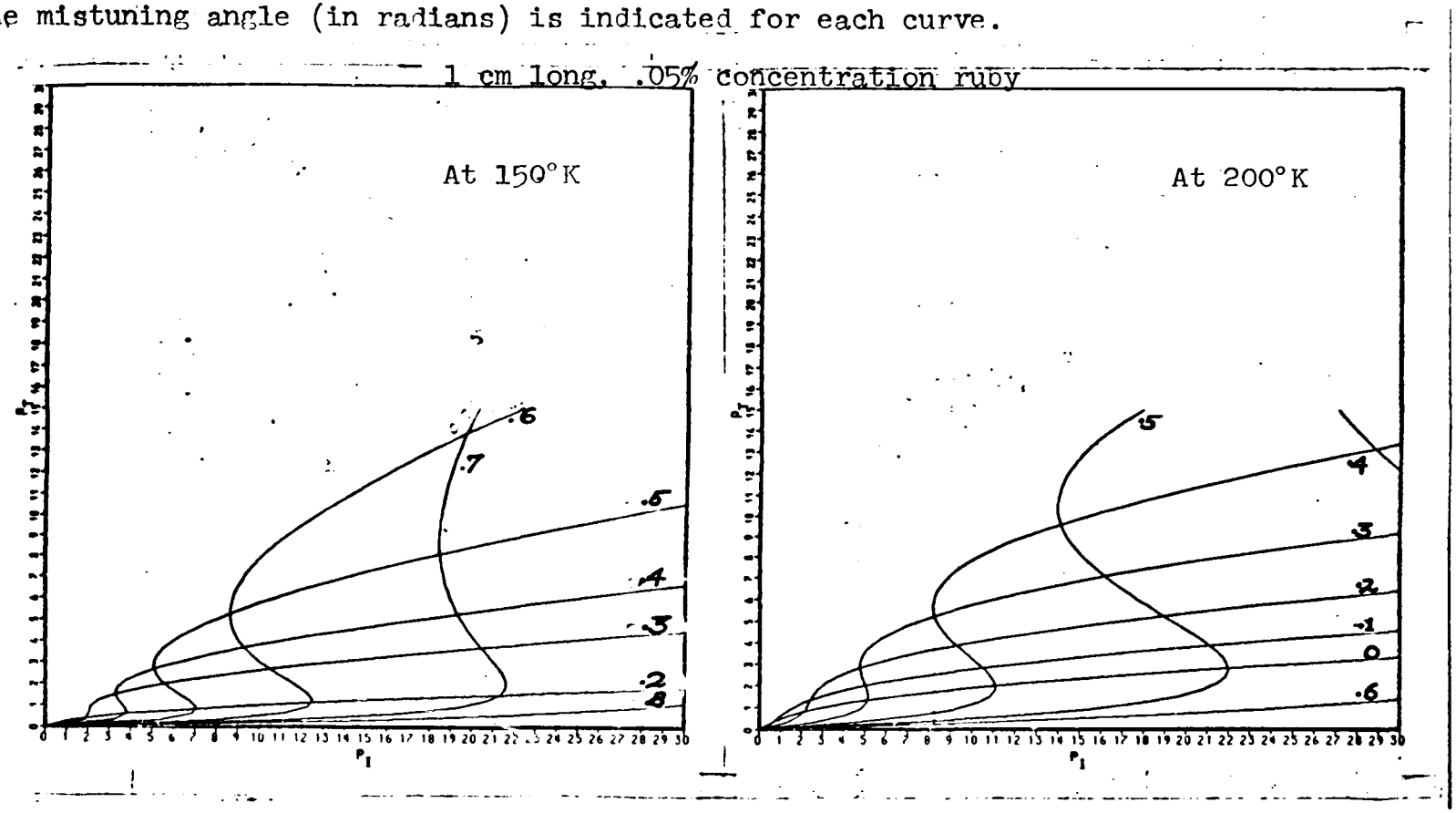

Figure 51

Computer plots of the characteristic curves using Eq.2.3 and the data from tables 1 and 2. The mistuning angle (in radians) is indicated for each curve.

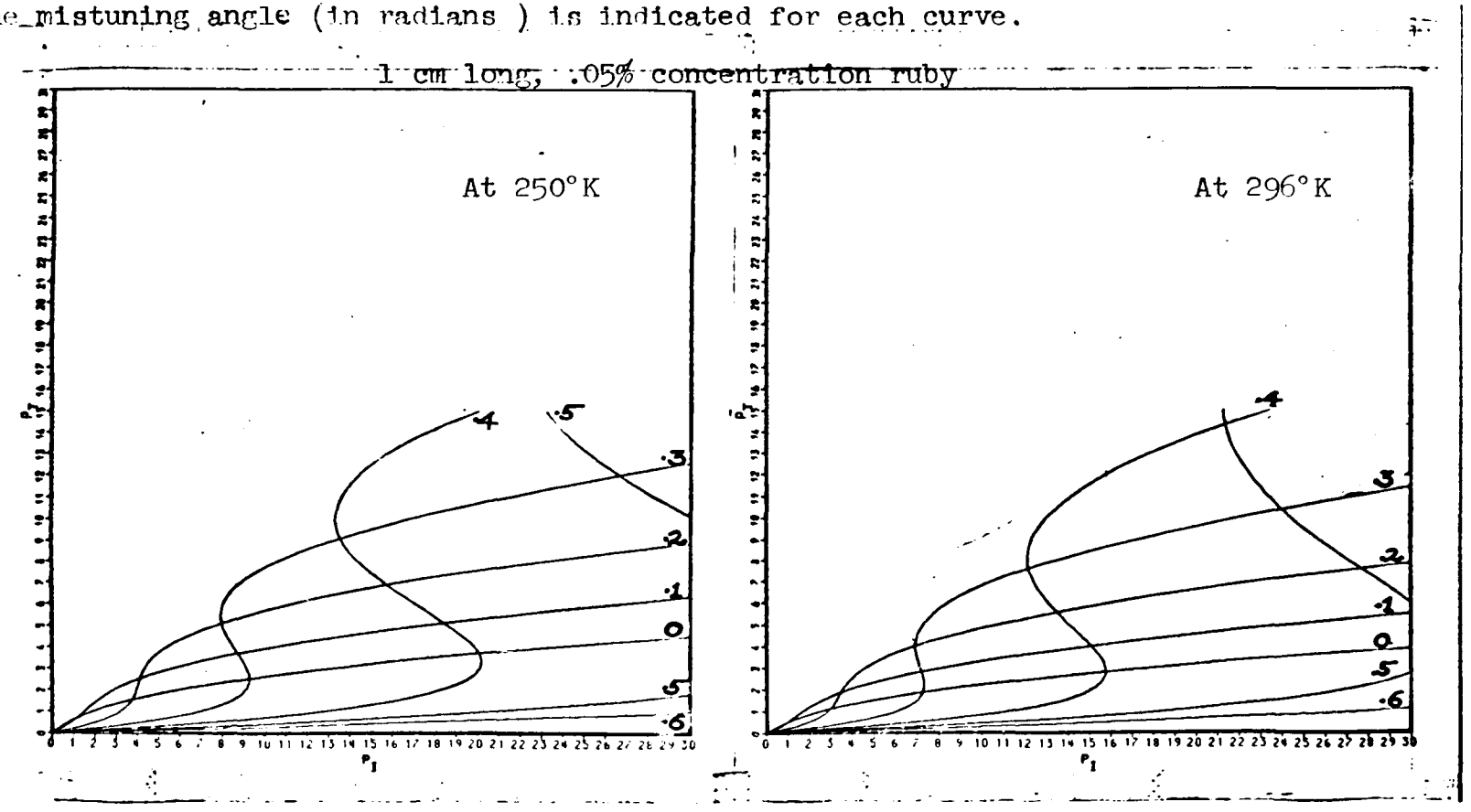

Figure 52

EXPERIMENTAL DATA

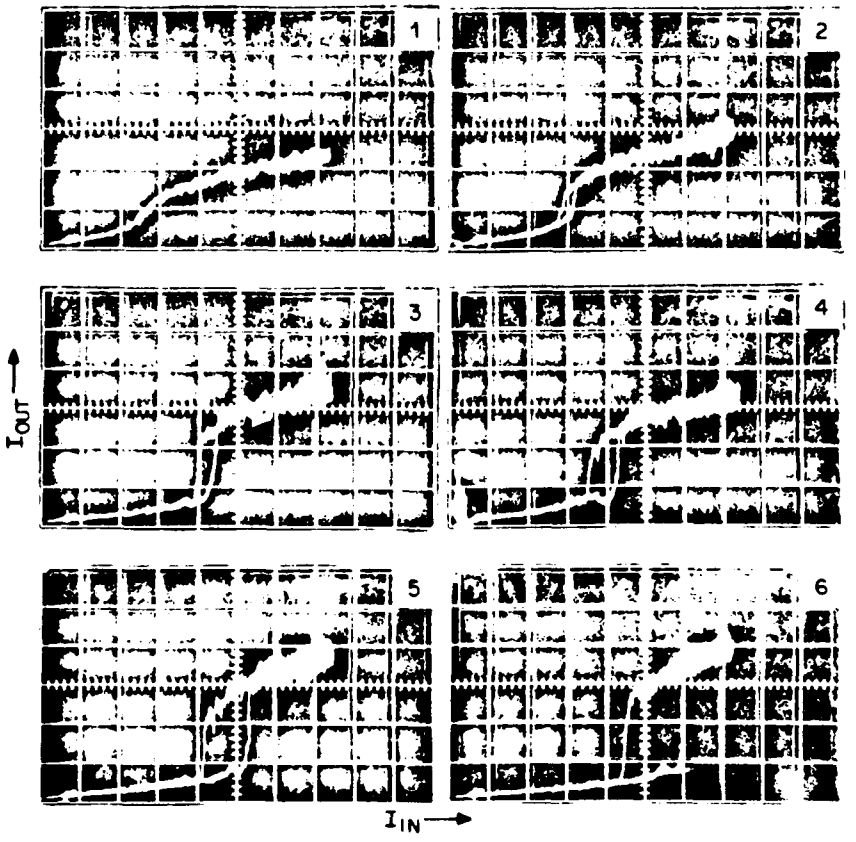

I_{IN} VS I_{OUT} FOR DIFFERENT DETUNING OF THE OT

- 5mm, 60°, 03% Cr^{3+} CONCENTRATION RUBY AT 105°K
- LASER ON LARGEST MODE AT 77°K
- TWO 10cm LENS USED FOR MODE MATCHING
- MAXIMUM TRANSMISSION IN TEM_{00} AT ROOM TEMPERATURE = 25%
- VERTICAL SCALE - 0.4mW/DIV
- HORIZONTAL SCALE - 3.2mW/DIV
- C AXIS AT 45° TO THE LIGHT POLARIZATION
- 0.2 Hz TRIANGULAR SWEEP OF MODULATOR

Figure 53

EXPERIMENTAL DATA

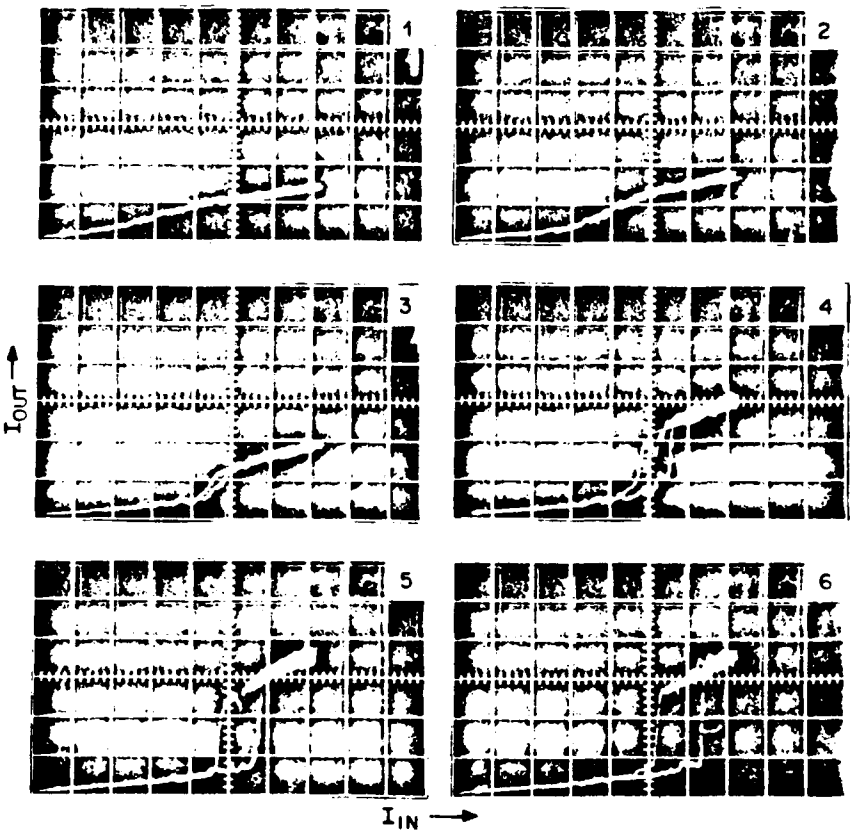

I_{IN} VS I_{OUT} FOR DIFFERENT DETUNING OF THE OT

- 5mm, 60°, .03% Cr CONCENTRATION RUBY AT 105°K
- LASER ON LARGEST MODE AT 77°K
- TWO 10cm LENS USED FOR MODE MATCHING
- MAXIMUM TRANSMISSION IN TEM_{00} AT ROOM TEMPERATURE = 25%
- VERTICAL SCALE - 0.4mW/DIV
- HORIZONTAL SCALE - 3.2mW/DIV
- C AXIS PERPENDICULAR TO THE LIGHT POLARIZATION
- 0.2 Hz TRIANGULAR SWEEP OF MODULATOR

Figure 54

EXPERIMENTAL DATA

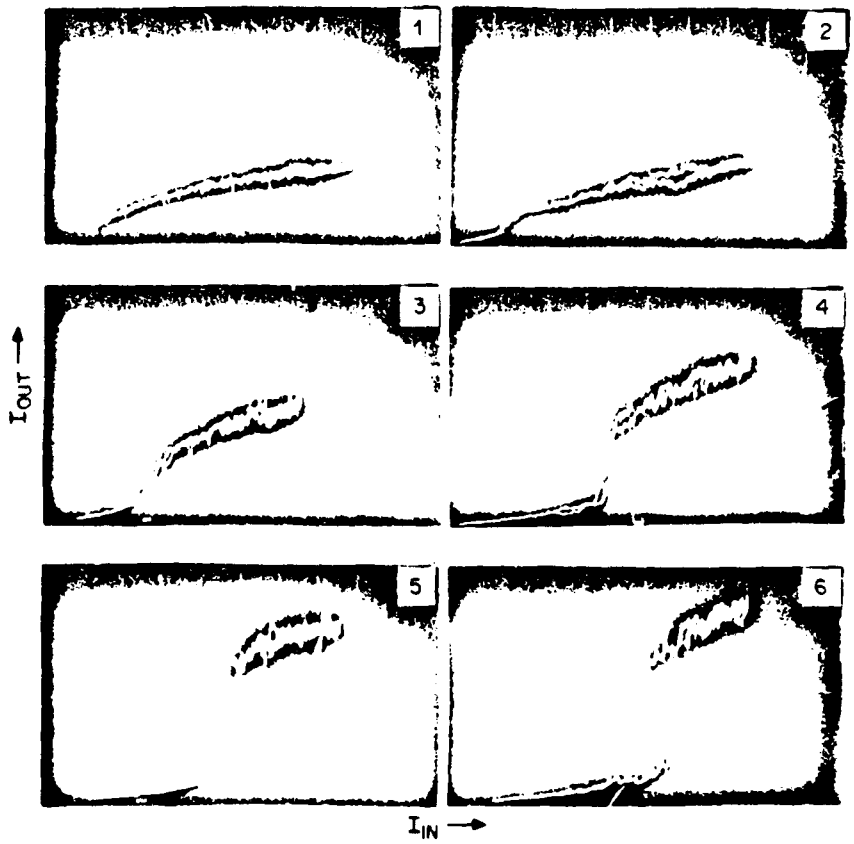

I_{IN} VS I_{OUT} CHARACTERISTIC FOR DIFFERENT DETUNING OF THE OT

- 3mm, 60°, .03% Cr^{3+} CONCENTRATION RUBY AT 95°K
- LASER ON LARGEST MODE AT 65°K
- TWO 10cm LENS USED FOR MODE MATCHING
- MAXIMUM TRANSMISSION IN TEM_{00} AT ROOM TEMPERATURE • 30%
- VERTICAL SCALE -0.38 mW/DIV
- HORIZONTAL SCALE - 3.28mW/DIV
- C AXIS PERPENDICULAR TO THE LIGHT POLARIZATION
- 0.2 Hz TRIANGULAR SWEEP OF MODULATOR

Figure 55

EXPERIMENTAL DATA

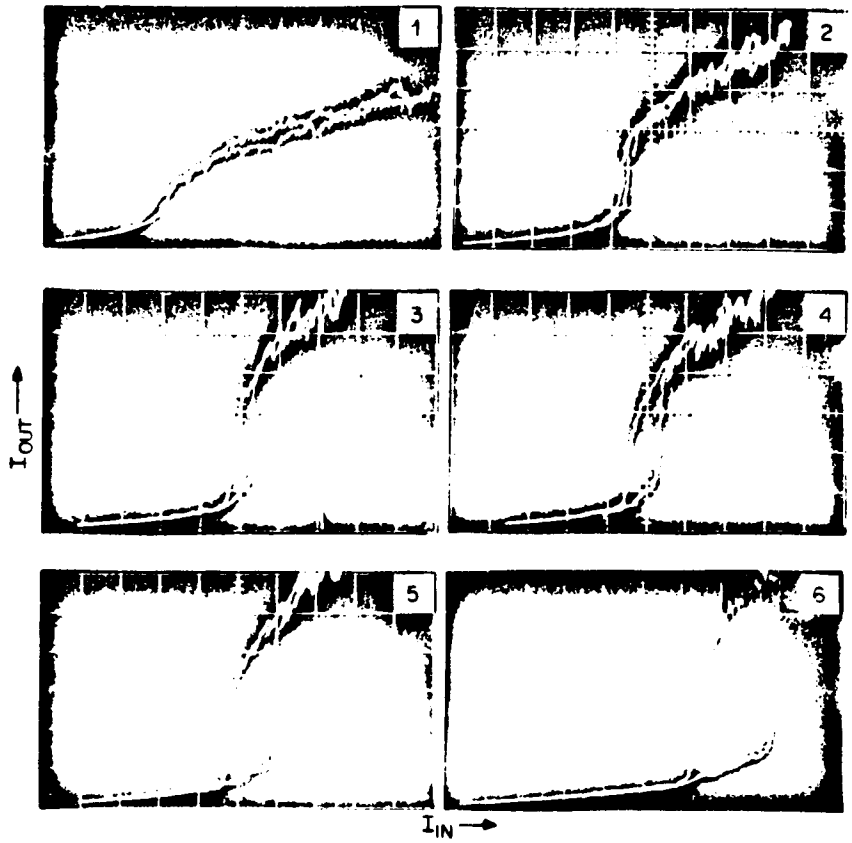

I_{IN} VS I_{OUT} CHARACTERISTIC FOR DIFFERENT DETUNING OF THE OT

- 3mm, 60°, .03% Cr^{3+} CONCENTRATION RUBY AT 95°K
- LASER ON LARGEST MODE AT 65°K
- TWO 10cm LENS USED FOR MODE MATCHING
- MAXIMUM TRANSMISSION IN TEM_{00} AT ROOM TEMPERATURE = 30%
- VERTICAL SCALE - 0.3mW/DIV
- HORIZONTAL SCALE - 2.75mW/DIV
- C AXIS PERPENDICULAR TO THE LIGHT POLARIZATION
- 0.2 Hz TRIANGULAR SWEEP OF MODULATOR
- DATA ON EXPANDED SCALE

Figure 56

EXPERIMENTAL DATA

I_{IN} VS I_{OUT} CHARACTERISTIC FOR DIFFERENT DETUNING OF THE OT

- 3mm, 60°, .03% Cr^{3+} CONCENTRATION RUBY AT 95°K
- LASER ON LARGEST MODE AT 77°K
- TWO 10cm LENS USED FOR MODE MATCHING
- MAXIMUM TRANSMISSION IN TEM_{00} AT ROOM TEMPERATURE = 30%
- VERTICAL SCALE - 0.63mW/DIV
- HORIZONTAL SCALE - 3.85mW/DIV
- C AXIS PERPENDICULAR TO THE LIGHT POLARIZATION
- 0.2 Hz TRIANGULAR SWEEP OF MODULATOR
- EFFECT OF BETTER MODE MATCHING

Figure 57

EXPERIMENTAL DATA

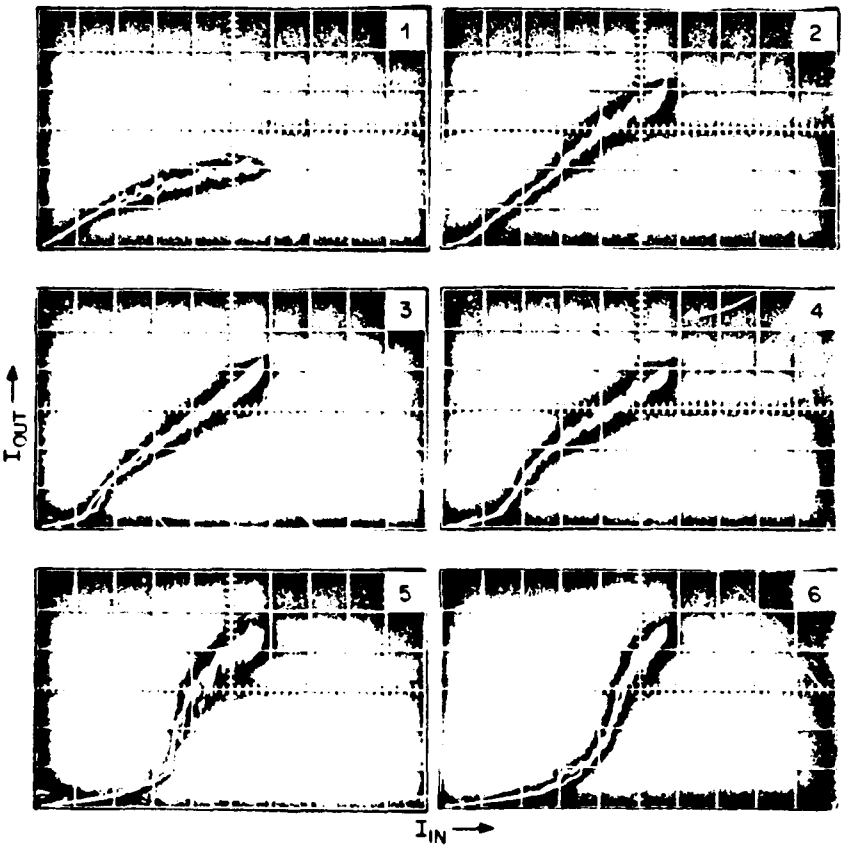

I_{IN} VS I_{OUT} CHARACTERISTIC FOR DIFFERENT DETUNING OF THE OT

- .9mm, 0°, .05% Cr^{3+} CONCENTRATION RUBY AT 85°K
- LASER ON LARGEST MODE AT 77°K
- TWO 10cm LENS USED FOR MODE MATCHING
- MAXIMUM TRANSMISSION IN TEM_{00} AT ROOM TEMPERATURE- 35%
- VERTICAL SCALE- 0.63mW/DIV
- HORIZONTAL SCALE -6mW/DIV
- C AXIS PERPENDICULAR TO THE LIGHT POLARIZATION
- 0.2 Hz TRIANGULAR SWEEP OF MODULATOR

Figure 58

.9 mm, 0°, .05 % CONC RUBY IN CAVITY

LASER AT 77° K

SAMPLE AT 100° K

CAVITY ASYMMETRY HAS SHARP RISE ON THE LEFT

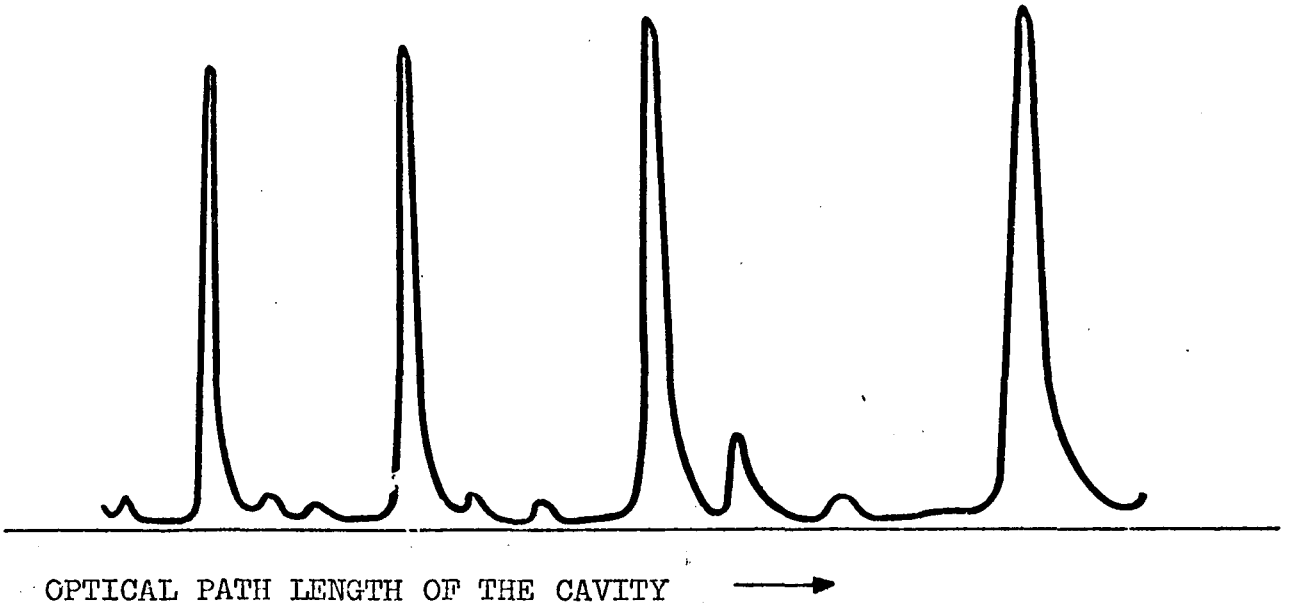

Figure 59

.9 mm, 0°, .05 % CONC RUBY IN CAVITY
LASER AT 77° K
SAMPLE AT 65° K
THE CAVITY ASYMMETRY HAS CHANGED SIGN
SHARP RISE IS ON THE RIGHT

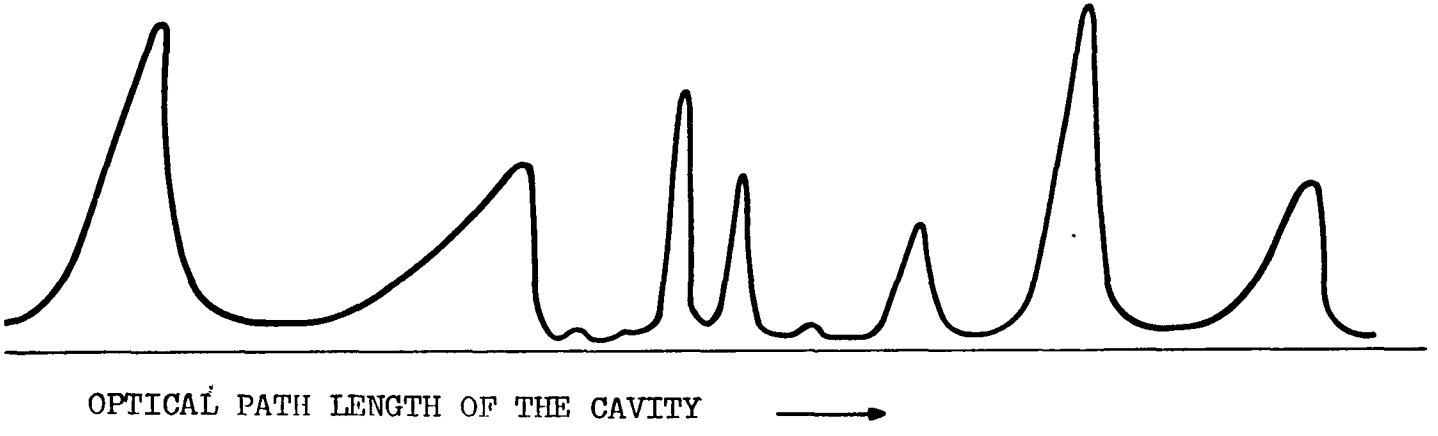

Figure 60

CONCLUSIONS

Bistability and optical amplifier action have been demonstrated in gaseous and doped solid systems. A working theoretical model has been proposed and the theory agrees reasonably with the experimental results. Both experiments indicate the superiority of systems dominated by nonlinear refractive index to those dominated by nonlinear absorption. Nonlinear refractive index enables a wider choice of optical frequencies and lower threshold operation. The experimental results are in good agreement with predicted values. The success of the results in two very different media, gives us confidence in the validity of the model, so that one may project ahead.

The important result of the ruby experiment is the large refractive index produced by the dispersive tails of strong nonresonant bands. This refractive index is made nonlinear by a resonant mechanism which changes the ground state population. If one looks at the absorption spectra of solids like GaAs, InP and so on, there are strong, wide absorption bands (typically $\alpha \sim 10^3$ cm^{-1}). There are also sharp resonances due to excitons or impurity levels in the bandgap region. If one excites these sharp resonances on their wings, one not only gets the nonlinear phase associated with the sharp resonance but also the contribution from the nonresonant bands.

How small could the device be made? In principle the volume of the device could be of the order of λ^3. To

achieve this, the medium should have α of the order of λ^{-1} and since $\alpha L \sim 1$, $L = \lambda$. Further, the beam should be focussed to a spot of area λ^2 for minimum diffractive loss (i.e., F number = area/λL = 1).

Let us now study the fundamental limitations of the device. If the absorption cross section σ is about λ^2, since $\alpha = N\sigma$ this implies one active atom per device. To guard against statistical glitches one needs at least say, a thousand active atoms and we can choose σ to be a thousand times less, perhaps by being off resonance and increasing the number of active atoms by a thousand. The power needed to operate such a device is that of a thousand photons/lifetime which is 10^{-16} joules/lifetime. This is comparable to the energy required in competitive devices like the charge coupled device. A nanosec. speed device, would need a laser power of 100 nW or more. The power of 10^{-16} joules per lifetime is the minimum power possible. The energy of a photon of the order of an eV and the statistical requirement of at least a 1000 photons may be the ultimate limitations [41] of these optical bistable devices.

Figure 61 is a possible use of the device in a repeater station where a single laser and many such devices are used to process several channels. The device may open up a new dimension in signal processing, but even if it doesn't, these experiments have shown that it is possible to construct devices where an optical beam could be controlled by a weaker beam.

A FICTITIOUS OPTICAL COMMUNICATION REPEATER USING OT

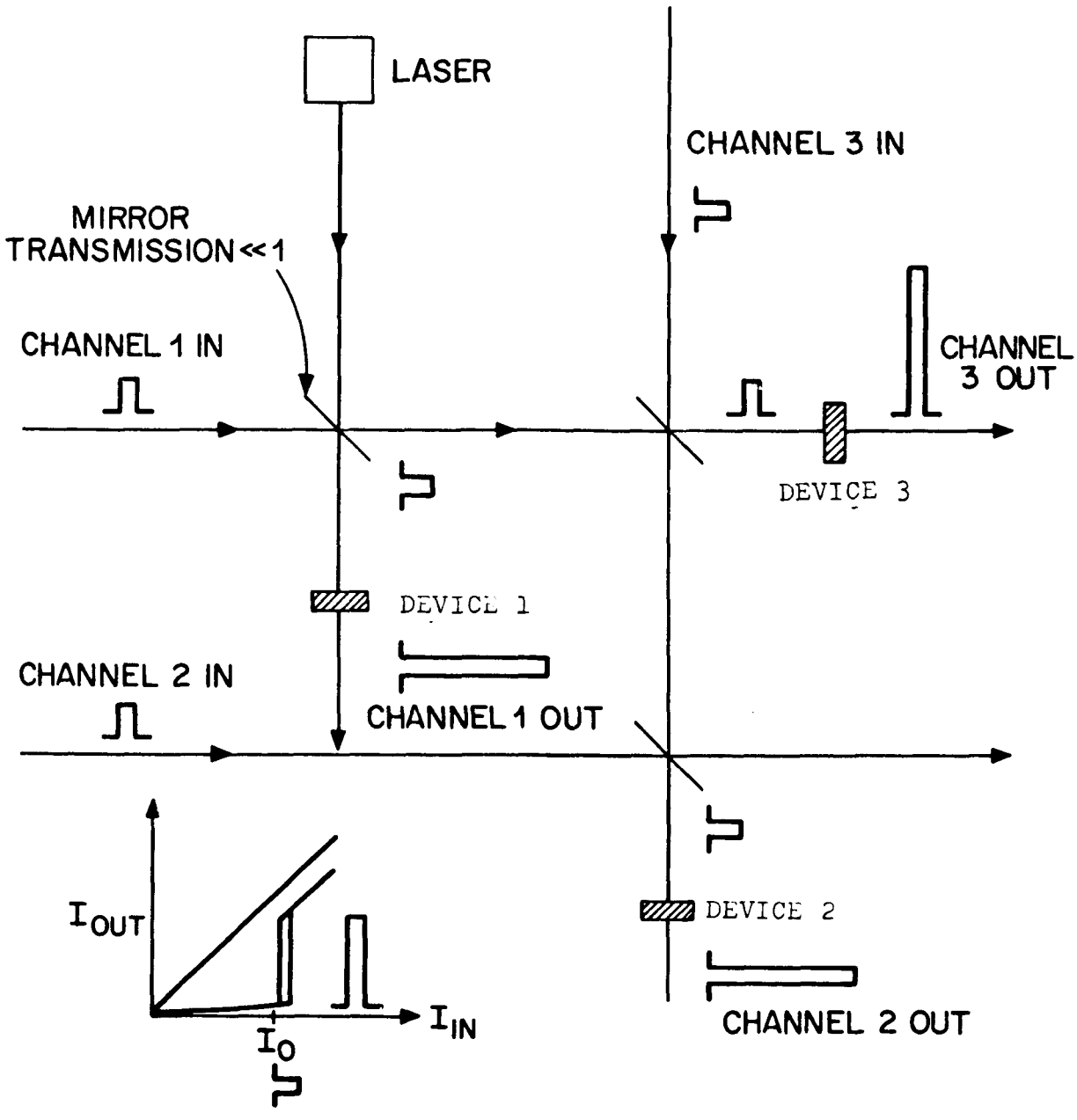

Figure 61

APPENDIX A

STABILITY OF THE SOLUTIONS

Equation 2.3 contains the essential information describing the device. For the moment it will suffice to assume that the device works purely on nonlinear absorption due to a two level Bloch system. Then in the absorptive case:

$$\varepsilon_I = \varepsilon_T + \Gamma v \ , \qquad \text{A.1}$$

where v is in units of $8\pi^2 L/\lambda n_0$. For further simplicity assume the laser to be exactly on resonance with the absorber so that $\Delta\omega = 0$. The fields may be chosen to be real without loss of generality. Using the Bloch equations 3.7a, b and c and A.1 we get

$$\dot{\varepsilon}_T = \dot{\varepsilon}_I + \Gamma W \kappa \varepsilon_I + \frac{1}{T_2'} (\varepsilon_I - \varepsilon_T) \ , \qquad \text{A.2}$$

and

$$W = -1 + \kappa \Gamma^{-1} \int_{-\infty}^{t} (\varepsilon_I - \varepsilon_T) \varepsilon_T e^{-(t-\tau)/T_1} \, d\tau \ . \qquad \text{A.3}$$

On substituting into A.2 we get

$$\dot{\varepsilon}_T = -\left(\frac{1}{T_2'} + \Gamma\kappa \right) \varepsilon_T + \frac{\varepsilon_I}{T_2'} + \varepsilon_I + \kappa^2 \varepsilon_T \int_{-\infty}^{t} (\varepsilon_I - \varepsilon_T) \varepsilon_T e^{-(t-\tau)/T_1} \, d\tau \ . \qquad \text{A.4}$$

This equation describes the time evolution of the transmitted field in a complicated way. At steady state, $\dot{\varepsilon}_T = \dot{\varepsilon}_I = 0$ and we get,

$$\varepsilon_I = \varepsilon_T \left(1 + \frac{\Gamma}{1 + \kappa^2 T_1 T_2' \varepsilon_T^2}\right). \qquad \text{A.5}$$

This equation gives the stationary points and has 1 or 3 solutions $\varepsilon_T = \varepsilon_T(\varepsilon_I)$. Figure 62 gives the general appearance of the curve described by A.5 and it is easy to see that for certain given input fields and values of Γ there are more than one steady state solution. Let us study the nature of the solutions at one of the output fields ε_0. Linearize the equation around ε_0, and let $x = \varepsilon_T - \varepsilon_0$, then

$$\dot{x} = -\left(\frac{1}{T_2'} + \Gamma\kappa\right)x - \left(\frac{1}{T_2'} + \Gamma\kappa\right)\varepsilon_0 + \varepsilon_I/T_2'$$

$$+ \kappa^2(\varepsilon_0+x)\int_{-\infty}^{t} d\tau e^{-(t-\tau)/T_1}(\varepsilon_0+x)(\varepsilon_I-\varepsilon_0-x) \; .$$

A.6

Dropping nonlinear terms in the limit of small values of x we get,

$$\dot{x} = A_1 x + A^2 \int_{-\infty}^{t} d\tau e^{-(t-\tau)/T_1} x(\tau), \quad \text{which} \qquad \text{A.7}$$

$$= A_1 x + A_2 I \quad , \qquad \text{where} \qquad \text{A.8}$$

$$A_1 = -\,(1/T_2' + \kappa\Gamma) + T_1\kappa^2\varepsilon_0(\varepsilon_I-\varepsilon_0)\ , \qquad \text{A.9}$$

$$A_2 = \kappa^2\varepsilon_0(\varepsilon_I-2\varepsilon_0) \quad \text{and} \quad I = \int_{-\infty}^{t} x(\tau)e^{-(t-\tau)/T_1}\,d\tau \qquad \text{A.10}$$

We could write the same as

$$\frac{d}{dt}\begin{pmatrix} x \\ I \end{pmatrix} = \begin{pmatrix} A_1 & A_2 \\ 1 & -\frac{1}{T_1} \end{pmatrix}\begin{pmatrix} x \\ I \end{pmatrix} . \qquad \text{A.11}$$

The time evolution of x is easily guessed as

$$x(t) \sim x(0)e^{\lambda t}\ , \qquad \text{A.12}$$

where λ is the eigenvalue of the matrix. If $\mathrm{Re}\lambda$ is positive, the solution is unstable, if $\mathrm{Re}\lambda$ is negative, we have a stable solution.

The eigenvalues of λ are given by

$$\lambda = \tfrac{1}{2}[(A_1-1/T_1) \pm \{(A_1-1/T_1)^2 + 4(A_1/T_1+A_2)\}^{\frac{1}{2}}]. \qquad \text{A.13}$$

Since λ is never purely imaginary, there are no purely oscillatory solutions. The necessary and sufficient condition that λ is negative definite is

$$T_1 A_1 - 1 < 0, \qquad \text{A.14}$$

and

$$A_1 + A_2 T_1 < 0 \quad . \qquad \text{A.15}$$

From Eq. A.5 we get

$$T_1 A_1 - 1 = - \frac{T_1 (\Gamma + 1/T_2' + 1/T_1)}{1 + \kappa^2 T_1 T_2' \varepsilon_T^2} \quad , \qquad \text{A.16}$$

which is always negative. Further manipulation of Eq. A.5 gives us

$$A_1 + A_2 T_1 = - T_1 (1 + \kappa^2 T_1 T_2') \frac{\partial \varepsilon_I}{\partial \varepsilon_T} \quad . \qquad \text{A.17}$$

Hence the solutions are stable if and only if

$$\frac{\partial \varepsilon_I}{\partial \varepsilon_T} > 0 \ , \qquad \text{A.18}$$

when evaluated at the steady-state solution values. Referring to Fig. 62 we see that there is a region of unstable points on the curve in the shaded region and hence as soon as the value of ε_I reaches the value ε_{IU} output switches from 1 to 2 and when ε_I research the value ε_{ID}, the output switches down from 3 to 4.

Clearly the requirement for bistability is that there exist two values of ε_T for a given ε_I where, $\frac{\partial \varepsilon_I}{\partial \varepsilon_T} > 0$. This implies that

$$1 + \frac{\Gamma(1-F^2)}{(1+F^2)^2} > 0, \qquad \text{A.19}$$

where $F^2 = \kappa^2 T_1 T_2' \varepsilon_T^2$. The bistable points correspond to

$$F^2 = \frac{(\Gamma-2) \pm \sqrt{\Gamma(\Gamma-8)}}{2}, \qquad \text{A.20}$$

Since F^2, proportional to intensity of light is real quantity, a necessary and sufficient condition for bistability is that $\Gamma > 8$. At the points $\frac{\partial \varepsilon_I}{\partial \varepsilon_T} = 0$, we get 2 values of λ, one negative and the other identically zero. At these points the solutions are stable for negative (positive) perturbation at the switch up (switch down) value of the field and unstable for positive (negative) perturbation.

The above conclusion is not very general. For instance, it can be shown that if there are more than one relaxation time in the medium the points with $\frac{\partial \varepsilon_I}{\partial \varepsilon_T} > 0$ need not necessarily be stable[42].

STABILITY OF SOLUTIONS FOR
ABSORPTIVE BISTABILITY

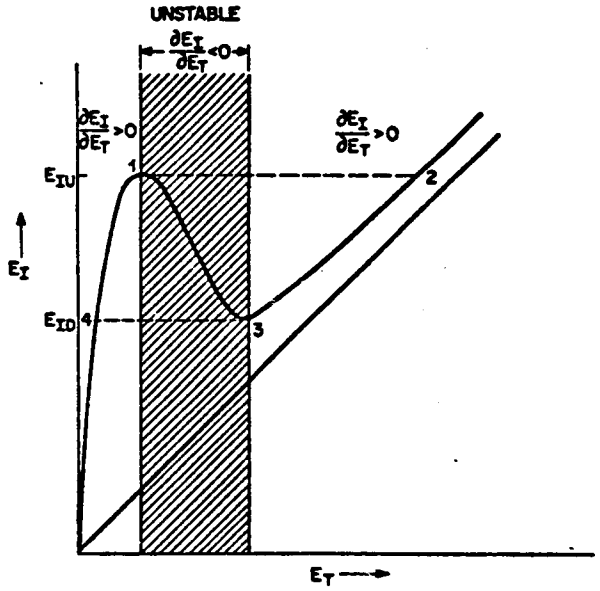

Figure 62

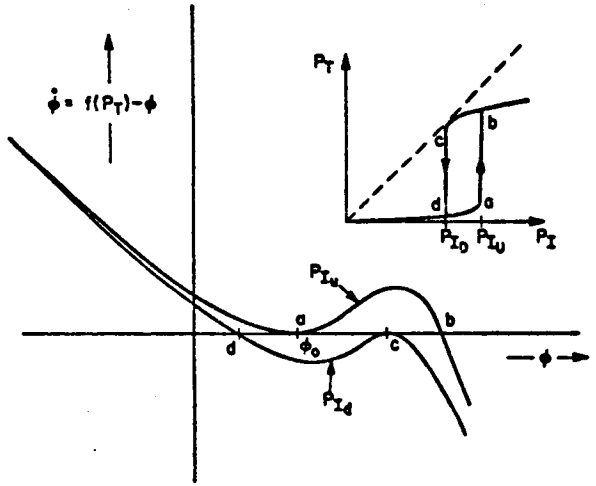

FIGURE 63

APPENDIX B

RESPONSE OF THE DEVICE AT A SWITCHING POINT

We will study the response of a dispersive, bistable device at the switch-on point for a small, linear increase in the input power. Referring to Fig. 63 and Eq. 2.5, we can see that $\dot{\phi}$ or $F(\phi,P_I)$ (refer to Eq. 2.7) as a function of ϕ will have the general form as shown in the figure. The switch-on points are defined by P_{Iu}, and ϕ_o which are the roots of the equations,

$$F(\phi,P_I)\Big|_{\phi_o,P_{Iu}} = 0 \qquad \text{B.1}$$

and

$$\frac{\partial F}{\partial \phi}(\phi,P_I)\Big|_{\phi_o,P_{Iu}} = 0. \qquad \text{B.2}$$

Hence, close to ϕ_o and P_{Iu},

$$F(\phi,P_I) = F(\phi_o,P_{Iu}) + \frac{\partial F}{\partial \phi}\Big|_o \Delta\phi + \frac{\partial F}{\partial P_I}\Big|_o \Delta P_I + \frac{1}{2}\frac{\partial^2 F}{\partial \phi^2}\Big|_o \Delta\phi^2 + \frac{\partial^2 F}{\partial\phi\partial P_I}\Big|_o \Delta\phi\Delta P_I + \ldots \qquad \text{B.3}$$

where the subscript o refers to evaluation of the function at $P_I = P_{Iu}$ and $\phi = \phi_o$. Using B.1, B.2 and Eq. 2.7, we obtain,

$$\Delta\dot{\phi} = \frac{\partial F}{\partial P_I}\Big|_o \Delta P_I + \frac{1}{2}\frac{\partial^2 F}{\partial \phi^2}\Big|_o \Delta\phi^2 + \frac{\partial^2 F}{\partial\phi\partial P_I}\Big|_o \Delta\phi\Delta P_I + \frac{1}{2}\frac{\partial^2 F}{\partial P_I^2}\Big|_o \Delta P_I^2 + \ldots$$

If we consider P_I = at where a is very small, then dropping terms containing the second and higher powers of a, we get

$$\dot{\Delta\phi} = \alpha a t + \beta \Delta\phi^2 + \gamma a \Delta\phi t \qquad \text{B.5}$$

where

$$\alpha = \left.\frac{\partial F}{\partial P_I}\right|_o, \quad \beta = \frac{1}{2}\left.\frac{\partial^2 F}{\partial \phi^2}\right|_o \text{ and } \gamma = \left.\frac{\partial^2 F}{\partial \phi \partial P_I}\right|_o .$$

We will deal with cases where $\alpha > 0$. Defining new variables

$$\xi = \left(\frac{\beta^2}{\alpha a}\right)^{1/3} \Delta\phi \quad \text{and} \quad \tau = (\alpha a \beta)^{1/3} t,$$

equation B.5 reduces to

$$\xi' = \tau + \xi^2 + \varepsilon \xi \tau \qquad \text{B.6}$$

where the prime denotes differentiation with respect to τ and

$$\varepsilon = \left(\frac{\gamma^3 a}{\alpha^2 \beta^2}\right)^{1/3} .$$

If P_I is changed from P_{Iu} very slowly (i.e., small a) the third term could be dropped. Eq. B.6 reduces to

$$\xi' = \xi^2 + \tau \qquad \text{B.7}$$

and defining

$$Y = e^{-\int_{-\infty}^{\tau} \xi d\tau'} \qquad \text{B.8}$$

we get

$$\ddot{Y} + Y\tau = 0 \qquad \text{B.9}$$

and

$$\xi = -\frac{d}{d\tau} \ln Y. \qquad \text{B.10}$$

The solution of the equation B.12 is made up of the Airy functions[17] and the general solution is

$$= AA_i(-\tau) + BB_i(-\tau) \qquad \text{B.11}$$

where A and B are constants, to be calculated from boundary conditions. From Eq. B.7 it is easy to see that as $\tau \to -\infty$, $\xi \to -\sqrt{\tau}$. Of the functions A_i and B_i, only A_i has the correct asymptotic form to satisfy this condition. Hence,

$$\xi = -\frac{d}{d\tau} \ln A_i(-\tau) \qquad \text{B.12}$$

or

$$\Delta\phi(t) = -\left(\frac{\alpha a}{\beta^2}\right)^{1/3} \frac{d}{dt} \ln A_i\,[-(\alpha a\beta)^{1/3} t]. \qquad \text{B.13}$$

From Eq. 2.7, the change in the transmitted power can be calculated.

If the third term in Eq. B.6 was not neglected one can again solve the problem exactly. On making the substitution

$$Y = e^{-\int_{-\infty}^{\tau} \xi d\tau'}$$

in Eq. B.7 we get

$$Y'' + \tau Y - \varepsilon Y''\tau = 0. \qquad \text{B.14}$$

Writing $Y = Xe^{1/4\ \varepsilon\tau^2}$ one gets

$$X'' - 1/4\{\varepsilon^2\tau^2 - 4\tau - 2\varepsilon\}X = 0. \qquad \text{B.15}$$

If we define $\bar{\tau} = \sqrt{\varepsilon}(\tau - 2/\varepsilon)$ and $q = (4/\varepsilon^2 + 2)$ then Eq. B.15 could be rewritten as

$$X'' - 1/4\{\bar{\tau}^2 - q\}X = 0. \qquad \text{B.16}$$

The solution to this equation is

$$X = uU(-q,\bar{\tau}) + vV(-q,\bar{\tau}) \qquad \text{B.17}$$

where u and v are constants and U and V are the Parabolic Cylindrical functions. To determine u and v let us consider the limit of $\tau \to -\infty$. From Eq. B.6 we obtain $\xi \to -\frac{1}{\varepsilon}$. Only $U(-q,\bar{\tau})$ has the correct asymptotic form. Hence,

$$\Delta\phi(t) = -\left[\frac{\alpha a}{\beta^2}\right]^{1/3} \frac{d}{dt} \ln \left\{ e^{1/4\ \varepsilon\tau^2}\ U\left[-q, \sqrt{\varepsilon}\left[\tau - \frac{2}{\varepsilon}\right]\right]\right\} \qquad \text{B.20}$$

APPENDIX C

THE GAIN FUNCTION FOR A TWO LEVEL SYSTEM DEVICE

From Chapter 2

$$E_I = E_T - i \frac{R}{T} \varphi (E_T) E_T \ . \qquad C.1$$

If at a steady state value E_I^0, E_T^0 the input is modulated (pure amplitude),

$$\Delta E_I = \Delta E_T (1 - i \frac{R}{T} \varphi(E_T)) - i \frac{R}{T} E_T \Delta\varphi \ . \qquad C.2$$

For a change in E_T, $\Delta\varphi$ could be calculated from Chapter 3, Eqs. 3.26 and 3.28 which yield

$$\Delta\varphi_R = \frac{4\pi L}{\lambda} \Delta n_R ,$$

$$= - \mathrm{Re} \left(\frac{4\pi L}{\lambda}\right) G_R(\Delta\omega, \nu) \kappa T_2' \frac{\Delta E_T}{E_T^0} e^{i\nu t} \ , \qquad C.3$$

where G_R is given by Eq. 3.26. Similarly,

$$\Delta\varphi_I = - \mathrm{Re} \left(\frac{4\pi L}{\lambda}\right) G_I(\Delta\omega, \nu) \kappa T_2' \frac{\Delta E_T}{E_T^0} e^{i\nu t} \ . \qquad C.4$$

A word of caution to the reader. The phase is a function of the cavity field and to an approximation we can replace the cavity field by $E_T/\sqrt{T}$. Hence in Eqs. C.3 and C.4, this factor of $\frac{1}{\sqrt{T}}$ must be appropriately added. This is still an approximation and it has been shown by

Bonifacio and Lugiato[10] that the factor $\frac{1}{\sqrt{T}}$ must be replaced by $\sqrt{\frac{3}{T}}$ using a mean field approximation method. Substituting these values we can get the matrix elements of the gain matrix, which are

$$G^{RR} = G^{II} \left(1 + \frac{R}{T}\varphi_I^0 + E_T^0 \frac{R}{T} \frac{\Delta\varphi}{\Delta E_T^I}\right)$$

$$= \frac{}{\left[\left(1 + \frac{R}{T}\varphi_I^0 + E_T^0 \frac{\Delta\varphi_I}{\Delta E_T}\right)^2 + \frac{R_2}{T^2}\left(\varphi_R^0 + E_T^0 \frac{\Delta\varphi^R}{\Delta E_T}\right)^2\right]} , \qquad \text{C.5}$$

$$G^{RI} = -G^{IR} \; R/T \left(\varphi^{Re} + E_T^0 \frac{\Delta\varphi^R}{\Delta E_T}\right)$$

$$= \frac{}{\left[\left(1 + R/T\,\varphi_I^0 + E_T^0 \frac{R}{T} \frac{\Delta\varphi_I}{\Delta E_T}\right)^2 + \frac{R^2}{T^2}\left(\varphi_R^0 + E_T^0 \frac{\Delta\varphi^R}{\Delta E_T}\right)^2\right]} . \qquad \text{C.6}$$

For a device to act as a pure AM-AM converter $G^{RI} = -G^{IR} = 0$. It might be possible to make AM-FM and FM-AM devices too.

APPENDIX D

To simplify the equations we could write them as

$$\frac{\partial}{\partial z}\begin{pmatrix}\varepsilon_F\\ \\ \varepsilon_B\end{pmatrix} = \begin{pmatrix}M_1 & M_2\\ \\ M_3 & -M_1\end{pmatrix}\begin{pmatrix}\varepsilon_F\\ \\ \varepsilon_B\end{pmatrix}, \qquad \text{D.1}$$

where

$$M_1 = \frac{\alpha}{2}\,\sigma(0) \qquad \text{D.2a}$$

$$M_2 = \frac{\alpha}{2}\,\sigma(2k)(\cos\,\Delta\varphi - Y\,\sin\,\Delta\varphi) \qquad \text{D.2b}$$

$$M_3 = -\frac{\alpha}{2}\,\sigma(2k)(\cos\,\Delta\varphi) \qquad \text{D.2c}$$

We could express equation D.1 as

$$\frac{\partial}{\partial z}\,\tilde{\varepsilon} = \tilde{M}\,\tilde{\varepsilon}\,, \qquad \text{a Matrix equation .} \qquad \text{D.3}$$

Assuming the variation of M to be negligible (SVEA) in the interval z and z + Δ z, the fields at position z + Δz may be calculated from that at position z, during the equation

$$\begin{pmatrix}\varepsilon_F\\ \\ \varepsilon_B\end{pmatrix}_{z+\Delta z} = \text{Exp}(M_1)\;\Delta z \begin{pmatrix}C + M_1 S & M_2 S\\ \\ -M_3 S & C - M_1 S\end{pmatrix}\begin{pmatrix}\varepsilon_F\\ \\ \varepsilon_B\end{pmatrix}_z,$$

D.4

where

$$C = \text{Cosh} \left\{ \sqrt{(M_1-M_2)^2/4 - M_1M_2\Delta z} \right\} \qquad \text{D.5}$$

and

$$S = \sqrt{(M_1-M_2)^2/4 - M_1M_2}\ \Delta z\ \text{Sinh} \left\{ \sqrt{(M_1-M_2)^2/4 - M_1M_2\ \Delta z} \right\}$$

D.6

while,

$$\Delta\varphi_{z+\Delta z} = \Delta\varphi_z + \left(\frac{\partial \varphi}{\partial z} \right)_z \Delta z \qquad \text{D.7}$$

Using equations D.4, and D.7 the value of ε at $z + \Delta z$ is calculated from the value at z. Equation 3.37c gives the the value of $\frac{\partial\varphi}{\partial z}$ at $z + \Delta z$ in terms of the values of ε_F, ε_B and $\Delta\varphi$ at z. By this process of iteration the fields are calculated along the length of the cavity, starting with the transmitted fields and eventually evaluating the incident fields.

BIBLIOGRAPHY

1. H. Seidel, U.S. Patent No. 3,610,731 (Oct. 5, 1971).
2. A. Szoke, V. Daneu, J. Goldhar, and N. A. Kurnit, Appl. Phys. Lett. 15, 376 (1969).
3. S. L. McCall, Phys. Rev. A. 9, 1515 (1974).
4. Ref. 2; J. W. Austin and L. G. Deshazer, J. Opt. Soc. Am. 61, 650 (1971); J. W. Austin, "Laser Saturable Resonators, and Criteria for Their Bistable Operation", PhD. Dissertation, University of Southern California, Jan. 1972; E. Spiller, J. Opt. Soc. Am. 61, 699 (1971), and J. Appl. Phys. 43, 1673 (1972).
5. S. L. McCall, H. M. Gibbs, G. G. Churchill, and T. N. C. Venkatesan, Bull. Am. Phys. Soc. 20, 636 (1975); Journ. Opt. Soc. Am. 65, 1184 (1975); H. M. Gibbs, S. L. McCall, T. N. C. Venkatesan, Phys. Rev. Lett. 36 1135 (1976); H. M. Gibbs, S. L. McCall, T. N. C. Venkatesan, U.S. Patent No. 4,012,699.
6. In Ref. 5 the term nonlinear dispersion was used instead of nonlinear refractive index, because of the spectral dependence. The two terms have the same physical meaning.
7. F. S. Felber and J. H. Marburger, Appl. Phys. Lett. 28, 731 (1976).
8. T. N. C. Venkatesan and S. L. McCall, Appl. Phys. Lett. 30, 282 (1977).
9. P. W. Smith and E. H. Turner, Appl. Phys. Lett. 30, 280 (1977).

10. R. Bonifacio and L. A. Lugiato, Opt. Commun. 19, 172 (1976).

11. M. Okuda, M. Toyota and K. Onaka, Opt. Comm. 19, 138 (1976).

12. A simple optical bistable device could also be constructed by properly feeding a part of the output of a FP to drive the PZTs which control the spacing of the FP. Then the device would be limited by the response of the PZTs.

13. S. L. McCall and E. L. Hahn, Phys. Rev. 183, 457 (1969).

14. Self-induced transparency by pulsed coherent light by S. L. McCall, Thesis, Univ. of California, Berkeley, 1967.

15. Optical resonance and two level atoms by L. Allen and J. H. Eberly. J. H. Wiley, 1975.

16. F. Bloch, Phys. Rev. 70, 460 (1946).

17. Handbook of Mathematical Functions, edited by M. Abramowitz and I. A. Stegun (NBS, Washington, D.C., 1964).

18. H. M. Gibbs, G. G. Churchill and G. J. Salamo, Opt. Comm. 12, 396 (1974).

19. J. E. Bjorkholm and A. Ashkin, Phys. Rev. Lett. 32, 129 (1974).

20. G. J. Salamo, "Effects of Degeneracies on Self-Induced Transparency", PhD. Dissertation, The City University of New York, 1974.

21. The dye-laser consisted of a folded cavity [A. Dienes, E. P. Ippen and C. V. Shank, IEEE J. Quantum Electron, 8, 388 (1972)] with jet stream, 4% transmitting output mirror on a piezoelectric translator, two uncoated solid etalons of thicknesses 0.8 and 3 cm, and a 10 mm solid etalon with 20% relfecting coatings.

22. A Szoke and A. Javan, Phys. Rev. 145, 137 (1967).

23. T. W. Hänsch, I. S. Shahin, and A. L. Schawlow, Phys. Rev. Lett. 27, 707 (1971).

24. D. S. McClure, J. Chem. Phys. 36, 2757 (1962); and Solid State Phys. Vol. 9, Edited by F. Seitz and D. Turnbull, Academic Press, New York, 1959.

25. S. Sugano and Y. Tanabe, J. Phys. Soc. Japan. 13, 880 (1958).

26. S. Sugano and I. Tsujikawa, J. Phys. Soc. Japan. 13, 889 (1958).

27 D. F. Nelson and M. D. Sturge, Phys. Rev. 137, A1117 (1975).

28a. D. E. McCumber and M. D. Sturge, Jour. Appl. Phys. 34, 1682 (1963).

28b T. N. C. Venkatesan and S. L. McCall, Rev. of Sci. Instrum. 48, 51(1977). About the time this article was submitted for publication, we heard about reports of a 30% dye laser conversion efficiency at these wavelength using a Kr laser as the pump.

29 M. Birnbaum, P. H. Wendzikowski and C. L. Fincher, Appl. Phys. Lett. 16, 436 (1970).

30. A. Szabo, J. Appl. Phys. 46, 802 (1975).

31. P. F. Liao and S. R. Hartman, Opt. Commun. 8, 310 (1973);
P. F. Liao, P. Hu, R. Leigh, and S. R. Hartman, Phys. Rev. 9, 332 (1974).

32 J. Koo, L. R. Walker and S. Geshwind, Phys. Rev. Lett. 35, 1669 (1975).

33. G. F. Imbusch, W. M. Yen, A. L. Schawlow, G. E. Devlin and J. P. Remeika, Phys. Rev. 136, A481 (1964).

34. H. W. Kogelnik and T. Li, Proc. IEEE, 54 1312 (1966).

35. W. Franzen, Phys. Rev. 115, 850 (1959).

36. R. C. Miller, and W. A. Nordland, Jr., J. Appl. Phys. 46, 2177 (1975).

37. U. J. Schmidt, J. Appl. Phys. 35, 259 (1964).

38. T. Kushida, J. Phys. Soc. Japan 21, 1333 (1966).

39. J. W. Huang and H. W. Moos, Phys. Rev. 173, 440 (1968).

40. W. M. Fairbanks, Jr., G. K. Klauminzer and A. L. Schawlow, Phys. Rev. B 11, 60 (1975).

41. R. W. Keyes and J. A. Armstrong, Appl. Opt., 8, 2549 (1969).

42. S. L. McCall et al, to be published.